UNIVERSIDADE ESTADUAL PAULISTA
"JÚLIO DE MESQUITA FILHO"
Campus de Ilha Solteira

PROGRAMA DE PÓS-GRADUAÇÃO EM ENGENHARIA MECÂNICA

DEVELOPMENT OF A VIRTUAL PIPE TEST RIG FOR TESTING ACOUSTIC CORRELATORS FOR LEAK DETECTION IN BURIED WATER PIPES

DESENVOLVIMENTO DE UM SIMULADOR VIRTUAL DE VAZAMENTOS PARA TESTAR CORRELACIONADORES ACÚSTICOS UTILIZADOS EM DETECÇÃO DE VAZAMENTOS DE ÁGUA EM DUTOS SUBTERRÂNEOS

Mauricio Kiotsune Iwanaga

Orientador: Prof. Dr. Michael John Brennan
Co-orientador: Prof. Dr. Oscar Scussel

Ilha Solteira
2019

UNIVERSIDADE ESTADUAL PAULISTA
"JÚLIO DE MESQUITA FILHO"
Campus de Ilha Solteira

PROGRAMA DE PÓS-GRADUAÇÃO EM ENGENHARIA MECÂNICA

DEVELOPMENT OF A VIRTUAL PIPE TEST RIG FOR TESTING ACOUSTIC CORRELATORS FOR LEAK DETECTION IN BURIED WATER PIPES

DESENVOLVIMENTO DE UM SIMULADOR VIRTUAL DE VAZAMENTOS PARA TESTAR CORRELACIONADORES ACÚSTICOS UTILIZADOS EM DETECÇÃO DE VAZAMENTOS DE ÁGUA EM DUTOS SUBTERRÂNEOS

Mauricio Kiotsune Iwanaga

Orientador: Prof. Dr. Michael John Brennan
Co-orientador: Prof. Dr. Oscar Scussel

Dissertation presented to São Paulo State University as a part of the requirements for obtaining the Master's degree in Mechanical Engineering.
Knowledge area: Solid Mechaics.

Ilha Solteira
2019

FICHA CATALOGRÁFICA
Desenvolvido pelo Serviço Técnico de Biblioteca e Documentação

I96d

Iwanaga, Mauricio Kiotsune.
Development of a virtual pipe test rig for testing acoustic correlators for leak detection in buried water pipes / Mauricio Kiotsune Iwanaga. -- Ilha Solteira: [s.n.], 2019
110 f. : il.

Dissertação (mestrado) - Universidade Estadual Paulista. Faculdade de Engenharia de Ilha Solteira. Área de conhecimento: Mecânica dos Sólidos, 2019

Orientador: Michael John Brennan
Co-orientador: Oscar Scussel
Inclui bibliografia

1. Buried water pipes. 2. Acoustic correlation. 3. Leak noise simulation. 4. Compensator. 5. Electro-dynamic exciters. 6. Time delay estimate.

João Josué Barbosa
Serviço Técnico de Biblioteca e Documentação
Diretor Técnico
CRB 8-5642

UNIVERSIDADE ESTADUAL PAULISTA

Câmpus de Ilha Solteira

CERTIFICADO DE APROVAÇÃO

TÍTULO DA DISSERTAÇÃO: Development of a Virtual Pipe Test Rig for Testing Acoustic Correlators for Leak Detection in Buried Water Pipes

AUTOR: MAURICIO KIOTSUNE IWANAGA
ORIENTADOR: MICHAEL JOHN BRENNAN
COORIENTADOR: OSCAR SCUSSEL

Aprovado como parte das exigências para obtenção do Título de Mestre em ENGENHARIA MECÂNICA, área: Mecânica dos Sólidos pela Comissão Examinadora:

Prof. Dr. MICHAEL JOHN BRENNAN
Departamento de Engenharia Mecânica / Faculdade de Engenharia de Ilha Solteira

Prof. Dr. RICARDO TOKIO HIGUTI
Departamento de Engenharia Elétrica / Faculdade de Engenharia de Ilha Solteira

Prof. Dr. SIDNEY BRUCE SHIKI
Departamento de Engenharia Mecânica / Universidade Federal de São Carlos

Ilha Solteira, 09 de agosto de 2019

To my parents Ricardo and Marinês, my beloved girlfriend Carol and all my friends that supported me.

ACKNOWLEDGEMENTS

I would like to thank Prof. Mike Brennan for all the patience and teaching that he has provided me over the last years. I am very glad about everything that I have learned and all the results that we have achieved together. Many thanks for all the suggestions and time that you have spent with me.

My co-supervisor, Prof. Oscar Scussel, and Prof. Fabrício Almeida also deserve a special acknowledgement for every advice and support that they have given me. Working with them was very productive and funny. I hope we can work together again in the near future.

My parents, Ricardo and Marinês, and my beloved girlfriend, Carol, were the most important people that have motivated me over the years. I am totally sure that I could not achieve such a progress without their motivation, support and care. I love you all.

There is no doubt that my friends and colleagues also have their contribution in this work. I would like to give a special thanks to Fábio Kroll, Vinícius Cleante and Pedro Ayala for the technical support and friendship in this work.

I would like to thank the GMSINT from UNESP – Ilha Solteira for giving the opportunity to carry out this research. I also would like to thank grant #2017/16953-8, São Paulo Research Foundation (FAPESP), and SABESP for the financial support over the years.

Finally, I want to thank the MGT Brazilian Jiu Jitsu, specially my sensei Henrique Urzulin and my senpai Kelson Souza, for giving me important lessons and good times that have helped me indirectly to carry out this work.

“Do not pray for easy lives. Pray to be stronger men.” - John F. Kennedy

RESUMO

Vazamentos em tubulações de água enterradas são considerados um importante problema já que uma grande quantidade de água é desperdiçada entre a planta de tratamento e os consumidores. Para lidar com tal problema, companhias de saneamento utilizam dispostivos para localizar vazamentos nas tubulações. Dispositivos de escuta e correlacionadores de ruídos são os equipamentos mais utilizados em campo pelas companhias de sanemaneto ao redor do mundo. Correlacionadores de ruídos são dispositivos usados na localização de vazamentos em tubulações enterradas através da estimativa do tempo de atraso entre os sinais medidos pelos sensores posicionados em ambos os lados de um suposto vazamento. Uma vez que as companhias de saneamento devem decidir qual tipo de correlacionador é o mais compatível com a sua rede de tubulações, elas devem realizar alguns testes para ajudar em tal decisão e para treinar os funcionários que operam estes dispositivos, os quais devem ser expostos a diferentes condições, tais como tubos de diferentes materiais e geometrias, diferentes tipos de solo, vazamentos com diferentes intensidades, etc. Neste contexto, o principal objetivo desta pesquisa é contribuir com esta necessidade através da elaboração de um dispositivo de bancada capaz de reproduzir as vibrações de um tubo causadas por um vazamento. O dispositivo, chamado de simulador virtual de vazamentos, é composto por um computador, um amplificador de potência com dois canais e dois shakers. Ruídos de vazamento são gerados no computador através de um modelo de tubo enterrado com vazamento, implementado como um software no Matlab®. Tais ruídos são chamados de ruídos de vazamento sintetizados. Uma vez que os sistemas são compostos por amplificadores e shakers cuja dinâmica afeta as vibrações geradas por eles, a compensação de tal dinâmica é realizada. Isso é feito através dos compensadores, que são filtros implementados no computador, que compensam a dinâmica através da filtragem dos sinais de entrada antes de serem fornecidos aos sistemas. Os resultados satisfatórios de tal compensação foram verificados no computador, através da combinação da resposta dos sistemas, e por um teste em laboratório. Tais resultados motivaram outro teste em laboratório, no qual o ruído de vazamento foi filtrado pelos compensadores antes de serem fornecidos aos amplificadores e aos shakers, para simular o ruído de vazamento em tubulações enterradas.

Palavras Chave: Tubulações de água enterradas. Correlação acústica. Simulação de ruído de vazamento. Compensador. Atuadores eletro-mecânicos. Estimativa de tempo de atraso.

ABSTRACT

Leakage in buried water pipes is an important problem since a large amount of water is wasted between the treatment plant and the consumers. To deal with such a problem, water companies have used some devices to localize leaks in the pipe network. Listening devices and leak noise correlators are the most popular equipment used in the field by the water companies around the world. Leak noise correlators are important devices used to localize leaks in buried pipes by calculating the time delay between the signals measured by the sensors positioned either side of a suspected leak. Since water companies have to decide which leak noise correlator is more suitable for each pipe network, they have to carry out some field tests to assist in this decision and to train the personnel that handles such a device, which ideally must be exposed to different conditions, such as pipes with different materials and geometries, different types of soil, different leak strengths, etc. The main objective of this research project is to contribute with the necessity of the water companies by designing an indoor bench-top device capable to reproduce the pipe vibrations generated by a leak in the field. The device, called virtual pipe test rig, comprises a computer and a dual-channel power amplifier supplying two shakers. In the computer, leak noise is synthesized by using a model of a buried leaking pipe implemented using the software Matlab®. Since the systems, composed by the power amplifiers and the shakers, have dynamics that affect the vibrations they generate, compensation of the system dynamics is necessary. This is carried out using compensators, which are filters that are realized in the computer, that compensate for the dynamics by filtering the input signals before supplying them to the amplifiers. The results provided by the compensation were verified in the computer, by combining the response of the systems and the response of the compensators, and by carrying out a laboratory experiment. Further experiments were carried out, in which the synthesized leak noise is filtered by the compensators before supplying the power amplifiers and the shakers, simulating a leak in a buried pipe.

Keywords: Buried water pipes. Acoustic correlation. Leak noise simulation. Compensator. Electro-dynamic exciters. Time delay estimate.

LIST OF FIGURES

LIST OF TABLES

LIST OF ABBREVIATIONS

ACF	Auto-Correlation Function
CCC	Cross-Correlation Coefficient
CCF	Cross-Correlation Function
CPSD	Cross-Power Spectral Density
FFT	Fast Fourier Transform
FRF	Frequency Response Function
IRF	Impulse Response Function
MDPE	Medium Density Polyethylene
NRC	National Research Council
PID	Proportional Integral Derivative
PSD	Power Spectral Density
SABESP	São Paulo State Basic Sanitation Company
SDOF	Single Degree of Freedom

LIST OF SYMBOLS

Symbol	Name	Units
a	Mean pipe radius	m
$a(t)$	Acceleration of the SDOF system	m/s²
$\bar{a}_1(t)$	Acceleration provided by the virtual pipe system 1	m/s²
$\bar{a}_2(t)$	Acceleration provided by the virtual pipe system 2	m/s²
$\hat{a}(t)$	Acceleration of the compensated SDOF system $\hat{a}_1(t)$	m/s²
	Acceleration provided by the compensated virtual pipe system 1	m/s²
$\hat{a}_2(t)$	Acceleration provided by the compensated virtual pipe system 2	m/s²
$A(\omega)$	Fourier transform of $a(t)$	m/s²
$\bar{A}(\omega)$	Acceleration provided by the compensated SDOF system	m/s²
B_{water}	Bulk modulus of the water	N/m²
c	Damping of the SDOF system	N.s/m
$c(\omega)$	Wavespeed	m/s
d	Distance between the sensors	m
d_1	Distance between the leak and the sensor 1	m
d_2	Distance between the leak and the sensor 2	m
E_{pipe}	Young's modulus of pipe-wall material	N/m²
f	Frequency	Hz
$f(t)$	Force applied to the mass of the SDOF system	N
$\hat{f}(t)$	$f(t)$ filtered by $\hat{h}^a(t)$	N
$F(\omega)$	Fourier transform of $f(t)$	N
$\bar{F}(\omega)$	Combination of $F(\omega)$ and $\bar{H}^a(\omega)$	N
$g^a(t, d_1)$	IRF between the leak pressure and the acceleration of the pipe-wall at a distance d_1 from the leak	-
$g^a(t, d_2)$	IRF between the leak pressure and the acceleration of the pipe-wall at a distance d_2 from the leak	-

$g^a(t,x)$	IRF between the leak pressure and the acceleration of the pipe-wall at a distance x from the leak	-
G_{soil}	Shear modulus of the soil	N/m²
$G^a(\omega,x)$	FRF between $P_l(\omega)$ and the acceleration of the pipe-wall at a distance x from the leak	m/(Pa.s²)
$G^d(\omega,x)$	FRF between $P_l(\omega)$ and $W_x(\omega)$	m/Pa
$G^p(\omega,x)$	FRF between $P_l(\omega)$ and $P_x(\omega)$	-
h	Pipe-wall thickness	m
$h(t)$	IRF for displacement of the SDOF system	m/N
$\dot{h}(t)$	IRF for velocity of the SDOF system	m/(N.s)
$\ddot{h}(t)$	IRF for acceleration of the SDOF system	m/(N.s²)
$\ddot{h}_1(t)$	IRF of the virtual pipe system 1	m/(V.s²)
$\ddot{h}_2(t)$	IRF of the virtual pipe system 2	m/(V.s²)
$\bar{h}^a(t)$	IRF of the compensator for a SDOF system	-
$\bar{h}_1^a(t)$	IRF of the compensator for the virtual pipe system 1	-
$\bar{h}_2^a(t)$	IRF of the compensator for the virtual pipe system 2	-
$\hat{h}^a(t)$	Modified IRF of the compensator for a SDOF system	-
$\hat{h}_1^a(t)$	Modified IRF of the compensator for the virtual pipe system 1	-
$\hat{h}_2^a(t)$	Modified IRF of the compensator for the virtual pipe system 2	-
$\ddot{h}_{\text{com}}(t)$	IRF for acceleration of the compensated SDOF system	m/(N.s²)
$\ddot{h}_{\text{com}_1}(t)$	IRF of the compensated virtual pipe system 1	m/(V.s²)
$\ddot{h}_{\text{com}_2}(t)$	IRF of the compensated virtual pipe system 1	m/(V.s²)
$H^a(\omega)$	Accelerance of the SDOF system	m/(N.s²)
$\bar{H}^a(\omega)$	FRF of the compensator for a SDOF system	-
$H_1^a(\omega)$	FRF of the virtual pipe system 1	m/(V.s²)
$H_2^a(\omega)$	FRF of the virtual pipe system 2	m/(V.s²)

$H^a_{\text{com}}(\omega)$	FRF of the compensated SDOF system	m/(N.s²)
$H^a_{\text{com}_1}(\omega)$	FRF of the compensated virtual pipe system 1	m/(V.s²)
$H^a_{\text{com}_2}(\omega)$	FRF of the compensated virtual pipe system 2	m/(V.s²)
k	Stiffness of the SDOF system	N/m
$k(\omega)$	Wavenumber	rad/m
$k_{\text{water}}(\omega)$	Wavenumber of the water	rad/m
K_{water}	Dynamic stiffness of the water	N/m³
K_{pipe}	Dynamic stiffness of the pipe	N/m³
$K^{(\text{stiff})}_{\text{pipe}}$	Stiffness component of the pipe wall	N/m³
$K^{(\text{inertia})}_{\text{pipe}}$	Inertia component of the pipe wall	N/m³
K_{soil}	Dynamic stiffness of the soil	N/m³
m	Mass of the SDOF system	kg
$P_l(\omega)$	Leak pressure	Pa
$P_x(\omega)$	Pressure measured at a distance x from the leak	Pa
$R_{y_1y_2}(\tau)$	CCF between $y_1(t)$ and $y_2(t)$	-
$\hat{R}_{y_1y_2}(\tau)$	Biased CCF between $y_1(t)$ and $y_2(t)$	-
$R_{\bar{y}_1\bar{y}_2}(\tau)$	CCF between $\bar{y}_1(t)$ and $\bar{y}_2(t)$	-
$R_{zz}(\tau)$	ACF of $z(t)$	-
$S_{\bar{a}_1\bar{a}_2}(\omega)$	CPSD between $\bar{a}_1(t)$ and $\bar{a}_2(t)$	m²/(Hz.s^4)
$S_{\hat{a}_1\hat{a}_2}(\omega)$	CPSD between $\hat{a}_1(t)$ and $\hat{a}_2(t)$	m²/(Hz.s^4)
$S_{\text{data}_1}(\omega)$	CPSD of the accelerations measured at the SABESP test site	m²/(Hz.s^4)
$S_{\text{data}_2}(\omega)$	CPSD of the accelerations measured at the NRC test site	m²/(Hz.s^4)
$S_{y_1y_2}(\omega)$	CPSD between $y_1(t)$ and $y_2(t)$	Hz^{-1}
$\hat{S}_{y_1y_2}(\omega)$	Biased CPSD between $y_1(t)$ and $y_2(t)$	Hz^{-1}
$S_{\bar{y}_1\bar{y}_2}(\omega)$	CPSD between $\bar{y}_1(t)$ and $\bar{y}_2(t)$	Hz^{-1}

t	Time	s
T	Time length	s
$W_x(\omega)$	Radial wall displacement at a distance x from the leak	m
x	Distance measured from the leak	m
$y_1(t)$	Leak noise measured by the sensor 1	-
$y_2(t)$	Leak noise measured by the sensor 2	-
$\bar{y}_1(t)$	Synthesized leak noise of the convolution of $z(t)$ with $g^a(t,d_1)$	-
$\bar{y}_2(t)$	Synthesized leak noise of the convolution of $z(t)$ with $g^a(t,d_2)$	-
$\bar{Y}_1(\omega)$	Fourier transform of $\bar{y}_1(t)$	-
$\bar{Y}_2(\omega)$	Fourier transform of $\bar{y}_2(t)$	-
$z(t)$	White noise	-
$z_1(t)$	White noise used as an input signal to the virtual pipe system 1	-
$z_2(t)$	White noise used as an input signal to the virtual pipe system 2	-
α	Time delay of the compensator	s
$\gamma_{\bar{a}_1\bar{a}_2}(\omega)$	Coherence between $\bar{a}_1(t)$ and $\bar{a}_2(t)$	-
$\gamma_{\hat{a}_1\hat{a}_2}(\omega)$	Coherence between $\hat{a}_1(t)$ and $\hat{a}_2(t)$	-
$\gamma_{\text{data}_1}(\omega)$	Coherence of the accelerations measured at the SABESP test site	-
$\gamma_{\text{data}_2}(\omega)$	Coherence of the accelerations measured at the NRC test site	-
$\gamma_{\bar{y}_1\bar{y}_2}(\omega)$	Coherence function between $\bar{y}_1(t)$ and $\bar{y}_2(t)$	-
ζ	Damping ratio of the SDOF system	-
ν_{pipe}	Poisson's ratio of the pipe material	-
ρ_{pipe}	Density of the pipe material	kg/m³
ρ_{water}	Density of the water	kg/m³
$\rho_{\bar{a}_1\bar{a}_2}(\tau)$	CCC between $\bar{a}_1(t)$ and $\bar{a}_2(t)$	-
$\rho_{\hat{a}_1\hat{a}_2}(\tau)$	CCC between $\hat{a}_1(t)$ and $\hat{a}_2(t)$	-
$\rho_{\text{data}_1}(\tau)$	CCC of the accelerations measured at the SABESP test site	-
$\rho_{\text{data}_2}(\tau)$	CCC of the accelerations measured at the NRC test site	-

$\rho_{y_1 y_2}(\tau)$	CCC between $y_1(t)$ and $y_2(t)$	-
$\rho_{\bar{y}_1 \bar{y}_2}(\tau)$	CCC between $\bar{y}_1(t)$ and $\bar{y}_2(t)$	-
τ	Lag time	s
τ_{peak}	Difference in propagation times between the leak and the sensors	s
$\Phi(\omega)$	Phase of the CPSD between $y_1(t)$ and $y_2(t)$	rad
$\Phi_{\bar{y}_1 \bar{y}_2}(\omega)$	Phase of the CPSD between $\bar{y}_1(t)$ and $\bar{y}_2(t)$	rad
ω	Angular frequency	rad/s
ω_d	Damped natural frequency of the SDOF system	rad/s
ω_n	Natural frequency of the SDOF system	rad/s

CONTENTS

1 INTRODUCTION

1.1 BACKGROUND

A large amount of water is lost in many water distribution systems between the treatment plant and the consumers. According to the world bank, approximately 90 billion liters of water are lost due to leakage globally each day. Such a loss represents 30-50% of the world's pumped water (KINGDOM *et al.*, 2016). In developing countries, the loss of water can reach alarming levels (GRANT *et al.*, 2012). In Brazil, for example, 38% of the total potable is lost before reaching residences and industries, with some states, such as Roraima (RR) and Amapá (AP), losing about 70% of its potable water (O GLOBO, 2018; O GLOBO, 2019) as shown in Fig. 1.

Furthermore, a recent study highlighted São Paulo as a city at great risk of running out of water in the future (BBC, 2018). In 2015, this city went through a severe water crisis when the main reservoir fell below 4% of its capacity. At the height of the crisis, São Paulo, which is one of the most populated cities in the world and has over than 21 million inhabitants, had less than 20 days of water supply. The São Paulo State Basic Sanitation Company (SABESP), estimated that around 3.5 billion liters of water per day pass through the distribution pipelines in the city and the water loss index reaches about 30%. Of the amount lost, 19.5% corresponds to leakage, and 10.5% to fraud and robbery of water directly from the pipe system (SABESP, 201?).

Considering the importance of water for the global population and the amount that is wasted, it is vital to minimize leakage from water distribution pipes, and a main aspect of this challenge is to detect and to locate leaks. An effective leak detection technique yields many benefits. First and foremost, by finding and fixing leaks, there is an immediate saving in pumping and water treatment costs. Second, if leaks are early discovered, repairs can be scheduled to avoid major damage to the pipe network, such as major pipe breaks, and erosion of foundations of roads and buildings. In addition, public health is protected since leaks are potential entries for contaminants if a pressure drop occurs in the system. To deal with such a problem, researches and water companies around the world have developed water audit procedures and leak detection methods over the last years. As a result, several leak detection techniques are well-established and efficient equipment are often used to detect leaks in pipe networks.

Figure 1 – Map of percentage of wasted water in each state before reaching residences and industries in Brazil.

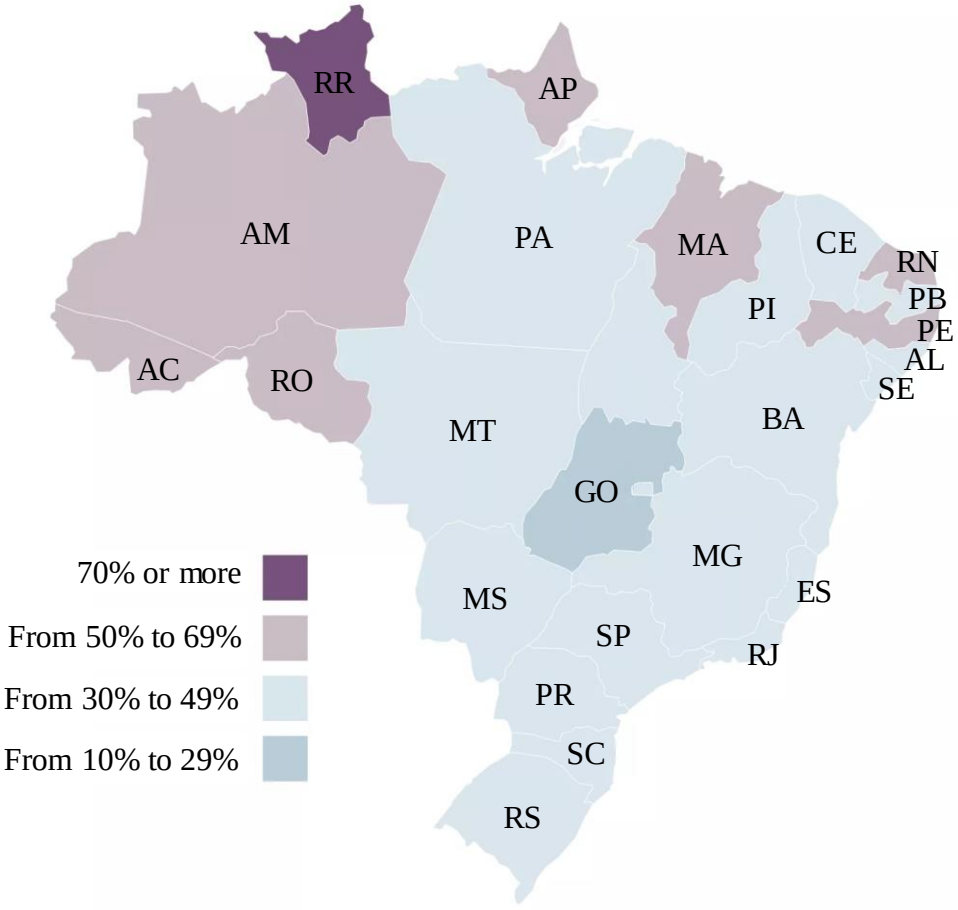

Source: adapted from O Globo (2019).

1.2 LEAK DETECTION TECHNIQUES, SURVEYS AND EQUIPMENT

The following subsections present the leak detection techniques, surveys and equipment that are commonly used by water companies. The first subsection introduces the leak detection techniques which are classified as acoustic or non-acoustic methods. The second subsection describes the usual methodology performed by water companies to detect and localize leaks in the pipework. The third subsection presents the most used leak detection equipment, such as listening sticks, geophones and leak noise correlators. Some advantages and shortcomings of using these devices are also presented in this subsection.

1.2.1 Leak detection techniques

Pressure measurements together with flow measurements are often used to determine if a leak is present in a specific part of the pipework (PUUST *et al.*, 2010). If a leak is confirmed, an acoustic technique is usually applied to localize such a leak in the pipework. Acoustic techniques are algorithms used to localize acoustic sources based on the sound that propagates within a media (RITU; DHULL, 2015; LI *et al.*, 2016). Since leaks from water supply pipes generate sound, an acoustic technique can be used for leak detection and localization. Acoustic techniques have been shown to be effective in detecting and localizing leaks in buried pipes (FUCHS; RIEHLE, 1991; LISTON; LISTON, 1992; FANTOZZI et al., 1993).

There are some other methods based on non-acoustic technologies such as ground-penetrating radar (HUNAIDI; GIAMOU, 1998; SNEDDON, 2000), thermography (WEIL, 1993), and tracer gas that were evaluated by Hunaidi et al. (2000b). Each technique has both advantages and shortcomings. Although they are considered promising alternatives in leak detection, non-acoustic techniques are more complex and time-consuming, and may fail to detect leaks in practical situations.

1.2.2 Leak detection surveys

Leak detection using acoustic equipment is generally performed in two stages. In the first stage, the entire system is surveyed for leak sounds. Such a survey is usually conducted by listening devices, such as listening sticks, on all accessible contact points with the pipework system such as fire hydrants, valves, stopcocks, etc. The contact of the listening devices with the accessible parts of the pipework system is more favorable than the contact of them with the ground surface, since the attenuation of the leak noise is lower along the pipe, relative to the distance travelled, than through the ground surface.

When a sound is heard, the location is noted as a potential leak site. After mapping all the potential leak sites, the second stage is performed in which each suspect location is further investigated. More accurate measurements can be taken to pinpoint the exact locations of the leaks by using more sophisticated equipment such as geophones, which is an instrument used to listen for the leak sounds on the ground directly above the pipe at close intervals, or leak noise correlators, which is an instrument that can estimate the location of a leak by measuring the time delay between the leak signals.

1.2.3 Leak detection equipment

Listening devices, including listening sticks and geophones, may be either mechanical or electronic. They contain sensitive mechanism or materials, for example piezo-electric elements, that facilitate the listening of leak noise. Some modern electronic devices may include signal amplifiers and noise filters, which could be very helpful in adverse environments. The use of such listening devices, shown in Fig. 2(a)-(b), is usually straightforward but their effectiveness depends upon the experience of the user.

Figure 2 – Examples of the use of acoustic instruments to detect leaks on the field.

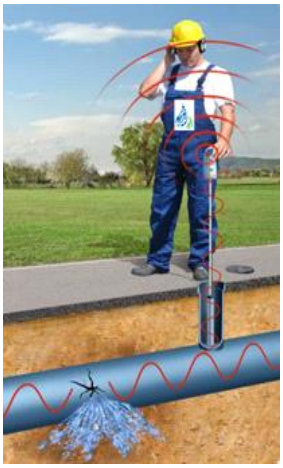

(a) Listening stick

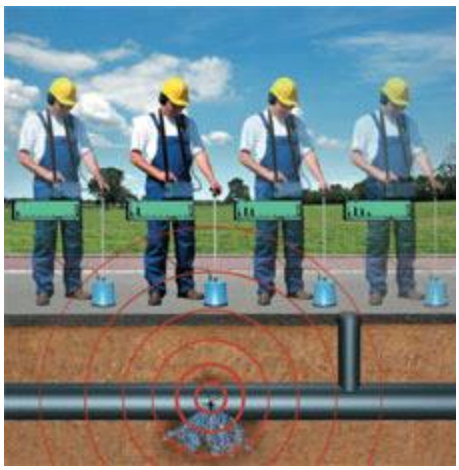

(b) Geophone

(c) Leak noise correlator

Source: adapted from Aquasave (2015).

Leak noise correlators, such as the ones shown in Fig. 2(c), are more efficient and more accurate than listening devices. They are state-of-art portable computer-based devices that can pinpoint the exact location of a leak automatically. The advantages of leak noise correlators over traditional listening devices means that they have become popular in recent years, and water companies from Brazil and many other countries worldwide have adopted them as the main alternative to detect leaks in pipework. The use of listening devices seeks to locate a leak by identifying the position of maximum leak noise intensity, which is determined by repeated listening on the ground along the pipeline route. Listening must be carried out at night to avoid high levels of environmental noise and even so, leak localization on deeper buried pipelines may be difficult or impossible due to the faster attenuation of sound by the ground. Furthermore, the positions located on the ground surface where the noise is a maximum might also not coincide with the actual leak position, since the noise might have followed an indirect path through the pipeline backfill. False leak localization might also be related to the percussion of the leak jet into the adjacent ground surrounding the pipeline.

Although leak noise correlators also use the sound generated by a leak, the method applied to estimate its position is different from the method when a listening device is used. Instead of using the sound intensity, leak noise correlators estimate the position of a leak based on sound similarity involving the properties of leak noise propagation. They can locate leaks in either automatic or manual mode based on the cross-correlation method. Since the introduction of this device in the early 1980s, the correlation technique, which is the most used acoustic technique for leak detection, has been significantly improved.

A leak noise correlator is usually composed by two acoustic/vibrations sensors, wireless signals transmitters and receivers, and an electronic processing unit. This device has great flexibility due to the advances in the types of sensors available currently. Leak noise is measured by the two sensors and the signals are transmitted to the electronic process unit, where they are digitized and cross-correlated. The cross-correlation function produces an output that indicates how similar the two signals are as they are shifted in time with respect to one another. If there is a leak at the mid-point between the two sensors, the cross-correlation function is given by a single central peak value since the leak noise wave reaches both sensors at the same time. More usually, the leak is located asymmetrically between the two sensors. In this case, the leak noise wave reaches one sensor before the other, and consequently there is a time delay between the measured signals. Then, the peak of the cross-correlation function is offset from the center by this time difference.

1.3 LEAK DETECTION USING THE CORRELATION TECHNIQUE

A schematic diagram showing a typical arrangement for leak detection using a leak noise correlator is shown in Fig. 3. Such a device estimates the leak position in buried water pipes by using the correlation technique, where a sensor is positioned either side of a suspected leak at distances d_1 and d_2. The distance d between the sensors, is equal to $d_1 + d_2$ and is assumed to be known. Accelerometers or hydrophones, which measure vibration or acoustic signals, are often used. Vibration signals are transmitted from the sensors to the leak noise correlator which calculates the cross-correlation function of the two signals, and hence the time delay, and presents the estimated results to an operator (GAO *et al.*, 2004).

Figure 3 – Schematic diagram of a buried pipe with a leak bracketed by two sensors.

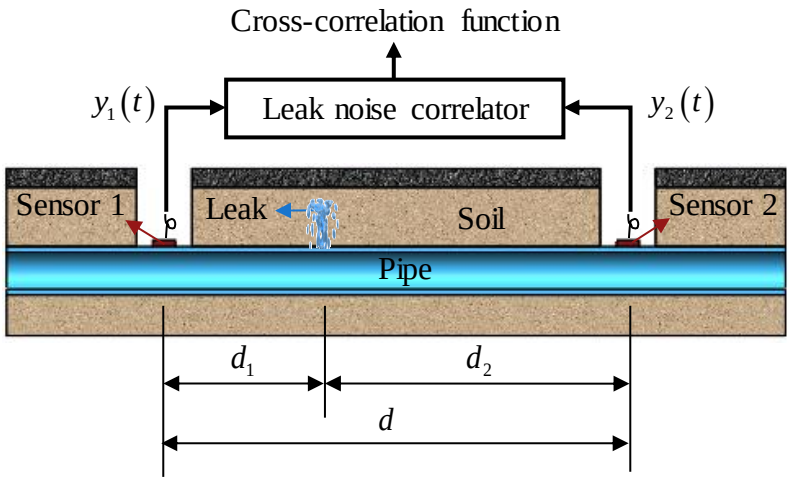

Source: elaborated by the author.

In order to localize the leak in a buried water pipe, it is necessary to estimate either d_1 or d_2. So, considering the arrangement given by Fig. 3, the distance d_1 can be calculated by (GAO *et al.*, 2004)

$$d_1 = \frac{d - c\tau_{\text{peak}}}{2} \tag{1}$$

where c and $\tau_{\text{peak}} = (d_2 - d_1)/c$ are the wavespeed (speed of leak noise propagation) and time delay between the arrival times of the leak noise at sensor positions 1 and 2. In Fig. 3, $y_1(t)$ and $y_2(t)$ are the leak noise signals from sensors 1 and 2 respectively.

The cross-correlation function between $y_1(t)$ and $y_2(t)$ is used to estimate the time delay, which is given by a distinct peak in such a function (GAO *et al.*, 2004). Note that c is assumed to be constant in Eq. (1), and is usually estimated from tables or measured in situ. However, since the wavespeed is not constant between the sensors 1 and 2 in practical situations, the estimation of the leak position is uncertain (LIMA *et al.*, 2019).

The peak in the correlation function is used to estimate the time delay τ_{peak} between $y_1(t)$ and $y_2(t)$. So, knowing the time delay τ_{peak} and the wavespeed c, the location of the leak can be calculated through Eq. (1) (BRENNAN *et al.*, 2016).

1.4 LEAK NOISE SIMULATION

The following subsections present the leak noise simulation using test sites and using laboratory devices. The first subsection describes how leak noise simulation is performed in test sites, and the second subsection describes how it is performed by using laboratory devices.

1.4.1 Leak noise simulation using test sites

Since the correlation technique is considered to be a straightforward and accurate method, it is widely used by water companies to detect leaks in their pipework systems. However, these companies have to decide which leak noise correlator is more suitable for each pipework system. It is thus necessary to carry out some field tests in order to assist this decision. In addition, these devices require training of the personnel in their use and, ideally, they must be exposed to different conditions that involves different pipe geometries, pipe materials, types of soil and leak strengths. Such a training is applied to provide knowledge and experience to the personnel that will use these devices to detect and localize leaks on the pipework (BRENNAN *et al.*, 2016).

Water companies worldwide usually have test sites to provide such training to the personnel and to test new devices before using to localize leaks on the field. These test sites are basically buried pipework systems in which water is pumped through them, and some valves or stopcocks are attached to the pipework to simulate leaks. Some access points to the pipes are available and are used to attach the sensors to measure leak noise. Water companies usually build each section of these test sites including pipes with different materials and dimensions, and different types of soil, to provide a wide range of conditions.

In Brazil for example, SABESP, which is a basic sanitation company in the state of São Paulo (SP), has a test site to perform the training of the personnel and the test of the leak detection equipment. Some studies have been carried out in this test site, which resulted in important contributions to leak detection in buried water pipes and the effects of soil properties in leak noise propagation (BRENNAN *et al.*, 2017; BRENNAN *et al.*, 2018; SCUSSEL *et al.*, 2018; SCUSSEL *et al.*, 2019). Some other studies have been carried out in test sites from other countries, such as Canada and United Kingdom, which were used to test different methods to detect leaks in buried water pipes (HUNAIDI; CHU, 1999; HUNAIDI *et al.*, 2000a; MUGGLETON; BRENNAN, 2008; MUGGLETON *et al.*, 2011), to validate models related to the leak noise propagation (MUGGLETON *et al.*, 2004b; GAO *et al.*, 2004; GAO *et al.*, 2005; MUGGLETON; YAN, 2013; ALMEIDA, *et al.*, 2014a; ALMEIDA, *et al.*, 2014b; ALMEIDA, *et al.*, 2015; BRENNAN *et al.*, 2016, GAO *et al.*, 2016; GAO *et al.*, 2017; ALMEIDA, *et al.*, 2018) and to validate methods to determine the time delay of the leak noise based on the correlation technique (GAO *et al.*, 2006; BRENNAN *et al.*, 2007).

1.4.2 Leak noise simulation using laboratory devices

Test sites are extremely useful for water companies, since they can use them to test their leak detection equipment and to train their personnel to detect leaks on the field, and for research, since they can simulate leaks under controlled conditions to validate experimentally studies regarding models of leak noise propagation, methods to detect leaks in buried water pipes, methods to determine the time delay of the measured leak noise, etc. Although test sites are very important, they can also be very expensive and time-consuming since their construction requires a large space and a lot of equipment, such as pipes of different materials and dimensions, pumps, valves, stopcocks, etc.

Figure 4 – Schematic diagram of the virtual pipe test rig proof-of-concept developed by Brennan *et al.* (2016).

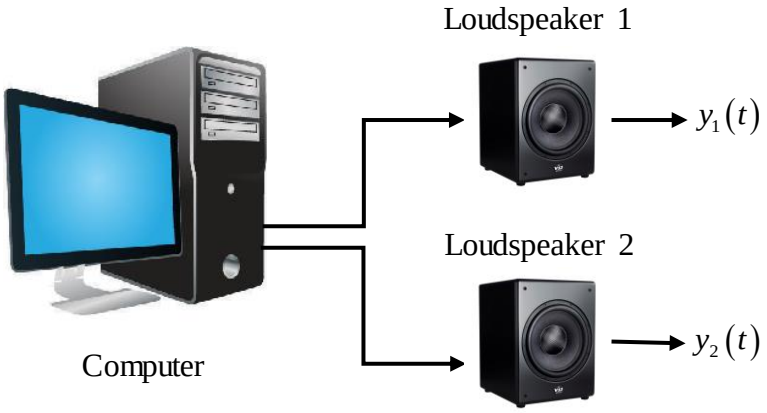

Source: elaborated by the author.

An alternative way of carrying out such a leak noise simulation is by using laboratory devices. This new way of simulating a leak in a buried water pipe can be very advantageous, since it provides a broad range of different conditions that can be simulated in a laboratory, and its setup is relatively fast and low-cost when it is compared with the setup of a test site. Some investigations about axisymmetric wave propagation in fluid filled pipes have been conducted by Pininngton and Briscoe (1994), using an experimental setup given by a water-filled pipe, an electromagnetic shaker and some sensors. The same experimental setup was also used by Muggleton *et al.* (2004a) to validate a model of wavenumber prediction for water-filled pipe in vacuo.

In recent years, a laboratory device was developed by Brennan *et al.* (2016) to carry out a proof-of-concept study of a new device, called virtual pipe test rig, which is able to generate vibrations representative of the pipe vibrations due to a leak. The vibrations generated by the virtual pipe test rig can be used to perform an indoor leak noise simulation to test leak noise correlators, which are commonly used by water companies, without the need of a test site. The device developed by Brennan *et al.* (2016) is composed by a computer and two small modified loudspeakers, with integral power amplifiers, as shown in Fig. 4. The device simulates a buried leaking pipe by generating the leak noise $y_1(t)$ and $y_2(t)$ shown in Fig. 3. The loudspeakers produce the leak sounds, given by a model of leak propagation implemented as software within the computer, whose vibrations are measured with small accelerometers attached to the loudspeakers.

Figure 5 – Schematic diagram of the virtual pipe test rig with more robust actuators.

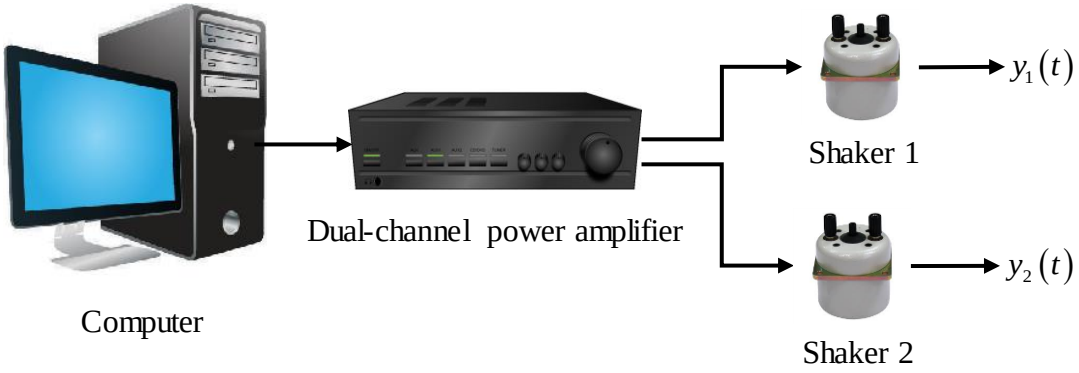

Source: elaborated by the author.

Although the small modified loudspeakers were considered to be an adequate vibration exciter for a proof-of-concept study, more robust actuators would be necessary in a practical system (BRENNAN *et al.*, 2016), since the sensors of the leak noise correlators may vary in size or in mass. One alternative way to perform an indoor leak noise simulation, with more robust actuators, is by using the laboratory device illustrated in Fig. 5. Instead of using two loudspeakers with integral power amplifiers, two electro-dynamic shakers are cascaded with a dual-channel power amplifier to generate the vibrations representative of the pipe vibrations due to a leak.

1.5 REVIEW ABOUT COMPENSATION FOR THE DYNAMICS OF ACTUATORS

The proof-of-concept study performed by Brennan *et al.* (2016) showed that the actuators, together with the power amplifiers, have dynamics that must be carefully considered if the system composed by such devices is used to faithfully model situations that are found on the field. This study showed that, when the leak noise is provided as voltage signal to the actuators through the computer, they generate sounds/vibrations which contain the effects of such dynamics. The correlation of the sounds/vibrations provided by the actuators does not agree with the correlation of the leak noise provided by the computer, since the effects of such dynamics are present in the sounds/vibrations provided by them. To carry out an indoor leak noise simulation that faithfully models the conditions found on the field, Brennan *et al.* (2016) concluded that it is necessary to compensate for the dynamics of these devices.

Field vibration replication in laboratories provides many features, such as over-sampling, long time histories, and filtering (low pass, high pass and band pass), that can be very important to maintain the accuracy of such a laboratory testing (BAREN; MACMILLAN, 2004). Many studies about compensation for the dynamics and other effects of the response of actuators have been developed, to ensure that the same conditions found on the field are properly replicated in the laboratory. There are a lot of approaches in the literature that were developed to compensate for the delay and dynamic response of electro-hydraulic actuators, which are important devices commonly used to simulate seismic response or to perform durability tests on structures (AHMADIZADEH *et al.*, 2007; CHEN; RICLES, 2009; SHEN *et al.*, 2010; CORNELIS *et al.*, 2014; SHEN *et al.*, 2016; SHEN *et al.*, 2018; YAO *et al.*, 2019). Chen and Ricles (2009) developed a general approach, in which a compensation method for actuator dynamics is used to design a transfer function to modify the signals before supplying them to the actuator. The general approach was analyzed for three popular compensation methods given by:

- **Linear acceleration extrapolation:** an actuator delay compensation method proposed by Horiuchi and Konno (2001). This method is based on a linear acceleration assumption, in which a transfer function is used to modify the signals before supplying them to the actuator to perform the replication. Such a modification is based on predicted values for the signals, which are calculated using linear extrapolation in the time domain.

- **Derivative feedforward compensation:** an actuator delay compensation method that uses a classical PID controller (JUNG; SHING, 2006; MERCAN, 2007). The implementation and control gain settings of the PID controller are selected to design a transfer function, which is used to modify the signals before supplying them to the actuator to perform the replication.

- **Inverse compensation method:** an actuator delay compensation method in which a transfer function is designed based on the model of the actuator response (CHEN *et al.*, 2007; CHEN *et al.*, 2009). The inverse of this transfer function is used to modify the signals before supplying them to the actuator to perform the replication.

Chen and Ricles (2009) validated the general approach using the three methods by carrying out real-time simulations with an experimental setup, composed by an electro-hydraulic actuator and a single-degree-of-freedom structure with an elastomeric damper. Although the compensation methods have different characteristics of amplitude and phase in their frequency response and different ways of implementation, the results showed that the general approach has a satisfactory experimental performance for each compensation method. The approach proposed by Chen and Ricles (2009) is considered a useful way to compensate for the dynamics of actuators used in field vibration replication, and it can also be extended to other compensation methods. A similar approach with a modified version of the inverse compensation method is used in this dissertation to compensate for the dynamics of power amplifiers and electro-dynamic shakers of the virtual pipe test rig.

1.6 OBJECTIVES

The main aim of this dissertation is to investigate the design of a virtual pipe test rig, with more robust actuators as shown in Fig. 5, to test leak noise correlators in the laboratory. For this purpose, the objectives are:

1. To design filters, which are referred as compensators in this dissertation, to compensate for the dynamics of the power amplifiers and shakers of the virtual pipe test rig, using a compensation method.

2. To investigate the performance of the compensators within the computer, by combining the response of the compensators and the response of the systems, and through a laboratory experiment, by filtering the signals with the compensators before supplying them to the power amplifiers and shakers.

3. To investigate if the robust virtual pipe test rig, together with the compensators implemented in the computer, is able to faithfully simulate a buried leaking pipe in the laboratory.

1.7 CONTRIBUTIONS TO KNOWLEDGE

- A method to test leak noise correlators by simulating a buried leaking pipe in the laboratory using a robust low-cost bench-top device has been developed. Such a device is composed by a computer, a dual-channel power amplifier and two electro-dynamic shakers, that generates vibrations representative of the pipe vibrations due to a leak.

- A simplified filter design approach to compensate for the dynamics of actuators has been developed. Such an approach is used to design filters, called compensators, which are convolved with the signals within the computer, before supplying them to the actuators.

1.8 OUTLINE OF THE DISSERTATION

This dissertation consists of 5 chapters and 2 appendixes. Chapter 1 introduces the topic of leak detection by providing a background about its worldwide importance. The equipment and techniques used to localize leaks in buried water pipework are discussed. Some important details about leak detection using acoustic correlation are introduced. The literature review about leak noise simulation and the compensation for the dynamics of actuators is also presented, since electro-dynamic shakers are used to generate vibrations to simulate a buried leaking pipe. The main objectives of the dissertation and the contributions to knowledge are also specified in this chapter.

In Chapter 2, the Cross-Correlation Function (CCF) and the Cross-Power Spectral Density (CPSD) are introduced as a way to estimate the time delay of the leak noise vibration measured by sensors attached to the pipe. The model of a buried leaking pipe is also presented in Chapter 2, by introducing the Frequency Response Function (FRF) and the Impulse Response Function (IRF) between the acceleration of the pipe-wall and the leak pressure. The IRF is used to generate leak noise within the computer, which is referred to as synthesized leak noise, by convolving this function with a white noise signal. An example of such a model is used to generate synthesized leak noise, whose CCF and CPSD are compared with the CCF and the CPSD given by the combination of the acoustic correlation with the buried leaking pipe model.

Chapter 3 introduces a simple approach to design compensators, which are used to compensate for the dynamics of actuators (IWANAGA *et al.*, 2019). The approach is illustrated by designing a compensator for a Single-Degree-of-Freedom (SDOF) system, whose performance was checked in both domains by convolving the response of the compensator and the response of the system within the computer. The same approach was used to design compensators for the systems given by the power amplifiers and the shakers of the virtual pipe test rig cascaded in series. Such systems are called virtual pipe systems, and the performance of their compensators was checked in both domains by convolving the response of the compensators, and the response of the virtual pipe systems within the computer. Given the encouraging results, the performance of the compensators was also checked in both domains by carrying out a laboratory experiment, in which white noise signal was filtered by the compensators before being supplied to the power amplifiers and the shakers of the virtual pipe test rig.

In Chapter 4, leak noise simulation is performed using the virtual pipe test rig together with the compensators implemented in the computer. Two laboratory experiments were carried out to evaluate the robustness of the leak noise simulation. In the first experiment, synthesized leak noise was supplied to the virtual pipe test rig, and the vibrations provided by the shakers were measured using accelerometers. In the second experiment, measured data of a real leak from two different test sites was supplied to the virtual pipe test rig, and the vibrations provided by the shakers were also measured using accelerometers. In both experiments, the performance of the compensators was checked by providing the signals directly to the virtual pipe systems and by filtering the signals with the compensators before supplying them to the virtual pipe systems.

Chapter 5 presents the summary and conclusions of the dissertation. Some recommendations for further work are also given.

In Appendix A, an analytical model for wavenumber prediction is presented to complement Chapter 2, since the FRF of a buried pipe and the wavespeed are functions of the wavenumber. Appendix B presents the IRFs for displacement, velocity and acceleration of a SDOF system. This appendix is used to complement Chapter 3 of the dissertation.

2 LEAK DETECTION USING ACOUSTIC CORRELATION

2.1 INTRODUCTION

This chapter describes the methodology applied to leak detection using acoustic correlation. In most cases, accelerometers (or less commonly, hydrophones) are attached at convenient access points either side of a suspected leak in order to sense the noise generated by the leak. Then, the peak in the correlation function between the measured leak noise is used to determine the difference in propagation times between the leak and the sensors. By combining this difference in propagation times with knowledge of the wavespeed (speed of leak noise propagation) and the distance of both sensors, the location of the suspected leak can be determined (BRENNAN *et al.*, 2016). A model of a buried leaking plastic pipe is presented, considering the soil properties and pipe characteristics adopted in previous works. This is used to obtain the frequency response and impulse response functions between the leak and the measurement positions. To synthesize the leak noise, white noise signal is convolved with the impulse response functions of the system. The synthesized leak noise is used in the estimation of the difference in propagation times between the leak and each sensor by calculating the Cross-Correlation (CCF) and Cross-Power Spectral Density (CPSD) functions.

2.2 OVERVIEW OF LEAK DETECTION USING ACOUSTIC CORRELATION

The difference in propagation times between the leak and the sensors, τ_{peak}, can be determined from the peak in the cross-correlation function between $y_1(t)$ and $y_2(t)$. These signals are measured by the sensors 1 and 2 as shown in Fig. 3. If $y_1(t)$ and $y_2(t)$ are assumed to be continuous and stationary (ergodic) with the mean value set to zero, the cross-correlation function of the leak noise $R_{y_1y_2}(\tau)$ is given by (OPPENHEIM; SCHAFER, 2011)

$$R_{y_1y_2}(\tau) = E\left[y_1(t)\, y_2(t+\tau)\right], \tag{2}$$

where τ is the lag time and $E[\ ]$ is the expectation operator.

The argument τ that maximizes $R_{y_1y_2}(\tau)$ provides an estimate of τ_{peak}. In practice, however, $R_{y_1y_2}(\tau)$ can only be estimated as signals if they are measured during a finite time interval. Therefore, if $y_1(t)$ and $y_2(t)$ are measured in a common time interval $0 \le t \le T$, the biased estimator $\hat{R}_{y_1y_2}(\tau)$ is given by (OPPENHEIM; SCHAFER, 2011)

$$\hat{R}_{y_1y_2}(\tau) = \begin{cases} \dfrac{1}{T}\displaystyle\int_0^{T-\tau} y_1(t)\, y_2(t+\tau)\, dt, & \tau < 0, \\ \dfrac{1}{T}\displaystyle\int_{-\tau}^{T} y_1(t)\, y_2(t+\tau)\, dt, & \tau < 0. \end{cases} \tag{3}$$

Furthermore, it is usual to express the cross-correlation function in a normalized form, which has a scale of -1 to +1, namely the Cross-Correlation Coefficient (CCC) $\rho_{y_1y_2}(\tau)$ defined as

$$\rho_{y_1y_2}(\tau) = \frac{R_{y_1y_2}(\tau)}{\sqrt{R_{y_1y_1}(0)\, R_{y_2y_2}(0)}} \tag{4}$$

where $R_{y_1y_1}(0)$ and $R_{y_2y_2}(0)$ are values of the Auto-Correlation Functions (ACF) $R_{y_1y_1}(\tau)$ and $R_{y_2y_2}(\tau)$ at $\tau = 0$.

The time delay τ_{peak} can also be determined approximately by calculating the phase of the CPSD $S_{y_1y_2}(\omega)$ of the leak noise, where ω is the angular frequency, given by $\omega = 2\pi f$, and f is the frequency that gives the number of cycles in a period of time. The CCF $R_{y_1y_2}(\tau)$ can be determined from the inverse Fourier transform of $S_{y_1y_2}(\omega)$, so that,

$$R_{y_1y_2}(\tau) = \frac{1}{2\pi}\int_{-\infty}^{\infty} S_{y_1y_2}(\omega)\, e^{j\omega\tau}\, d\omega, \tag{5}$$

where $j=\sqrt{-1}$, and $S_{y_1y_2}(\omega)=\left|S_{y_1y_2}(\omega)\right|e^{j\Phi(\omega)}$ in which $\left|S_{y_1y_2}(\omega)\right|$ is the modulus and $\Phi(\omega)$ is the phase. If there is a time delay τ_{peak} between the two signals then the modulus is a constant and $\Phi(\omega)=-\omega\tau_{\text{peak}}$ (BRENNAN *et al.*, 2016).

If $y_1(t)$ and $y_2(t)$ are infinite bandwidth white noise with a pure time delay τ_{peak}, the magnitude and phase of $S_{y_1y_2}(\omega)$ over the infinite bandwidth are given by the constant K and the straight line with slope $-\omega\tau_{\text{peak}}$ respectively. The CCF $R_{y_1y_2}(\tau)$ is given by $K\delta(\tau-\tau_{\text{peak}})$ in which $\delta(\ )$ is the Dirac delta function (SHIN; HAMMOND, 2008).

Since $y_1(t)$ and $y_2(t)$ are finite bandwidth signals in practice, the magnitude and phase of the biased operator $\hat{S}_{y_1y_2}(\omega)$ are given by the constant K and the straight line with slope $-\omega\tau_{\text{peak}}$ over the finite bandwidth of both signals. The biased CPSD $\hat{S}_{y_1y_2}(\omega)$ is shown in Fig. 6 in terms of magnitude and unwrapped phase, considering the signals within the bandwidth 0 to ω_a (SHIN; HAMMOND, 2008).

Figure 6 – Biased CPSD $\hat{S}_{y_1y_2}(\omega)$ with $y_1(t)$ and $y_2(t)$ with frequency content up to ω_a in the frequency domain.

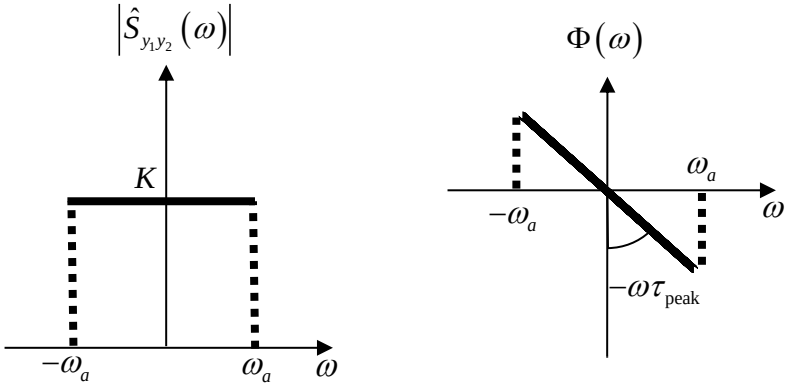

(a) Magnitude (b) Unwrapped phase

Source: elaborated by the author.

Calculating the inverse Fourier transform of $\hat{S}_{y_1y_2}(\omega)$, the biased CCF $\hat{R}_{y_1y_2}(\tau)$ is given by

$$\hat{R}_{y_1y_2}(\tau) = \frac{1}{2\pi}\int_{-\omega_a}^{\omega_a} \hat{S}_{y_1y_2}(\omega) e^{j\omega(\tau-\tau_{\text{peak}})} d\omega = \frac{\omega_a K}{\pi} \frac{\sin\left(\omega_a(\tau-\tau_{\text{peak}})\right)}{\omega_a(\tau-\tau_{\text{peak}})}, \quad (6)$$

According to Eq. (6), $\hat{R}_{y_1y_2}(\tau)$ is the *sinc* function with argument of $\omega_a(\tau-\tau_{\text{peak}})$ multiplied by a constant given by $\omega_a K/\pi$. Such a function is shown in Fig. 7.

Figure 7 – Biased CCF $\hat{R}_{y_1y_2}(\tau)$ with $y_1(t)$ and $y_2(t)$ with frequency content up to ω_a in the frequency domain.

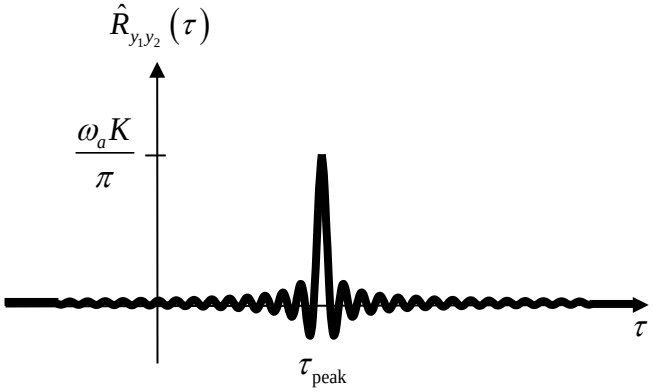

Source: elaborated by the author.

Although $\hat{R}_{y_1y_2}(\tau)$ does not result in an impulse (Dirac delta function) due to the finite bandwidth of the signals $y_1(t)$ and $y_2(t)$, it is possible to estimate approximately the time delay τ_{peak} through the value of τ that maximizes $\hat{R}_{y_1y_2}(\tau)$.

2.3 FREQUENCY RESPONSE FUNCTION OF A BURIED LEAKING PIPE

The location of a suspected leak in a buried pipe can be estimated by acoustic correlation, measuring the leak noise. In particular, it has been found that in many buried plastic water pipes, leak noise propagates mostly at low frequencies, below about 200 Hz, because of the high levels of damping in the pipe-wall, and the radial motion of the pipe-wall due to the coupling between the fluid and the pipe (BRENNAN *et al.*, 2016). The wave responsible for propagating the noise is a low-frequency, non-dispersive, axisymmetric, coupled structural-fluid wave located well below the ring frequency (MUGGLETON *et al.*, 2002; MUGGLETON et al., 2004a).

Figure 8 – Schematic diagram of a pipe with the leak pressure $P_l(\omega)$ and the pressure $P_x(\omega)$ measured at a distance x from the leak.

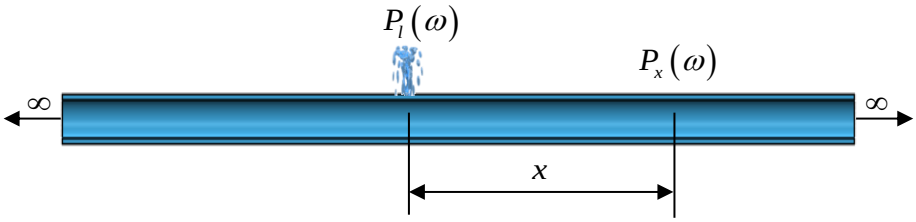

Source: elaborated by the author.

Fig. 8 shows the leak pressure $P_l(\omega)$ and the pressure $P_x(\omega)$, measured at a distance x from the leak. In the frequency range where the wavelength of the predominantly fluid-borne wave is much greater than the diameter of the pipe (which is the case considered in this work), the acoustic pressure can be considered to be uniform across the cross-section. So, the FRF $G^p(\omega, x)$ between the leak pressure $P_l(\omega)$ and the pressure $P_x(\omega)$ is given by (PINNINGTON; BRISCOE, 1994)

$$G^p(\omega, x) = \frac{P_x(\omega)}{P_l(\omega)} = e^{-jkx}, \tag{7}$$

where $j = \sqrt{-1}$, x is the distance between the leak and the measurement position, and k is the wavenumber which describes the spatial frequency of a wave, measured in radians per unit distance. The prediction of the wavenumber for a buried pipe is described in more detail in Appendix A.

Figure 9 – Radial displacement of an infinitesimal section of the pipe-wall.

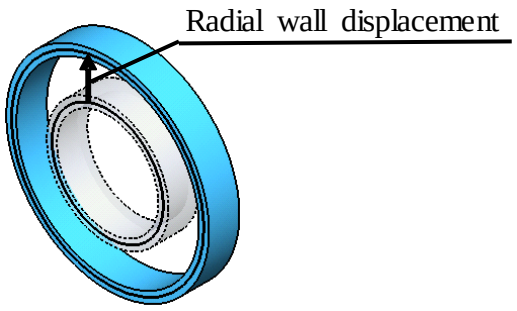

Source: elaborated by the author.

Eq. (7) provides the relationship between the pressure measured at a distance x from the leak and the pressure of the leak. Therefore, $P_x(\omega)$ can be calculated by the combination of $G^p(\omega, x)$ and $P_l(\omega)$. However, there are some situations that measuring acceleration in the radial direction of the pipe is more practical than measuring acoustic pressure, since the internal access of the pipe can be difficult. To determine the relationship between the acceleration at the distance x from the leak and the leak pressure, it is necessary to determine the relationship between the radial displacement of the pipe-wall and the internal pressure. Fig. 9 shows the radial displacement of an infinitesimal section of the pipe-wall. At low frequencies, well below the pipe ring frequency, the radial wall displacement amplitude $W_x(\omega)$ of the pipe-wall caused by the pressure $P_x(\omega)$ is given by (GAO *et al.*, 2005)

$$W_x(\omega) = \frac{P_x(\omega) a^2}{E_{\text{pipe}} h}, \tag{8}$$

where a, h are the mean pipe radius and wall thickness and E_{pipe} is the Young's modulus of pipe-wall material.

The Frequency Response Function (FRF) $G^d(\omega, x)$ between the leak pressure $P_l(\omega)$ and the radial wall displacement $W_x(\omega)$, at a distance x from the leak, is

$$G^d(\omega, x) = \frac{W_x(\omega)}{P_l(\omega)} = \frac{a^2}{E_{\text{pipe}} h} e^{-jkx}. \tag{9}$$

To calculate the FRF $G^a(\omega, x)$, which is the relationship between the acceleration of the pipe-wall and the leak pressure, it is noted that $G^a(\omega, x) = -\omega^2 G^d(\omega, x)$ to give

$$G^a(\omega, x) = -\frac{a^2 \omega^2}{E_{\text{pipe}} h} e^{-jkx}. \tag{10}$$

Since the sensors 1 and 2 are positioned at the distances d_1 and d_2 respectively according to Fig. 3, the FRFs $G^a(\omega, x)$ between the leak and the sensor 1 and between the leak and sensor 2 are given by Eq. (10), with $x = d_1$ and $x = d_2$ respectively.

Table 1 – Parameters of the MDPE pipe and soil.

Parameters	MDPE	Soil
a [m]	0.0845	-
h [m]	1.1×10^{-2}	-
Density [kg/m³]	900	1500
Young's modulus [N/m²]	2×10^{9}	-
Bulk's modulus [N/m²]	-	4×10^{7}
Shear modulus [N/m²]	-	1.5×10^{7}
Poisson's ratio	0.4	-
Material loss factor	0.06	-

Source: parameters extracted from Gao *et al.* (2017).

Figure 10 – FRFs $G^a(\omega, x)$ considering the parameters of the MDPE pipe and soil from Tab. 1. $G^a(\omega, x)$ with $x = 3$ m is given by the line ▬ and $G^a(\omega, x)$ with $x = 5$ m is given by the line ▪▪.

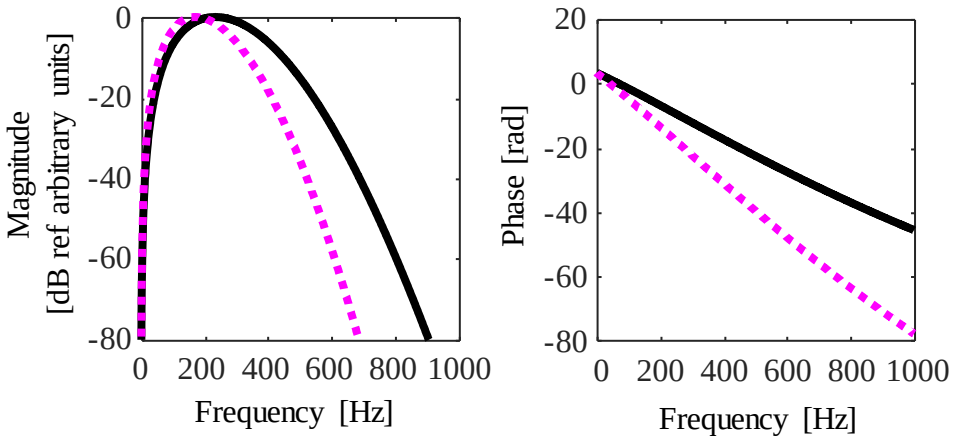

(a) Normalised magnitude (b) Unwrapped phase

Source: elaborated by the author.

An example of $G^a(\omega, x)$ was calculated considering the prediction of the wavenumber k in Appendix A and the parameters of the Medium Density Polyethylene (MDPE) pipe and soil retrieved from Gao *et al.* (2017). The values of such parameters can be found in Tab. 1. Both FRFs are shown in Fig. 10 in terms of magnitude and unwrapped phase.

2.4 IMPULSE RESPONSE FUNCTION OF A BURIED LEAKING PIPE

The Impulse Response Functions (IRFs) $g^a(t, x)$ between the acceleration of the pipe-wall (at a distance x from the leak) and the leak pressure is calculated by the inverse Fourier transform of $G^a(\omega, x)$, i.e. $g^a(t, x) = F^{-1}\{G^a(\omega, x)\}$ where $F^{-1}\{\ \}$ is the inverse Fourier transform operator. Using the inverse Fourier transform of the FRFs in Fig. 10, the IRFs $g^a(t, x)$ between the leak and the sensor 1 and between the leak and the sensor 2 were calculated considering $x = d_1$ and $x = d_2$ respectively. Both IRFs are shown in Fig. 11.

Figure 11 – Normalized IRFs $g^a(t, x)$ considering the parameters of the MDPE pipe and soil from Tab. 1. $g^a(t, x)$ with $x = 3$ m is given by the line ▬ and $g^a(t, x)$ with $x = 5$ m is given by the line ▪▪▪.

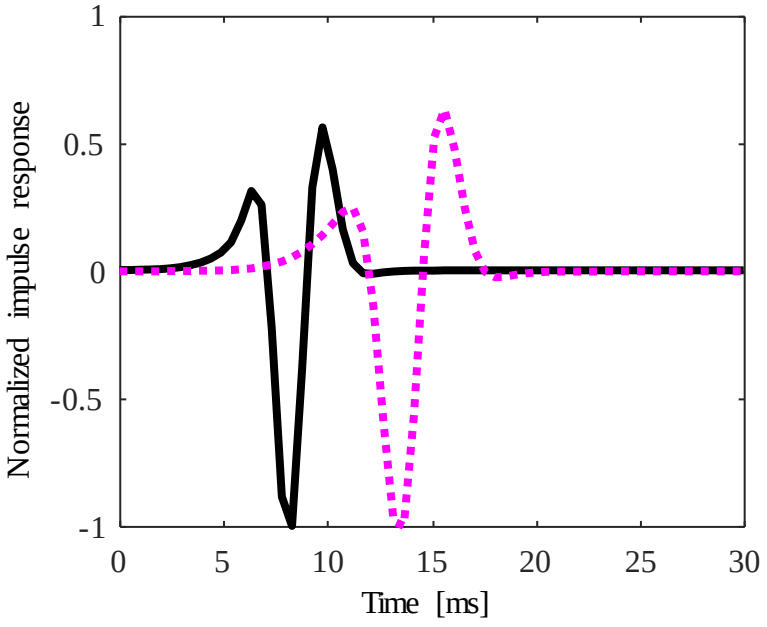

Source: elaborated by the author.

Note that each function is normalized by the respective maximum absolute value and are represented up to the interval of 30 ms.

2.5 LEAK NOISE SIMULATION USING THE IMPULSE RESPONSE FUNCTION OF A BURIED LEAKING PIPE

Detecting leaks in buried pipes using acoustic correlation requires that the leak noise is measured either side of a suspected leak. The difference in arrival times, or time delay, τ_{peak} of the signals measured by both sensors is estimated by the calculation of the CCF (or CCC) and the phase of CPSD between such signals. To simulate this situation, the time series $y_1(t)$ and $y_2(t)$ need to be generated from a mathematical model.

Since it is assumed that leak noise is represented by white noise with finite bandwidth, such a generation results the synthesized leak noise $\bar{y}_x(t)$, given by the convolution of a white noise signal $z(t)$ with the IRFs $g^a(t,x)$ of the buried pipe, which is given by

$$\bar{y}_x(t) = g^a(t,x) \otimes z(t), \tag{11}$$

where $\otimes$ is the convolution operator.

Since the sensors 1 and 2 are positioned at the distances d_1 and d_2, the synthesized leak noise $\bar{y}_1(t)$ and $\bar{y}_2(t)$ are given by the convolution of $z(t)$ with the IRFs $g^a(t,x)$, where $x = d_1$ and $x = d_2$ respectively. A schematic diagram is shown in Fig. 12.

Figure 12 – Schematic diagram of the synthetized leak noise $\bar{y}_1(t)$ and $\bar{y}_2(t)$ resulted from the convolution of white noise $z(t)$ and the IRFs $g^a(t,d_1)$ and $g^a(t,d_2)$.

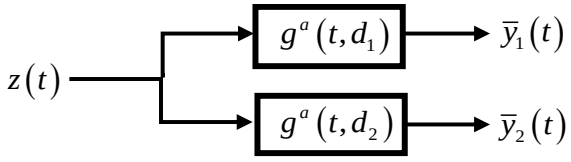

Source: elaborated by the author.

2.6 COMBINING THE ACOUSTIC CORRELATION WITH THE BURIED LEAKING PIPE MODEL

The CPSD $S_{\bar{y}_1\bar{y}_2}(\omega)$ of the synthesized signals $\bar{y}_1(t)$ and $\bar{y}_2(t)$ can be obtained by (GAO *et al.*, 2004)

$$S_{\bar{y}_1\bar{y}_2}(\omega) = \frac{1}{2\pi} \lim_{T\to\infty} E\left[\frac{\bar{Y}_1^*(\omega)\bar{Y}_2(\omega)}{T}\right] = S_{zz}(\omega)\Psi_{\bar{y}_1\bar{y}_2}(\omega), \tag{12}$$

where $\bar{Y}_1^*(\omega)$ and $\bar{Y}_2(\omega)$ are the Fourier transform of $\bar{y}_1(t)$ and $\bar{y}_2(t)$ respectively, and $*$ is the complex conjugate operator. $S_{zz}(\omega)$ is the Power Spectral Density (PSD) of $z(t)$ and $\Psi_{\bar{y}_1\bar{y}_2}(\omega) = G_1^{a*}(\omega, d_1)G_2^a(\omega, d_2)$.

The phase of CPSD $\Phi_{\bar{y}_1\bar{y}_2}(\omega)$ between the two signals is related to the time shift that the signals experience as they propagate through the pipe, and is given by (GAO *et al.*, 2004)

$$\Phi_{\bar{y}_1\bar{y}_2}(\omega) = \mathrm{Arg}\left(S_{\bar{y}_1\bar{y}_2}(\omega)\right), \tag{13}$$

where $\mathrm{Arg}(\ )$ is the argument operator.

Since multiplication in the frequency domain corresponds to convolution in the time domain, the CCF $R_{\bar{y}_1\bar{y}_2}(\tau)$ is given by

$$R_{\bar{y}_1\bar{y}_2}(\tau) = F^{-1}\left\{S_{\bar{y}_1\bar{y}_2}(\omega)\right\} = R_{zz}(\tau) \otimes \psi_{\bar{y}_1\bar{y}_2}(\tau), \tag{14}$$

where $R_{zz}(\tau)$ is the ACF of $z(t)$ given by $F^{-1}\left\{S_{zz}(\omega)\right\}$ and $\psi_{\bar{y}_1\bar{y}_2}(\tau) = F^{-1}\left\{\Psi_{\bar{y}_1\bar{y}_2}(\omega)\right\}$.

Similarly, the CCC $\rho_{\bar{y}_1\bar{y}_2}(\tau)$ is given by

$$\rho_{\bar{y}_1\bar{y}_2}(\tau) = \frac{R_{\bar{y}_1\bar{y}_2}(\tau)}{\sqrt{R_{\bar{y}_1\bar{y}_1}(0)R_{\bar{y}_2\bar{y}_2}(0)}}, \tag{15}$$

where $R_{\bar{y}_1\bar{y}_1}(0)$ and $R_{\bar{y}_2\bar{y}_2}(0)$ are the values of $R_{\bar{y}_1\bar{y}_1}(\tau)$ and $R_{\bar{y}_2\bar{y}_2}(\tau)$ given by $F^{-1}\left\{S_{\bar{y}_1\bar{y}_1}(\omega)\right\} = R_{zz}(\tau) \otimes \psi_{\bar{y}_1\bar{y}_1}(\tau)$ and $F^{-1}\left\{S_{\bar{y}_2\bar{y}_2}(\omega)\right\} = R_{zz}(\tau) \otimes \psi_{\bar{y}_2\bar{y}_2}(\tau)$ at $\tau = 0$. Note that $S_{\bar{y}_1\bar{y}_1}(\omega) = S_{zz}(\omega)\left|G_1^a(\omega)\right|^2$ and $S_{\bar{y}_2\bar{y}_2}(\omega) = S_{zz}(\omega)\left|G_2^a(\omega)\right|^2$.

Considering the MDPE pipe and soil with the parameters from Tab. 1 and the distances $d_1 = 3$ m and $d_2 = 5$ m, $\bar{y}_1(t)$ and $\bar{y}_2(t)$ were calculated through the convolution of white noise signal with the IRFs shown in Fig. 11. Such signals were used to estimate the time delay τ_{peak} between them by calculating the CSPD $S_{\bar{y}_1\bar{y}_2}(\omega)$, shown in terms of magnitude and phase in Fig. 13(a)-(b), and the CCC $\rho_{\bar{y}_1\bar{y}_2}(\tau)$, shown in Fig. 14.

Note that $S_{\bar{y}_1\bar{y}_2}(\omega)$ was calculated in two different ways. One way was using the Welch's modified periodogram method of spectral estimation (line ▬). Each signal was divided into 128 segments. Each segment was multiplied by a Hanning window, and 50% overlap was adopted between the segments. The CCFs of the averaged signals were calculated, and the CPSDs were determined by calculating the Fourier transform of the CCFs. A sampling frequency of 2,048 Hz was used together with a 2,048-point CPSD, resulting in a frequency resolution of approximately 1 Hz (OPPENHEIM; SCHAFER, 2011). And the other way was using the model given by Eq. (12) (line ▪▪).

The normalized magnitude shown in Fig. 13(a) means that the signals $\bar{y}_1(t)$ and $\bar{y}_2(t)$ are more related in the frequency components where the magnitude is larger (SHIN; HAMMOND, 2008). The same information can also be verified by calculating the coherence function $\gamma_{\bar{y}_1\bar{y}_2}(\omega)$, shown in Fig. 13(c), which is a normalized form of $S_{\bar{y}_1\bar{y}_2}(\omega)$ given by

$$\gamma_{\bar{y}_1\bar{y}_2}(\omega) = \frac{\left|S_{\bar{y}_1\bar{y}_2}(\omega)\right|^2}{S_{\bar{y}_1\bar{y}_1}(\omega) S_{\bar{y}_2\bar{y}_2}(\omega)}. \tag{16}$$

Note that $\gamma_{\bar{y}_1\bar{y}_2}(\omega)$ was also calculated in two different ways. One way was using the Welch's modified periodogram method of spectral estimation (line ▬), with the same parameters used to calculate $S_{\bar{y}_1\bar{y}_2}(\omega)$. And the other way was using Eq. (16) (line ▪▪).

Figure 13 – CPSD $S_{\bar{y}_1\bar{y}_2}(\omega)$ and coherence $\gamma_{\bar{y}_1\bar{y}_2}(\omega)$ considering the parameters of the pipe and soil from Tab. 1. $S_{\bar{y}_1\bar{y}_2}(\omega)$ and $\gamma_{\bar{y}_1\bar{y}_2}(\omega)$ obtained through the Welch's modified periodogram method is given by the line ▬, and $S_{\bar{y}_1\bar{y}_2}(\omega)$ and $\gamma_{\bar{y}_1\bar{y}_2}(\omega)$ obtained through Eq. (12) and Eq. (16) are given by the line ▬.

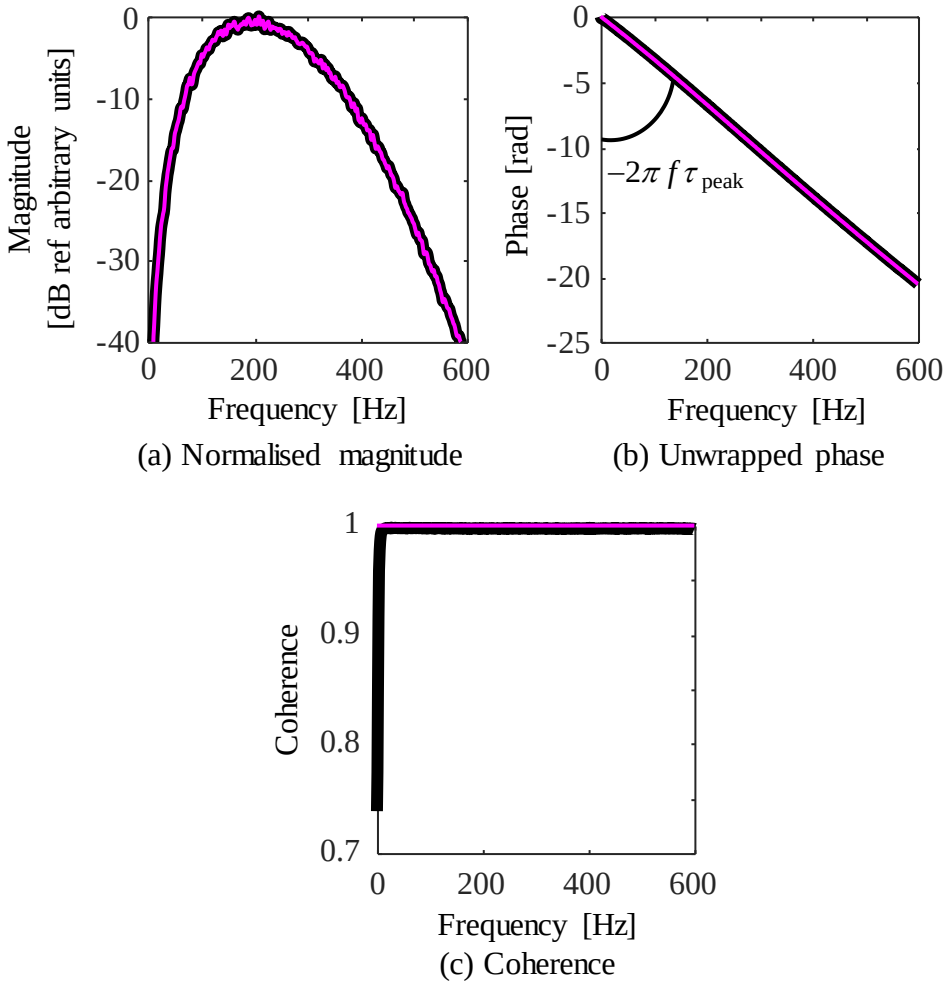

Source: elaborated by the author.

The phase of $S_{\bar{y}_1\bar{y}_2}(\omega)$, shown in Fig. 13(b), shows whether frequency components in one signal 'lag' or 'lead' the components at the same frequency in the other signal (SHIN; HAMMOND, 2008). Considering the bandwidth where both signals are more related (which is approximately up to 600 Hz), the time delay τ_{peak} provided by the slope of the phase of $S_{\bar{y}_1\bar{y}_2}(\omega)$ is approximately equal to 5.4 ms.

Figure 14 – CCC $\rho_{\bar{y}_1\bar{y}_2}(\tau)$ calculated with the synthesized leak noise $\bar{y}_1(t)$ and $\bar{y}_2(t)$ considering the parameters of the pipe and soil from Tab. 1. $\rho_{\bar{y}_1\bar{y}_2}(\tau)$ obtained through the inverse Fourier transform of the Welch's modified periodogram method is given by the line ▬, and $\rho_{\bar{y}_1\bar{y}_2}(\tau)$ obtained through Eq. (15) is given by the line ▪▪.

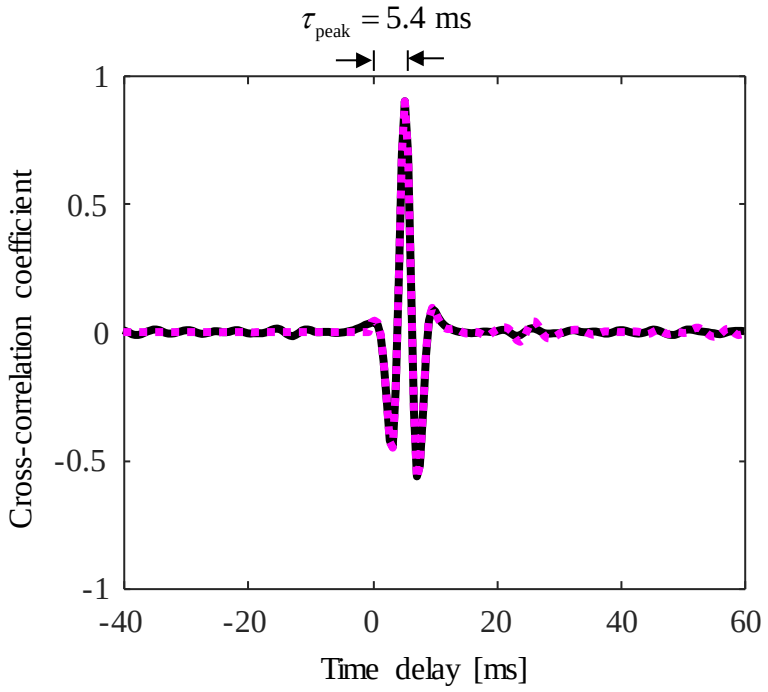

Source: elaborated by the author.

Since τ_{peak} is given by the argument τ that maximizes $R_{\bar{y}_1\bar{y}_2}(\tau)$, the time delay between $\bar{y}_1(t)$ and $\bar{y}_2(t)$ is given by the peak presented in the function shown in Fig. 14. So, τ_{peak} is equal to approximately 5.4 ms in this case, which corresponds to the same value obtained by the slope of the phase of $S_{\bar{y}_1\bar{y}_2}(\omega)$.

According to Eq. (30) in Appendix A, the wavespeed $c(\omega)$ is given by $c(\omega) = \omega / \text{Re}\{k(\omega)\}$. So, it is possible to estimate the mean wavespeed by calculating the mean value of $c(\omega)$ over the finite bandwidth. In this case, the mean value of $c(\omega)$ is equal to approximately 406.24 m/s. Therefore, since $d_1 + d_2 = 8$ in this case, the estimation gives that d_1 is equal to approximately 2.90 m according to Eq. (1). Note that the estimation gives a value which is close to the real value of d_1.

2.7 CONCLUSIONS

This chapter has given an overview of leak detection using acoustic correlation. Such a technique is able to detect leaks in buried pipes by measuring the difference in propagation times (or time delay) between the leak and each sensor positioned at either side of the suspected leak. The time delay estimation can be done in both domains by calculating the CCF (or CCC) and the CPSD between the leak noise measured by both sensors. A mathematical model is used to describe the pipe-wall acceleration response of a buried leaking pipe in frequency domain. Then, the simulation of a buried leaking pipe is done by the synthesis of leak noise, which is result of the convolution between white noise and the IRFs of the buried leaking pipe. Such functions were calculated by the inverse Fourier transform of the FRFs that represent the relationship between the pipe-wall accelerations and the leak pressure. An example of such simulation was done using the parameters of the soil and pipe from previous work, whose time delay was estimated in both domains using the CCC and the CPSD, which were compared with the model that combines the acoustic correlation with the buried leaking pipe model. Such a comparison resulted in good agreement and both functions provided the same time delay for the synthesized leak noise, which was used to estimate the distance between the leak and one of the sensors together with the wavespeed. Since it is intended to simulate leak noise, systems composed by power amplifiers and electrodynamic shakers are used to replicate the synthesized leak noise in form of vibration. So, the next chapter describes the compensation for the dynamics of such systems in order to get synthesized leak noise, in form of vibration, without the influence of the dynamics of such devices.

3 COMPENSATING THE DYNAMICS OF THE VIRTUAL PIPE TEST RIG

3.1 INTRODUCTION

The main objective of this work is to design a bench-top device to simulate the vibrations of a buried pipe due to a leak. This device is composed by a computer (that generates the synthesized leak noise with the model introduced in Chapter 2), a dual-channel power amplifier and two shakers. Devices such as power amplifiers and shakers have dynamics that can affect the vibrations generated by them (BRENNAN *et al.*, 2016). Thus, the vibrations provided by such devices in the virtual pipe test rig are a combination of the devices and the response of the model of a buried leaking pipe. One way to avoid this problem is to compensate for the dynamics of the power amplifiers and the two shakers of the virtual pipe test rig, since the intention is to build a device that reproduces the same behavior as a buried leaking pipe. This compensation is achieved by designing filters based on the FRFs of the systems and they are called compensators. To illustrate the compensator design approach using a system whose acceleration response is given by simple functions in both domains, the first section of this chapter presents the dynamics and the compensator design for a Single Degree of Freedom (SDOF) system. The compensation performance of the SDOF system is checked in both domains by combining, within the computer, the response of the compensator and the acceleration response of the SDOF system. Following the introduction of the compensator design, the dynamics of the virtual pipe systems, including the power amplifiers and the two shakers in series, is presented in the second section. The compensators for the virtual pipe systems are designed and the performance is checked in both domains by combining, within the computer, the response of the compensators and the acceleration response of the systems. Given the encouraging results, a laboratory experiment was carried out by filtering a white noise with the compensators before supplying the signal to the power amplifiers and the shakers. A spectral estimator was used to calculate the FRFs of the compensated virtual pipe systems and the IRFs were also estimated by calculating the inverse Fourier transform of the FRFs.

3.2 INTRODUCTION OF THE COMPENSATOR DESIGN

The following subsections illustrate the compensator design approach by determining a compensator for a SDOF system. The first subsection presents the dynamics of a SDOF system in both domains, giving the FRF and the IRF of the system. The second subsection presents the compensator design for a SDOF system. The third subsection describes the modified compensator design for a SDOF system, and presents the performance of the compensator by combining the response of the modified compensator and the acceleration response of the SDOF system.

3.2.1 Frequency response and impulse response functions of a single degree of freedom system

Fig. 15 shows a schematic diagram of a SDOF system. The terms m, k and c are the mass, stiffness and damping of the system respectively. The accelerance of a SDOF system $H^a(\omega)$, which is the FRF that provides the relationship between the acceleration $A(\omega)$ of the mass and the force $F(\omega)$ applied to the mass, is given by (SHIN; HAMMOND, 2008)

$$H^a(\omega) = \frac{A(\omega)}{F(\omega)} = \frac{-\omega^2}{k - m\omega^2 + j\omega c}, \tag{17}$$

Figure 15 – Schematic diagram of a SDOF system.

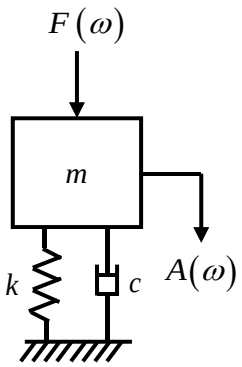

Source: elaborated by the author.

The IRF for acceleration $\ddot{h}(t)$ of a SDOF system is the second derivative of the IRF for displacement $h(t)$ of a SDOF system, which is derived in Appendix B, and is given by

$$\ddot{h}(t)=\frac{\delta(t)}{m}+\frac{1}{m\omega_d}e^{-\zeta\omega_n t}\left(\left(\left(\zeta\omega_n\right)^2-\omega_d^2\right)\sin\left(\omega_d t\right)-2\zeta\omega_n\omega_d\cos\left(\omega_d t\right)\right), \tag{18}$$

where the term $\delta(t)$ is the Delta function. The terms ω_n and ω_d are the undamped natural frequency and the damped natural frequency of the SDOF system, respectively, given by $\omega_n=\sqrt{k/m}$ and $\omega_d=\omega_n\sqrt{1-\zeta^2}$. The term ζ is the damping ratio of the SDOF system and is given by $\zeta=c\Big/\left(2\sqrt{mk}\right)$.

Equation (17) provides the relationship, in the frequency domain, between the acceleration $A(\omega)$ and the force $F(\omega)$ of the SDOF system. Therefore, the acceleration $A(\omega)$ is given by $A(\omega)=H^a(\omega)F(\omega)$. Equation (18) provides the acceleration response of the mass in the time domain when a force described by $\delta(t)$ is applied. Since multiplication in one domain corresponds to convolution in the transformed domain, the acceleration $a(t)$, which is the inverse Fourier transform of $A(\omega)$, is given by $a(t)=\ddot{h}(t)\otimes f(t)$ where $f(t)$ is the inverse Fourier transform of $F(\omega)$ and $\ddot{h}(t)$ is the inverse Fourier transform of $H^a(\omega)$. Thus, the FRF $H^a(\omega)$ can be calculated from Eq. (17) or by the Fourier transform of $\ddot{h}(t)$, given by Eq. (18), and the IRF $\ddot{h}(t)$ can be calculated from Eq. (18) or by the inverse Fourier transform of $H^a(\omega)$, given by Eq. (17).

An example of $H^a(\omega)$ is shown in Fig. 16, in terms of magnitude and phase, up to a frequency of 1.0×10^3 Hz. It was calculated considering the parameters of the SDOF system shown in Tab. 2. Note that such a function was calculated by Eq. (17) (line ▬) and by the Fourier transform of Eq. (18) (line ▪▪).

Table 2 – Parameters of the SDOF system.

m [kg]	k [N/m]	ζ
1.0	1.0×10^4	0.1

Source: elaborated by the author.

Figure 16 – FRF $H^a(\omega)$ of the SDOF system considering the parameters from Tab. 2. $H^a(\omega)$ calculated through Eq. (17) is given by the line ▬, and $H^a(\omega)$ calculated by the Fourier transform of Eq. (18) is given by the line ▪▪.

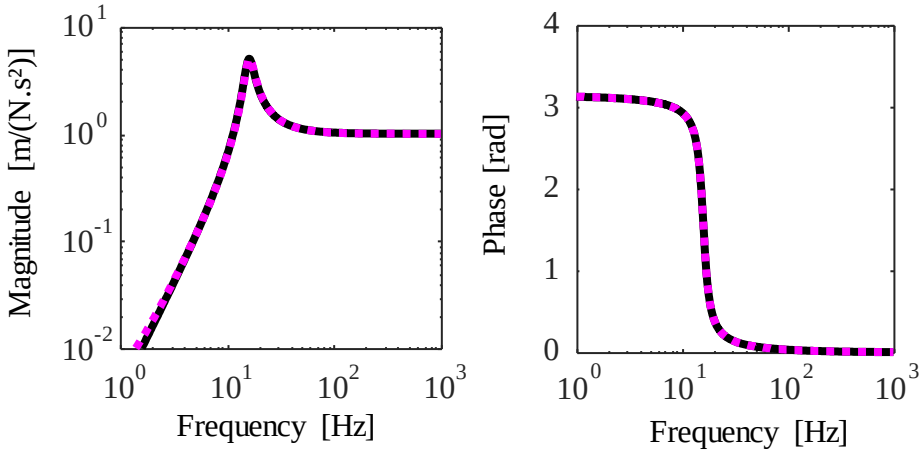

(a) Magnitude (b) Phase

Source: elaborated by the author.

An example of $\ddot{h}(t)$ is shown in Fig. 17 up to the interval of 600 ms. It was also calculated considering the parameters shown in Tab. 2. Note that such a function was calculated by Eq. (18) (line ▬) and by the inverse Fourier transform of Eq. (17) (line ▪▪). The impulse at the beginning of $\ddot{h}(t)$ in Fig. 17(a) is given by the term $\delta(t)/m$ in Eq. (18) (such a term in $\ddot{h}(t)$ is explained in more detail in Appendix B). Note that Fig. 17(b) shows a zoomed portion of $\ddot{h}(t)$ shown in Fig. 17(a), in which it is verified good agreement between the line ▬ and the line ▪▪.

Figure 17 – IRF $\ddot{h}(t)$ of the SDOF system considering the parameters from Tab. 2. $\ddot{h}(t)$ calculated through Eq. (18) is given by the line ▬, and $\ddot{h}(t)$ calculated by the inverse Fourier transform of Eq. (17) is given by the line ▪▪.

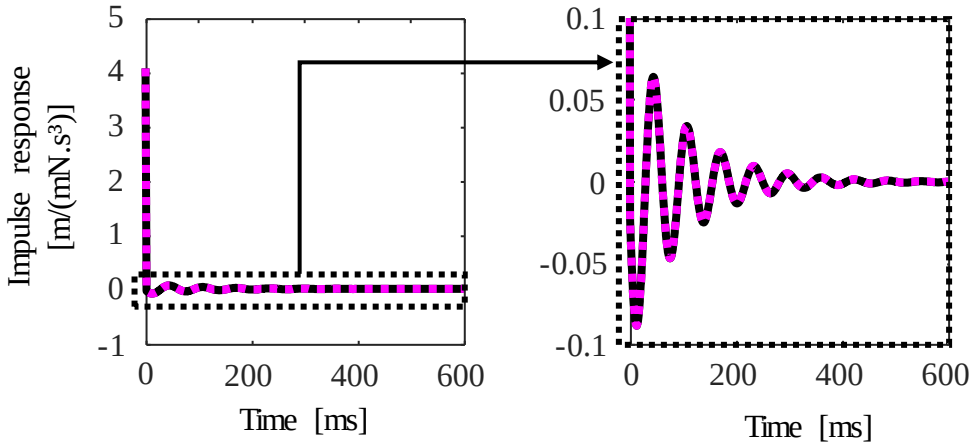

(a) IRF $\ddot{h}(t)$ (b) Zoomed IRF $\ddot{h}(t)$

Source: elaborated by the author.

3.2.2 Compensator design for a single degree of freedom system

A simple way of compensating for the dynamics of a system is to linearly combine in the frequency domain the response of the system with the response of the compensator. Using the SDOF system to illustrate the approach, in which the FRF is given by $H^a(\omega)$, the compensator $\bar{H}^a(\omega)$ for this system is given by $\bar{H}^a(\omega) = 1/H^a(\omega)$.

Note that $H^a(\omega)$, which is the accelerance of the SDOF system given by Eq. (17), is equal to 0 when $\omega = 0$. Since $\lim_{\omega \to 0} \bar{H}^a(\omega) = \infty$, the compensator $\bar{H}^a(\omega)$ has extremely large values at frequencies close to 0 which are impossible to compute. To deal with this issue, the values of $H^a(\omega)$ are clipped once they are smaller than a threshold value. This threshold value must be chosen based on a trade-off between the minimal value of $H^a(\omega)$ that can be computed and the maximum bandwidth in which $H^a(\omega)$ is clipped. In this work, the threshold value for the FRF $H^a(\omega)$ was approximately of 3.0×10^{-4} m/(N.s²), clipping the function up to a frequency of approximately 0.28 Hz.

The combination between the FRF $H^a(\omega)$ and the compensator $\bar{H}^a(\omega)$, shown in Fig. 18, results in the FRF $H^a_{\text{com}}(\omega)$ of the compensated SDOF system given by

$$H^a_{\text{com}}(\omega) = \bar{H}^a(\omega) H^a(\omega) = \frac{\bar{A}(\omega)}{F(\omega)}. \tag{19}$$

where $\bar{A}(\omega)$ is the acceleration provided by the compensated SDOF system. Note that $\bar{A}(\omega)$ can also be obtained by $\bar{A}(\omega) = H^a(\omega)\bar{F}(\omega)$ in which $\bar{F}(\omega) = \bar{H}^a(\omega)F(\omega)$, i.e. the acceleration $\bar{A}(\omega)$ of the compensated SDOF system is also obtained when the force $\bar{F}(\omega)$, which is the combination of the force $F(\omega)$ and the compensator $\bar{H}^a(\omega)$, is applied to the SDOF system.

Figure 18 – Schematic diagram of the FRF $H^a_{\text{com}}(\omega)$ of the compensated SDOF system.

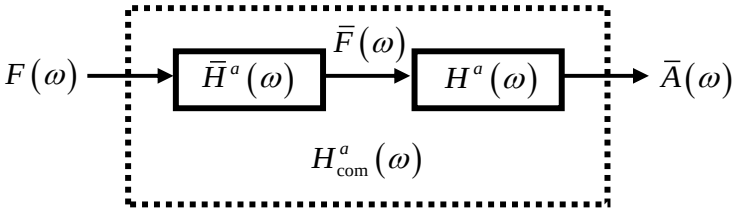

Source: elaborated by the author.

Note that $\bar{A}(\omega) \approx F(\omega)$ because $H^a_{\text{com}}(\omega) \approx \bar{H}^a(\omega)H^a(\omega)$ and $\bar{H}^a(\omega) \approx 1/H^a(\omega)$. Thus, the magnitude of $H^a_{\text{com}}(\omega)$ is given by a unitary constant and the phase of $H^a_{\text{com}}(\omega)$ is given by a zero constant. This means that the compensated SDOF system provides the acceleration $\bar{A}(\omega)$ that contains the compensated effects of the dynamics of the SDOF system given by $H^a(\omega)$.

Although $\bar{H}^a(\omega)$ is able to compensate for the dynamics of a SDOF system implemented in the computer, it is not possible to compensate completely the effects of the dynamics of real systems by simply combining the compensators in this form with such systems. This occurs because there is a time delay associated with the real systems, since it takes a finite time for a signal to pass through them. So, to compensate adequately the effects of the dynamics of real systems, a time delay must be added to the compensator. This time delay ensures that the

compensator has a time delay rather than a time advance and that the compensated system is causal.

The IRF $\bar{h}^a(t)$ of the compensator, in which $0 \le t \le T$ and T is the finite interval in which the function is represented, is calculated by the inverse Fourier transform of $\bar{H}^a(\omega)$. A time delay α is then added to $\bar{h}^a(t)$ resulting in the modified IRF given by

$$\bar{h}^a(t) = \bar{h}^a(t+\alpha) \tag{20}$$

where, in this dissertation the time delay is set so that $\alpha = T/2$, for convenience.

Figure 19 – IRF $\bar{h}^a(t)$ of the compensator for the SDOF system considering the parameters from Tab. 2. The plot of $\bar{h}^a(t)$ is given by the line ▬, and the zone given by the lines ▪▪ shows the segment of $\bar{h}^a(t)$ that contains the compensation for the dynamics of the SDOF system.

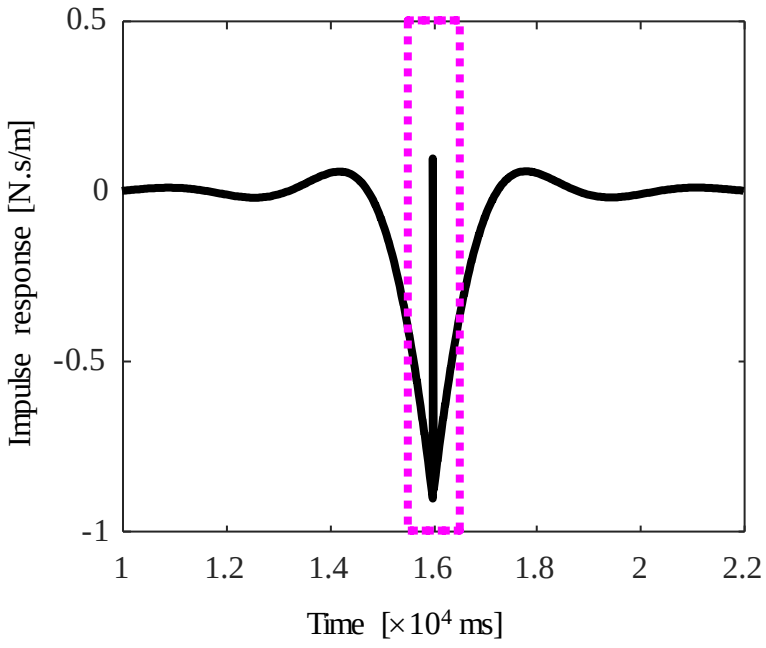

Source: elaborated by the author.

Considering the example of SDOF system, whose parameters are shown in Tab. 2 and the FRF and the IRF are shown in Figs. 16-17, the IRF $\bar{h}^a(t)$ of the compensator was calculated through the inverse Fourier transform of $\bar{H}^a(\omega)$ with T equal to approximately 3.2×10^4 ms. Then, the time delay α, which is equal to approximately 1.6×10^4 ms, was set resulting in the modified IRF shown in Fig. 19, whose plot is given by the line ▬. It is shown from 1.0×10^4 ms up to 2.2×10^4 ms.

3.2.3 Modified compensator design for a single degree of freedom system

Although the compensator presented in the previous section could be used for compensating the dynamics of the SDOF system, it is a function described in a time interval up to 3.2×10^4 ms (note that Fig. 19 shows a segment between 1.0×10^4 ms and 2.2×10^4 ms). This is thought to be inefficient as the compensator could be represented accurately by a minor segment of $\bar{h}^a(t)$, since this function tends to zero for both sides of the impulse at $T/2$. Therefore, the segment of $\bar{h}^a(t)$ that contains the compensation for the dynamics of the system is within the interval whose middle is at $T/2$. The length of the interval must be chosen considering a trade-off between the length of $\bar{h}^a(t)$ that is intended to be truncated and the minimal interval in which this function can be truncated, without losing information regarding the compensation for the dynamics of the system. In the example of this dissertation, the middle of $\bar{h}^a(t)$ is at 1.6×10^4 ms and the truncated segment is within the zone in Fig. 19 given by the lines ▪▪. Such a segment is described from approximately 1.55×10^4 ms to 1.65×10^4 ms, that corresponds to a time interval of approximately 1.0×10^3 ms.

By removing the segments of $\bar{h}^a(t)$ that are outside the zone given by the lines ▪▪, a truncated version of $\bar{h}^a(t)$ is shown in Fig. 20(a). Note that the compensator is now described in a time interval of approximately 1.0×10^3 ms instead of 3.2×10^4 ms, decreasing the time interval in which the function is described by a factor of 32.

Figure 20 – Truncated version of $\bar{h}^a(t)$ and modified IRF $\hat{h}^a(t)$ of the compensator for the SDOF system considering the parameters from Tab. 2. The plots of $\bar{h}^a(t)$ and $\hat{h}^a(t)$ are given by the lines ▬, and the zones given by the lines ▪▪ show the segment of $\bar{h}^a(t)$ that was extracted from Fig. 19.

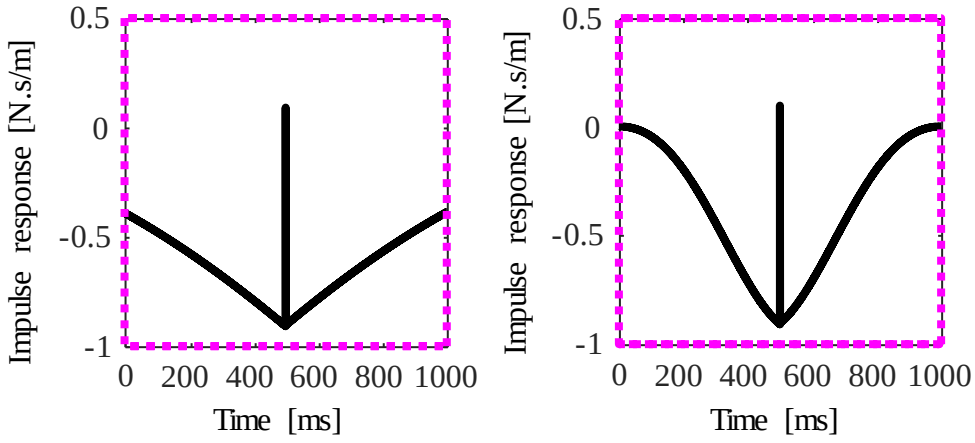

(a) Truncated version of $\bar{h}^a(t)$ (b) Modified IRF $\hat{h}^a(t)$

Source: elaborated by the author.

Fig. 20(a) shows the truncated segment of $\bar{h}^a(t)$. Note that such a truncation is similar to multiply $\bar{h}^a(t)$ by a rectangular window. Although the segment of $\bar{h}^a(t)$ can be used to compensate for the dynamics of the system, the procedure of truncating (or multiplying by a rectangular window) in the time domain can result in nonuniform convergence in the frequency domain, known Gibbs phenomenon. To minimize this issue, it is necessary a less abrupt truncation by tapering the segment of $\bar{h}^a(t)$ smoothly to zero at each end of the function (OPPENHEIM; SCHAFER, 2011). In this dissertation, the segment of $\bar{h}^a(t)$ is multiplied by a Hanning window described approximately between 0 and 1.0×10^3 ms. This operation results in the modified IRF $\hat{h}^a(t)$, shown in Fig. 20(b), with the beginning and end of this function tapered smoothly to zero.

To verify if the modified compensator with IRF $\hat{h}^a(t)$ is able to compensate for the dynamics of the SDOF system, the IRF of the compensated SDOF system $\ddot{h}_{\text{com}}(t)$ is calculated through the convolution of $\hat{h}^a(t)$ and $\ddot{h}(t)$, i.e. $\ddot{h}_{\text{com}}(t) = \hat{h}^a(t) \otimes \ddot{h}(t)$. The results are shown in Fig. 21. Note that $\ddot{h}_{\text{com}}(t)$, given by the line ▪▪ in Fig. 21, is approximately a delayed delta function and $\ddot{h}(t)$, given by the line ▬ in Fig. 21, is the IRF given by Eq. (18) that contains the dynamics of the SDOF system. If the force $f(t)$ is filtered by the compensator $\hat{h}^a(t)$ and the filtered force $\hat{f}(t)$ is supplied to the SDOF system, as shown in Fig. 22, the compensated SDOF system provides the acceleration $\hat{a}(t)$ which has the compensated dynamics of the SDOF system. Furthermore, the acceleration $\hat{a}(t)$ also contains the same time delay as $\ddot{h}_{\text{com}}(t)$.

Figure 21 – IRF $\ddot{h}(t)$ of the SDOF system and IRF $\ddot{h}_{\text{com}}(t)$ of the compensated SDOF system. $\ddot{h}(t)$ is given by the line ▬ and $\ddot{h}_{\text{com}}(t)$ is given by the line ▪▪.

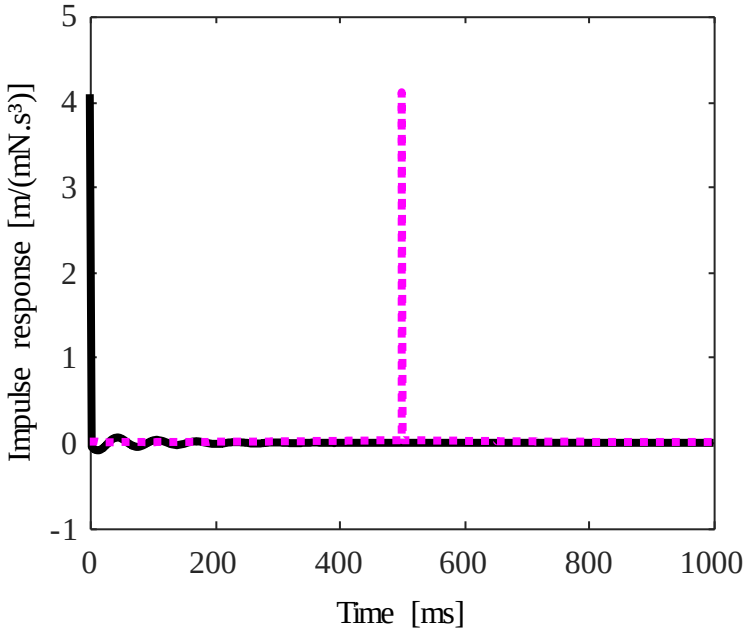

Source: elaborated by the author.

Figure 22 – IRF $\ddot{h}_{\text{com}}(t)$ of the compensated SDOF system given by the convolution of $\hat{h}^{a}(t)$ and $\ddot{h}(t)$.

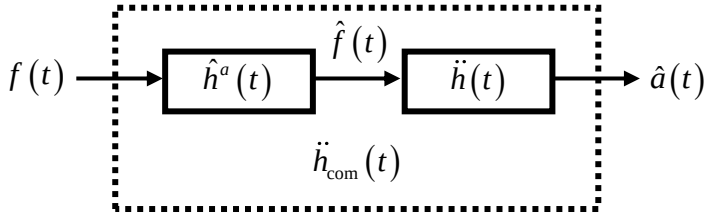

Source: elaborated by the author.

To verify the compensation in the frequency domain, the FRF $H^{a}_{\text{com}}(\omega)$ of the compensated SDOF system was calculated using the Fourier transform of $\ddot{h}_{\text{com}}(t)$. The results are shown in Fig. 23 in terms of magnitude and unwrapped phase. Note in Fig. 23(a) and Fig. 23(b) that above about 3 Hz, the magnitude of $H^{a}_{\text{com}}(\omega)$ is approximately given by a unitary constant. This is expected since the compensator was designed based on the FRF $H^{a}(\omega)$, which was clipped to avoid the singularity $\lim_{\omega \to 0} \bar{H}^{a}(\omega) = \infty$. Therefore, the compensation for the dynamics of the SDOF system only exists for frequencies above approximately 3 Hz. Gibbs phenomenon exists up to approximately 30 Hz caused by the windowing effects of $\ddot{h}_{\text{com}}(t)$. This is a result from the convolution of the IRF $\hat{h}^{a}(t)$, that is a windowed version of $\bar{h}^{a}(t)$, and the IRF $\ddot{h}(t)$.

Above 3 Hz the compensated SDOF system is approximately a pure delay system since the magnitude of $H^{a}_{\text{com}}(\omega)$, shown in Fig. 23(a) and Fig. 23(b), is approximately a unitary constant and the unwrapped phase of $H^{a}_{\text{com}}(\omega)$, shown in Fig. 23(c), is a straight line with a constant slope.

Figure 23 – FRF $H^{a}_{\text{com}}(\omega)$ of the compensated SDOF system.

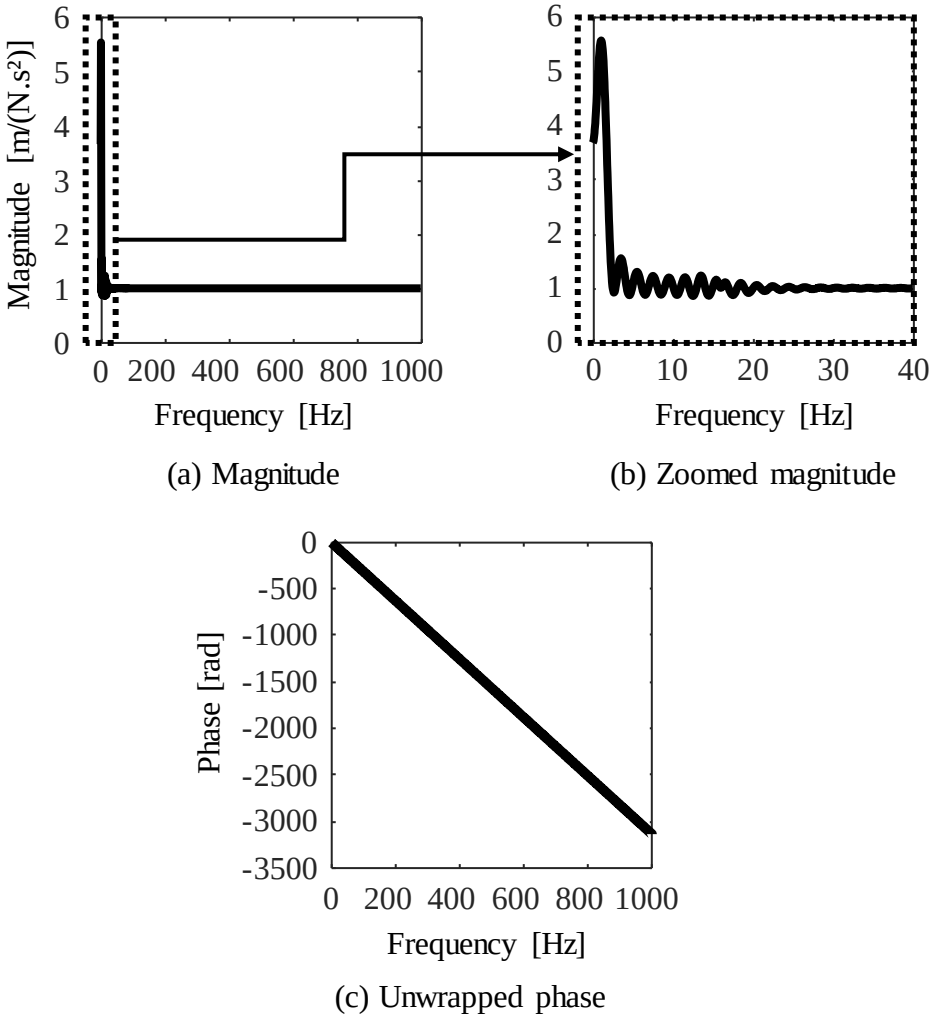

(a) Magnitude (b) Zoomed magnitude

(c) Unwrapped phase

Source: elaborated by the author.

Although the compensation does not exist for the entire bandwidth of the system, this result is considered satisfactory because this approach is used to compensate for the dynamics of the systems used to simulate leak noise in a buried pipe. The compensation of these systems at frequencies below about 10 Hz is not necessary, since the signals provided by the leak noise simulation has no influence at these frequencies. Gibbs phenomenon in the magnitude of $H^{a}_{\text{com}}(\omega)$, caused by the windowing effects of $\ddot{h}_{\text{com}}(t)$, are also not a problem for the performance of the compensator since it is narrowband and has a small magnitude when compared with the magnitude of $H^{a}_{\text{com}}(\omega)$.

3.3 COMPENSATOR DESIGN FOR THE POWER AMPLIFIERS AND THE SHAKERS OF THE VIRTUAL PIPE TEST RIG

The following subsections present the compensator design for the power amplifiers and the shakers of the virtual pipe test rig, using the approach illustrated in the previous section. The first subsection presents the dynamics of the power amplifiers and the two shakers cascaded in series, giving the frequency response and the impulse response functions of the virtual pipe systems. The second subsection presents the compensator design for the virtual pipe systems. The third subsection presents the modified compensator design for the virtual pipe systems, and the performance of the compensation by combining the response of the modified compensators and the acceleration response of the virtual pipe systems.

3.3.1 Frequency response and impulse response functions of the virtual pipe systems

The experimental arrangement for the virtual pipe test rig is shown in Fig. 24. It consists of a computer, a dual-channel power amplifier and two LDS V101 shakers, which are used to generate vibration representative of measured leak noise. The power amplifier has a usable frequency range between approximately 20 Hz and 20 kHz, and the shakers have a usable frequency range between approximately 5 Hz and 12 kHz according to their manufacturer data. There are also two PCB 352C22 piezoelectric accelerometers, whose frequency range is between approximately 1 Hz and 10 kHz, and an LMS SCADAS data acquisition system to measure and record the signals which are used to estimate the FRFs and the IRFs of the systems.

Figure 24 – Virtual pipe test rig.

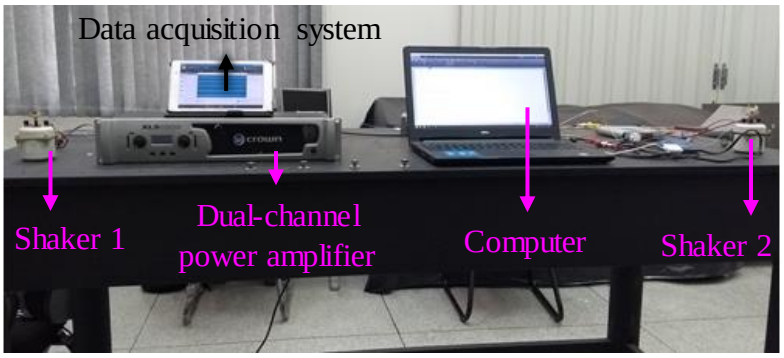

Source: elaborated by the author.

To simulate a leak in a buried pipe, the arrangement shown in Fig. 24 is divided in two independent systems, called virtual pipe system 1 and virtual pipe system 2, which are shown schematically in Fig. 25.

Figure 25 – Schematic diagram of the two systems of the virtual pipe test rig.

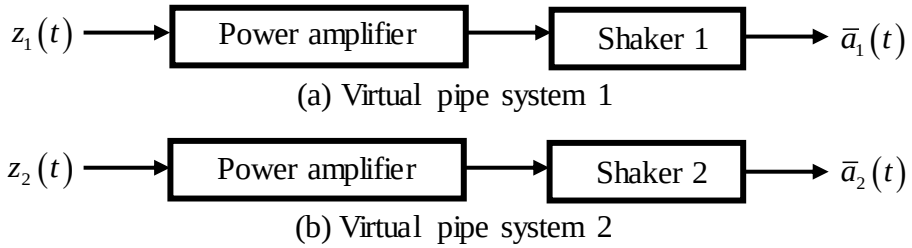

Source: elaborated by the author.

To determine the FRFs, white noise signals $z_1(t)$ and $z_2(t)$ were used as input signals to the virtual pipe systems 1 and 2, resulting the accelerations $\bar{a}_1(t)$ and $\bar{a}_2(t)$ respectively, that were used as output signals to the virtual pipe systems 1 and 2. The input signals and the output signals were measured in a time interval of 60 s with a sampling frequency of 8,192 Hz. The FRFs of both systems are denoted as $H_s^a(\omega)$, in which s is used to denote virtual pipe systems 1 and 2. A H_1 spectral estimator was used together with a sampling frequency of 8,192 Hz and 8,192 points to calculate the Fast Fourier Transform (FFT), giving a frequency resolution of approximately 1 Hz. The CPSD between the signals and the PSD of the input signal were calculated using the Welch's modified periodogram method, in which the signals were divided into 512 segments. Each segment was multiplied by a Hanning window, and 50% overlap was adopted between the segments (OPPENHEIM; SCHAFER, 2011). The FRFs for the systems in Fig. 25 are shown in Fig. 26 in terms of magnitude and unwrapped phase.

Figure 26 – FRFs $H_1^a(\omega)$ and $H_2^a(\omega)$ of the virtual pipe systems 1 and 2 respectively.

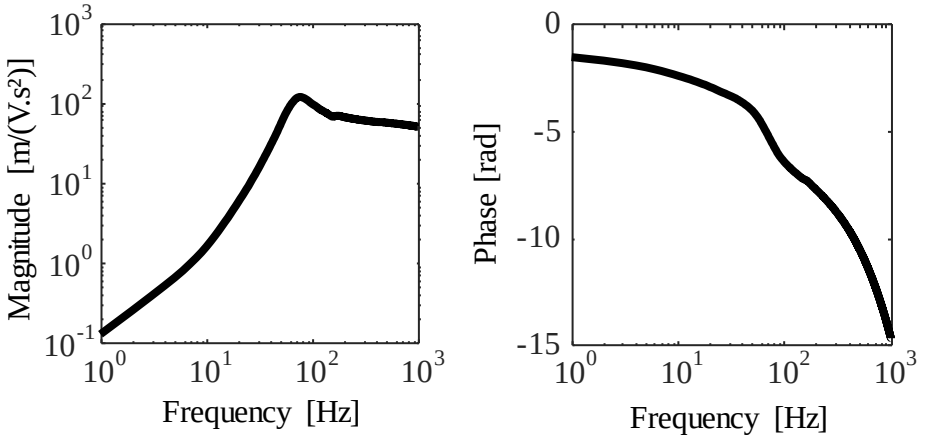

(a) Magnitude of $H_1^a(\omega)$ (b) Unwrapped phase of $H_1^a(\omega)$

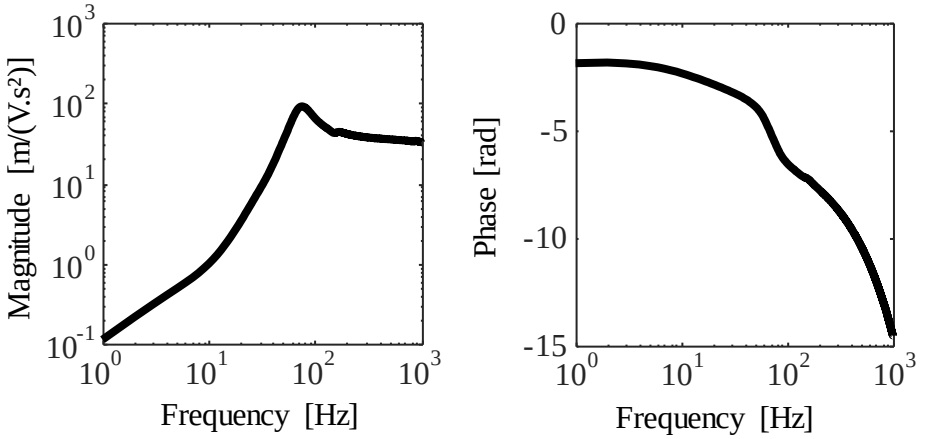

(c) Magnitude of $H_2^a(\omega)$ (d) Unwrapped phase of $H_2^a(\omega)$

Source: elaborated by the author.

Examining Fig. 26, it can be seen that the two systems have similar behavior, which is to be expected because they consist of nominally the same equipment, but there are some small differences due to manufacturing.

Using the measured FRFs $H_1^a(\omega)$ and $H_2^a(\omega)$ shown in Fig. 26, the IRFs $\ddot{h}_1(t)$ and $\ddot{h}_2(t)$ are calculated using the inverse Fourier transform. Both functions are shown in Fig. 27.

Figure 27 – IRFs $\ddot{h}_1(t)$ and $\ddot{h}_2(t)$ of the virtual pipe systems 1 and 2 respectively.

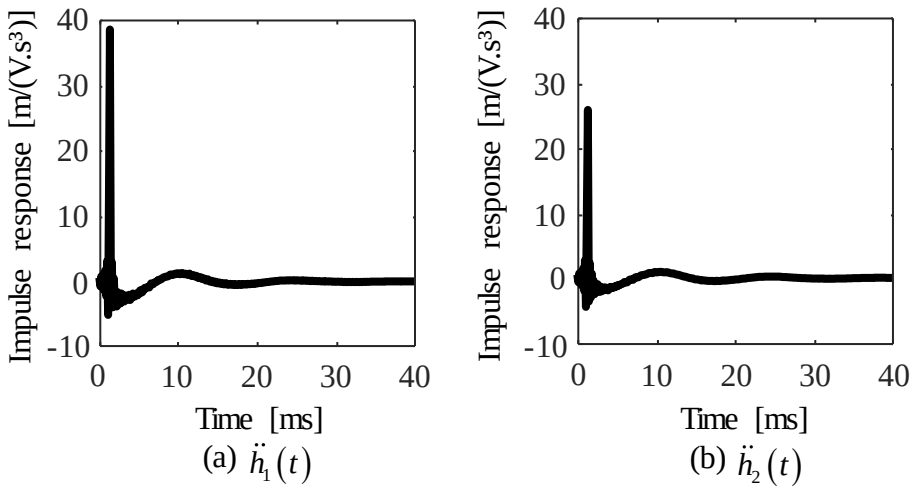

Source: elaborated by the author.

Examining Fig. 27, it can be seen that, as with the FRFs, the IRFs of the two virtual pipe systems have similar behavior, which is to be expected, but there are some small differences.

3.3.2 Compensator design for the virtual pipe systems

The aim of the compensators is to compensate for the dynamics of the power amplifiers and the shakers when they are connected in series. However, each shaker together with the power amplifier has a time delay associated with it because of the finite time it takes for a signal to pass through the compensator. This added time delay is to ensure that the compensator has a time delay rather than a time advance and ensures that the compensated system is causal. To design the compensator, the FRFs $H_s^a(\omega)$ are first inverted to give the compensators $\bar{H}_s^a(\omega)$, i.e.,

$$\bar{H}_s^a(\omega) = 1/H_s^a(\omega). \tag{21}$$

Figure 28 – IRFs $\bar{h}_1^a(t)$ and $\bar{h}_2^a(t)$ of the compensators for the virtual pipe systems 1 and 2 respectively. The plots of $\bar{h}_1^a(t)$ and $\bar{h}_2^a(t)$ are given by the lines ▬, and the zones given by the lines ▪▪ show the segments of $\bar{h}_1^a(t)$ and $\bar{h}_2^a(t)$ that contain the compensation for the dynamics of the virtual pipe systems 1 and 2 respectively.

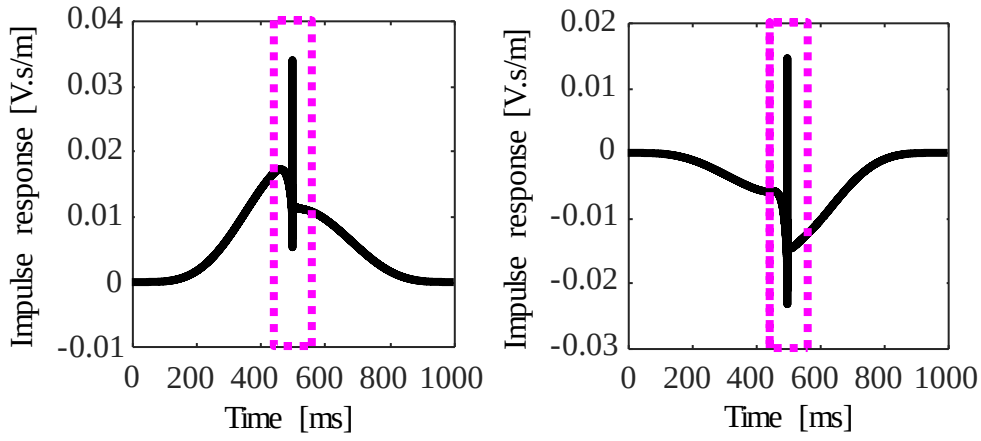

(a) $\bar{h}_1^a(t)$ (b) $\bar{h}_2^a(t)$

Source: elaborated by the author.

The IRFs $\bar{h}_s^a(t)$ of the compensators, in which $0 \le t \le T$, are then calculated through the inverse Fourier transform. A time delay α is then added resulting in the modified IRFs given by

$$\bar{h}_s^a(t) = \bar{h}_s^a(t+\alpha) \tag{22}$$

where $\alpha = T/2$. In the experiments reported here, T was set equal to 1.0×10^3 ms with a delay α of 500 ms. The IRFs $\bar{h}_s^a(t)$ of the compensators for each system are shown in Fig. 28. Note that the zones of $\bar{h}_s^a(t)$, given by the lines ▪▪ in Fig. 28, show the segments that were selected to design the modified compensators for the virtual pipe systems 1 and 2. The intervals were chosen based on the minimal interval of $\bar{h}_s^a(t)$ that can be truncated, without losing information regarding the compensation for the dynamics of the systems.

3.3.3 *Modified compensator design for a single degree of freedom system*

Although the compensators described in the previous subsection could be used in the practical system, they are described in the interval from 0 up to 1.0×10^{3} ms. However, this is inefficient as they could be represented accurately in a much minor interval. In the work conducted here, the interval was decreased by removing the segments of $\bar{h}_s^a(t)$ that are outside the zones given by the lines ▪▪ in Fig. 28, and keeping the segments of $\bar{h}_s^a(t)$ which are inside the zones and contain the information required to compensate for the dynamics of the virtual pipe systems 1 and 2. Such zones contain the segments of $\bar{h}_s^a(t)$ that are described between approximately 440 ms and 560 ms in Fig. 28, decreasing the time interval from 1.0×10^{3} ms to 120 ms. Then, the IRFs $\bar{h}_s^a(t)$ were multiplied by a Hanning window to ensure that the beginning and end of these functions are tapered smoothly to zero. This is done to minimize the Gibbs phenomenon resulted from the abrupt truncation of $\bar{h}_s^a(t)$. These operations resulted in the modified IRFs $\hat{h}_s^a(t)$, described in the interval from 0 up to 120 ms as shown in Fig. 29.

Figure 29 – Modified IRFs $\hat{h}_1^a(t)$ and $\hat{h}_2^a(t)$ of the compensators for the virtual pipe systems 1 and 2 respectively. The plots of $\hat{h}_1^a(t)$ and $\hat{h}_2^a(t)$ are given by the lines ▬, and the zones given by the lines ▪▪ show the segments of $\bar{h}_1^a(t)$ and $\bar{h}_2^a(t)$ that were extracted from Fig. 28.

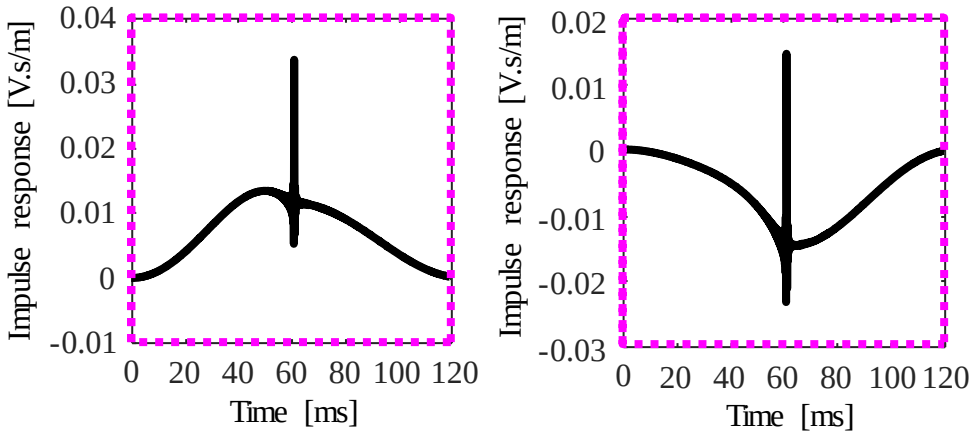

(a) $\hat{h}_1^a(t)$ (b) $\hat{h}_2^a(t)$

Source: elaborated by the author.

To verify if the IRFs $\hat{h}_s^a(t)$ are able to compensate for the dynamics of the systems depicted in Fig. 25, the modified IRFs of the two compensated systems of the virtual pipe test rig $\ddot{h}_{\text{com}_s}(t)$ are calculated through the convolution of $\hat{h}_s^a(t)$ and $\ddot{h}_s(t)$ within the computer, i.e., $\ddot{h}_{\text{com}_s}(t) = \hat{h}_s^a(t) \otimes \ddot{h}_s(t)$. The result should be a delayed *sinc* function (note that if the bandwidth was infinite then the result would be a delayed delta function). The results are shown in Fig. 30 (line ▪▪).

Figure 30 – Normalized IRFs $\ddot{h}_1(t)$ and $\ddot{h}_2(t)$ of the two virtual pipe systems and IRFs $\ddot{h}_{\text{com}_1}(t)$ and $\ddot{h}_{\text{com}_2}(t)$ of the two compensated virtual pipe systems. $\ddot{h}_1(t)$ and $\ddot{h}_2(t)$ are represented by the line ▬, and $\ddot{h}_{\text{com}_1}(t)$ and $\ddot{h}_{\text{com}_2}(t)$ are represented by the line ▪▪.

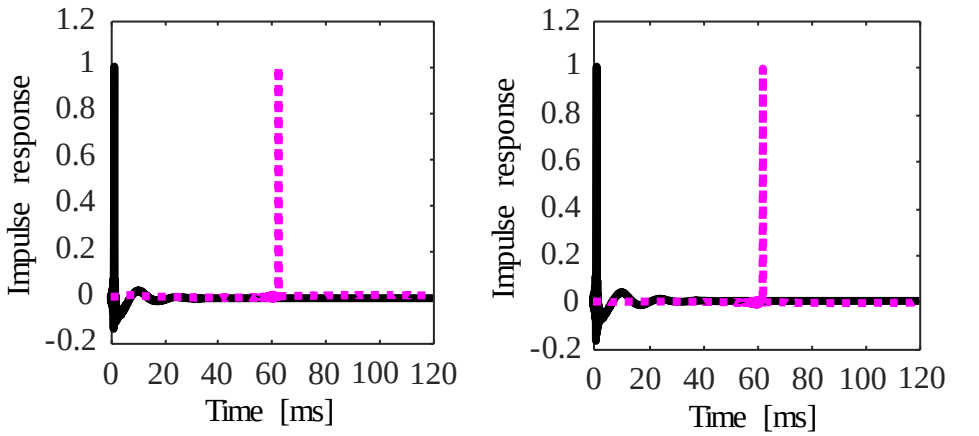

(a) Normalized $\ddot{h}_1(t)$ and $\ddot{h}_{\text{com}_1}(t)$ (b) Normalized $\ddot{h}_2(t)$ and $\ddot{h}_{\text{com}_2}(t)$

Source: elaborated by the author.

Also shown in each graph of Fig. 30 are the IRFs $\ddot{h}_1(t)$ and $\ddot{h}_2(t)$ of the virtual pipe systems 1 and 2, normalized by the maximum value of $\ddot{h}_1(t)$ and $\ddot{h}_2(t)$ respectively (line ▬). It can be seen that $\ddot{h}_{\text{com}_s}(t)$ are apparently delayed unitary impulses, which means that the compensators are functioning as expected. Note that $\ddot{h}_{\text{com}_s}(t)$ are not pure delay delta functions because of the finite bandwidth, which is between 0 and 4,096 Hz, since a H_1 spectral estimator was used together with a sampling frequency of 8,192 Hz to calculate the FRFs $H_1^a(\omega)$ and $H_2^a(\omega)$ of the virtual pipe systems 1 and 2.

Figure 31 – Schematic diagram of the two compensated systems of the virtual pipe test rig.

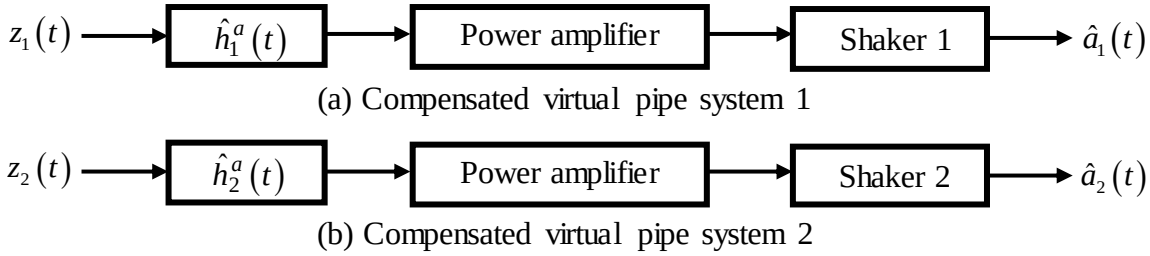

Source: elaborated by the author.

Given the encouraging results shown in Fig. 30, where the combination of the IRFs of the compensators and the IRFs of the power amplifiers and the shakers was carried out entirely in the computer, it was decided to verify whether the compensators would work in practice. To do this, white noise signals $z_1(t)$ and $z_2(t)$ were filtered by the compensators, and then the filtered signals were supplied to the power amplifiers and shakers resulting the accelerations $\hat{a}_1(t)$ and $\hat{a}_2(t)$, as shown in Fig. 31. The input signals and the output signals were again measured in a time interval of 60 s with the sampling frequency of 8,192 Hz. The FRFs of the systems shown in Fig. 31 were also estimated by a H_1 spectral estimator with a sampling frequency of 8,192 Hz and 8,192 points to calculate the FFT, resulting a frequency resolution of approximately 1 Hz. The CPSD between the signals and the PSD of the input signals were calculated using the Welch's modified periodogram method, in which the signals were divided into 64 segments. Each segment was also multiplied by a Hanning window, and 50% overlap was adopted between the segments (OPPENHEIM; SCHAFER, 2011). Such functions are shown in Fig. 32 (line ▬) in terms of magnitude and unwrapped phase. Also plotted in Fig. 32 are the FRFs corresponding to the Fourier transform of the IRFs $\ddot{h}_{\mathrm{com_s}}(t)$, shown in Fig. 30 (line ▪▪).

Using the FRFs depicted in Fig. 32, the IRFs $\ddot{h}_{\mathrm{com_s}}(t)$, shown in Fig. 33, were estimated by the results of the laboratory experiment by calculating the inverse Fourier transform (line ▬), and compared with $\ddot{h}_{\mathrm{com_s}}(t)$ given by the convolution (line ▪▪).

Figure 32 – FRFs $H^{a}_{\text{com}_1}(\omega)$ and $H^{a}_{\text{com}_2}(\omega)$. $H^{a}_{\text{com}_1}(\omega)$ and $H^{a}_{\text{com}_2}(\omega)$ estimated by the laboratory experiment are represented by the line ▬, and $H^{a}_{\text{com}_1}(\omega)$ and $H^{a}_{\text{com}_2}(\omega)$ given by the convolution are represented by the line ▪▪.

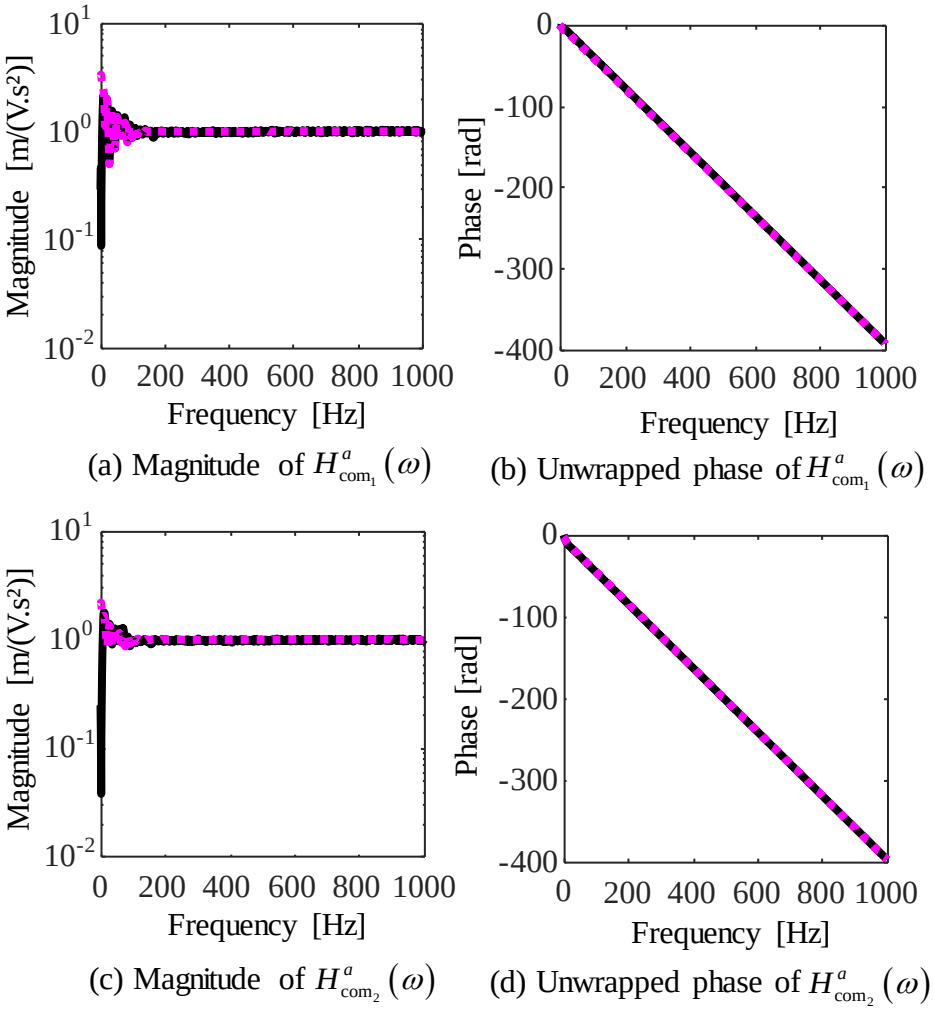

(a) Magnitude of $H^{a}_{\text{com}_1}(\omega)$ (b) Unwrapped phase of $H^{a}_{\text{com}_1}(\omega)$

(c) Magnitude of $H^{a}_{\text{com}_2}(\omega)$ (d) Unwrapped phase of $H^{a}_{\text{com}_2}(\omega)$

Source: elaborated by the author.

Figure 33 – IRFs $\ddot{h}_{com_1}(t)$ and $\ddot{h}_{com_2}(t)$ of the two compensated systems of the virtual pipe test rig. $\ddot{h}_{com_1}(t)$ and $\ddot{h}_{com_2}(t)$ estimated by the laboratory experiment are represented by the line ▬, and $\ddot{h}_{com_1}(t)$ and $\ddot{h}_{com_2}(t)$ given by the convolution are represented by the line ▪▪.

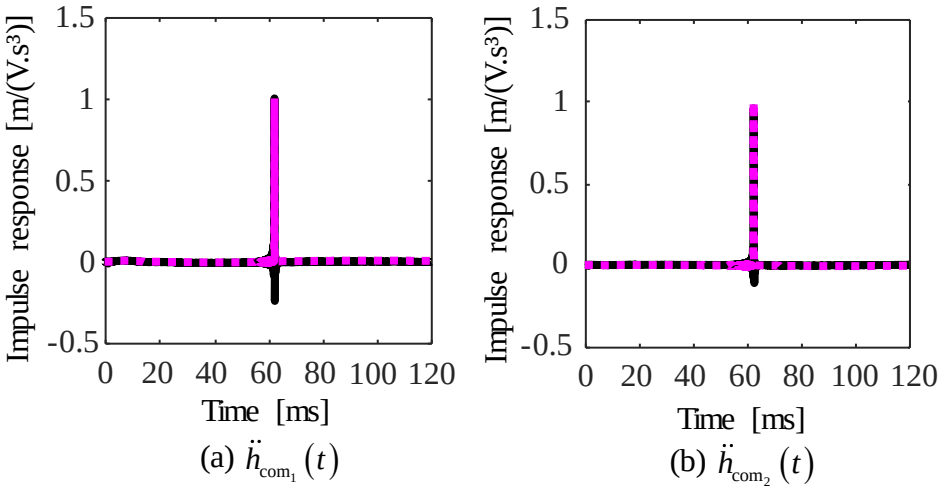

(a) $\ddot{h}_{com_1}(t)$ (b) $\ddot{h}_{com_2}(t)$

Source: elaborated by the author.

Note in Fig. 32 that the magnitude and phase of the FRFs for both systems are given approximately by a constant and a straight line with a constant slope respectively. This suggests that such systems provide pure delay signals as can be verified in Fig. 33, where the IRFs of both systems are approximately a delayed unitary impulse. Some differences between the two FRFs are apparent at low frequency, probably due to the poor frequency response of the accelerometers with the associated instrumentation and the shaker dynamics. Furthermore, observing Fig. 33, it can be seen that $\ddot{h}_{com_s}(t)$ are not pure delay delta functions because of the finite bandwidth, resulting in a delayed *sinc* function.

3.4 SUMMARY

This chapter illustrates the design approach of a compensator for a SDOF system, whose FRF and IRF are given by simple functions. The design of the compensator is based on the inverted version of the FRF of the system, which is a function that represents the dynamics of the system in frequency domain. Then, the IRF of the compensator is calculated by the inverse Fourier transform of the compensator. A time delay is applied on the response of the compensator to assure that the response of the compensated system, which is given by the combination of the compensator and the system, is causal, i.e. the time delay is applied to ensure that the response of the compensated system has a time delay rather than a time advance.

Since the compensation for the dynamics of the system can be represented by a segment of the IRF of the compensator, such a segment is truncated from the function and multiplied by a Hanning window. This operation resulted in a new function called modified compensator.

The performance of the modified compensator for the SDOF system was checked in the time domain by convolving the IRF of the system with the IRF of the modified compensator, resulting in a delayed delta function. This is a satisfactory result since it suggests that the compensated SDOF system is pure delay, which means that the influence of the dynamics of the SDOF system is compensated in the response of the system. This characteristic was also checked in the frequency domain by calculating the Fourier transform of the IRF of the compensated SDOF system, which resulted in an FRF whose magnitude is approximately given by a unitary constant and the phase is given by a straight line with constant slope. Although the compensation does not exist for the entire bandwidth, and that there are Gibbs phenomenon in the FRF caused by truncation of the IRF of the compensator, the results are considered satisfactory.

The same approach was used to compensate for the dynamics of the virtual pipe systems. The performance of the modified compensators was also checked by convolving the IRFs of the systems with the IRFs of the modified compensators, within the computer, which also resulted in pure delay systems.

Given the encouraging results, the performance of the modified compensators was also checked by carrying out a laboratory experiment, in which white noise signals were filtered by the modified compensators before supplying them to the virtual pipe systems. The results of the experiment showed that the IRFs of the compensated virtual pipe systems are approximately given by *sinc* functions, because of the finite bandwidth, and the magnitude and phase of the FRFs are approximately given by a unitary constant and a straight line with constant slope respectively.

3.5 CONCLUSIONS

The dynamics of the power amplifiers and the shakers can affect the vibrations provided by them. To avoid the influence of the dynamics of such devices, the compensation of these dynamics is necessary. One way to do this is to design filters to compensate for the dynamics of the power amplifiers and the shakers before supplying the signal to them. These filters are called compensators, and a simple approach to design them was introduced in this chapter. The results in both domains suggest that the compensated SDOF system and the compensated virtual pipe systems are approximately pure delay, in which the dynamics of these systems are compensated within a finite bandwidth. Since the leak noise is contained within a bandwidth where the compensators are able to compensate for the dynamics of the virtual pipe systems, the results are considered to be satisfactory. The next chapter introduces the leak noise simulation using the virtual pipe test rig, where the model of a buried leaking pipe, introduced in Chapter 2, is used to synthesize leak noise within the computer. The virtual pipe systems, together with the modified compensators implemented as filters within the computer, are used to generate vibrations representative of measured leak noise.

4 LEAK NOISE SIMULATION USING THE VIRTUAL TEST RIG AND THE COMPENSATORS

4.1 INTRODUCTION

This chapter describes the procedure to simulate a leak in a buried pipe in the laboratory, by using the virtual pipe test rig to generate vibrations similar to those generated by a leak in a buried pipe. The virtual pipe systems described in Chapter 3, which are the two systems that compose the virtual pipe test rig, are supplied with synthesized leak noise, which is the signal obtained by filtering white noise with the model of a buried pipe described in Chapter 2. Accelerometers are used to measure the vibrations provided by both shakers, and the CPSD, coherence and CCC are calculated using such signals. This is done with and without the modified compensators in the system for comparison. To verify if the virtual pipe test rig is able to simulate real conditions using measured data from real leaks, another laboratory experiment was carried out using the measurements of a real leak from two different test sites. One test site is from SABESP, in Brazil, and the other one is from National Research Council (NRC), in Canada. The data from both test sites were acceleration time histories. The vibrations provided by both shakers were also measured using accelerometers. The performance of the systems was assessed as in the previous tests.

4.2 LEAK NOISE SIMULATION BY SUPPLYING THE VIRTUAL PIPE TEST RIG WITH SYNTHESIZED LEAK NOISE

To check the performance of the modified compensators in leak noise simulation, two experiments were carried out: leak noise simulation by supplying the virtual pipe systems 1 and 2 with the synthesized leak noise $\bar{y}_1(t)$ and $\bar{y}_2(t)$, as shown in Fig. 34, and leak noise simulation by supplying the compensated virtual pipe systems 1 and 2 with the synthesized leak noise $\bar{y}_1(t)$ and $\bar{y}_2(t)$, as shown in Fig. 35.

Figure 34 – Schematic diagram of leak noise simulation using the virtual pipe systems 1 and 2, supplied by the synthesized leak noise $\bar{y}_1(t)$ and $\bar{y}_2(t)$ respectively, to generate the accelerations $\bar{a}_1(t)$ and $\bar{a}_2(t)$.

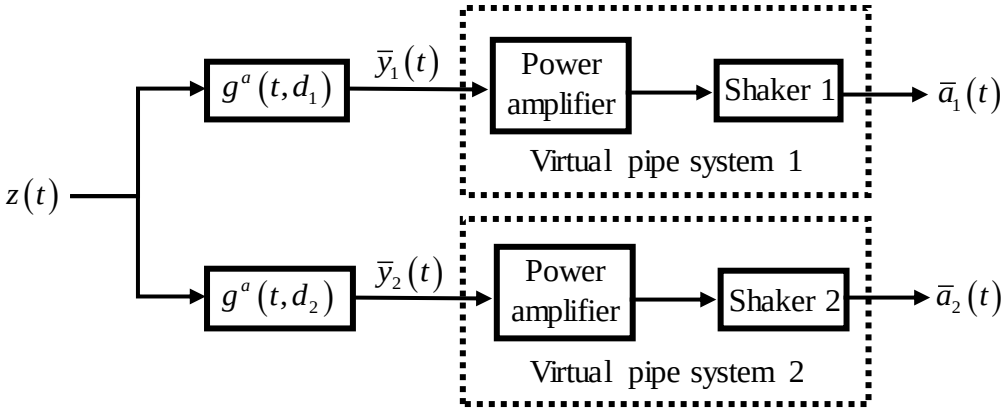

Source: elaborated by the author.

In both experiments, white noise $z(t)$ was filtered within the computer by the IRFs $g^a(t,d_1)$ and $g^a(t,d_2)$ of the buried pipe, resulting in the synthesized leak noise $\bar{y}_1(t)$ and $\bar{y}_2(t)$. Such functions were calculated considering the parameters for the MDPE pipe and the soil shown in Tab. 2.1, with $d_1 = 30$ m and $d_2 = 50$ m.

Figure 35 – Schematic diagram of leak noise simulation using the compensated virtual pipe systems 1 and 2, supplied by the synthesized leak noise $\bar{y}_1(t)$ and $\bar{y}_2(t)$ respectively, to generate the accelerations $\hat{a}_1(t)$ and $\hat{a}_2(t)$.

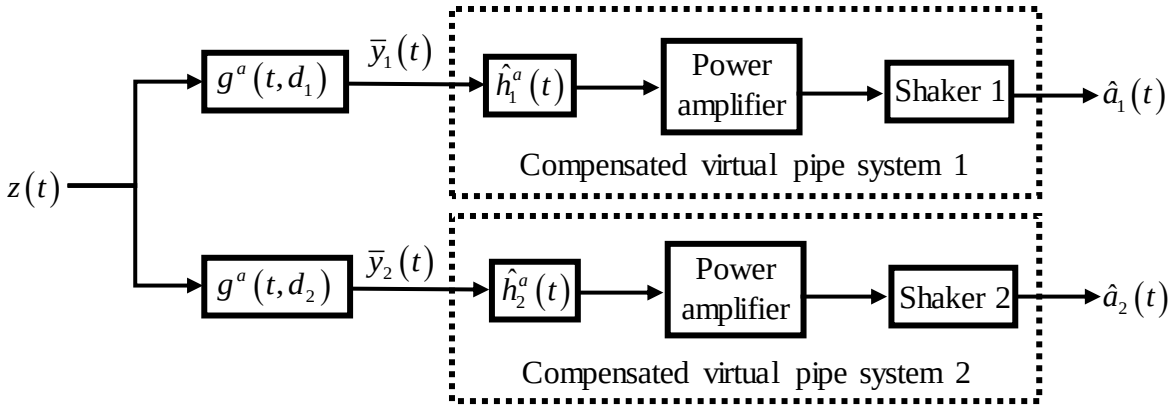

Source: elaborated by the author.

In the first experiment, shown in Fig. 34, $\bar{y}_1(t)$ and $\bar{y}_2(t)$ were directly supplied to the power amplifiers and the shakers 1 and 2 of the virtual pipe systems 1 and 2, resulting in the accelerations $\bar{a}_1(t)$ and $\bar{a}_2(t)$ respectively. In the second experiment, shown in Fig. 35, $\bar{y}_1(t)$ and $\bar{y}_2(t)$ were filtered by the IRFs $\hat{h}_1^a(t)$ and $\hat{h}_2^a(t)$ of the modified compensators. The filtered signals were supplied to the power amplifiers and the shakers 1 and 2 of the virtual pipe systems 1 and 2, resulting in the accelerations $\hat{a}_1(t)$ and $\hat{a}_2(t)$ respectively. The CPSDs $S_{\bar{a}_1\bar{a}_2}(\omega)$ and $S_{\hat{a}_1\hat{a}_2}(\omega)$ were both calculated using the Welch's modified periodogram method of spectral estimation (OPPENHEIM; SCHAFER, 2011). Each signal was divided into 8 segments. Each segment was multiplied by a Hann window, and 50% overlap was adopted between the segments. The CCFs of the averaged signals were calculated, and the CPSDs were determined by calculating the Fourier transform of the CCFs. A sampling frequency of 8,192 Hz was used together with an 8,192-point CPSD, resulting in a frequency resolution of approximately 1 Hz. Both CPSDs are shown in Figs. 36-37 (line ▬). Also shown in both figures is the CPSD $S_{\bar{y}_1\bar{y}_2}(\omega)$ (line ▬), given by Eq. (12), which is the combination of acoustic correlation and the buried leaking pipe model in frequency domain.

Figure 36 – CPSDs $S_{\bar{a}_1\bar{a}_2}(\omega)$ and $S_{\bar{y}_1\bar{y}_2}(\omega)$ considering the parameters of the MDPE pipe and soil from Tab. 2.1 with $d_1 = 30$ m and $d_2 = 50$ m. $S_{\bar{a}_1\bar{a}_2}(\omega)$ is given by the line ▬ and $S_{\bar{y}_1\bar{y}_2}(\omega)$ obtained through Eq. (12) is given by the line ▬.

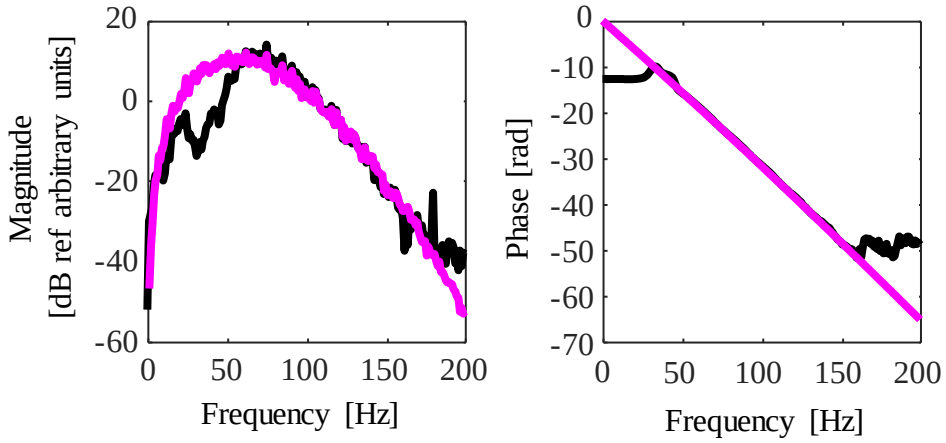

(a) Normalised magnitude (b) Unwrapped phase

Source: elaborated by the author.

Figure 37 – CPSDs $S_{\hat{a}_1\hat{a}_2}(\omega)$ and $S_{\bar{y}_1\bar{y}_2}(\omega)$ considering the parameters of the MDPE pipe and soil from Tab. 2.1 with $d_1 = 30$ m and $d_2 = 50$ m. $S_{\hat{a}_1\hat{a}_2}(\omega)$ is given by the line ▬ and $S_{\bar{y}_1\bar{y}_2}(\omega)$ obtained through Eq. (12) is given by the line ▬.

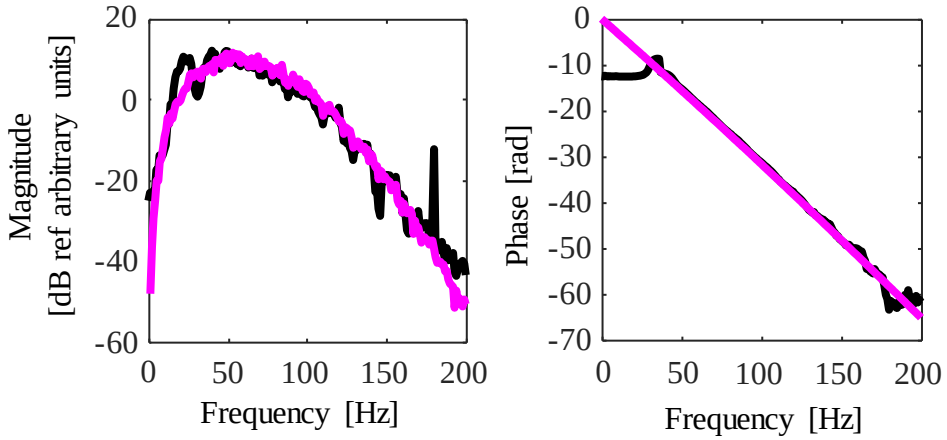

(a) Normalised magnitude (b) Unwrapped phase

Source: elaborated by the author.

Note that the agreement between the magnitudes of $S_{\hat{a}_1\hat{a}_2}(\omega)$ and $S_{\bar{y}_1\bar{y}_2}(\omega)$, shown in Fig. 37(a), is greater than the agreement between the magnitudes of $S_{\bar{a}_1\bar{a}_2}(\omega)$ and $S_{\bar{y}_1\bar{y}_2}(\omega)$, shown in Fig. 36(a), within the bandwidth between approximately 10 Hz and 60 Hz. This suggests that the dynamics of the power amplifiers and the shakers behaves as a pass-band filter, decreasing the agreement between the correlation of the vibrations provided by the shakers and the correlation of the synthesized leak noise within this bandwidth. When the synthesized leak noise is filtered by the IRFs $\hat{h}_1^a(t)$ and $\hat{h}_2^a(t)$ of the modified compensators before being supplied to the virtual pipe systems, the dynamics of such devices are compensated increasing the agreement between the correlation of the vibrations provided by the shakers and the correlation of the synthesized leak noise within this bandwidth. Note that the slope of the phase of $S_{\hat{a}_1\hat{a}_2}(\omega)$ (line ▬) is approximately equal to the slope of the phase of $S_{\bar{y}_1\bar{y}_2}(\omega)$ (line ▬) in Fig. 37(b), since both compensators applies the same time delay on $\bar{y}_1(t)$ and $\bar{y}_2(t)$ when they are filtered.

Figure 38 – Coherences $\gamma_{\bar{a}_1\bar{a}_2}(\omega)$, $\gamma_{\hat{a}_1\hat{a}_2}(\omega)$ and $\gamma_{\bar{y}_1\bar{y}_2}(\omega)$ considering the parameters of the MDPE pipe and soil from Tab. 2.1 with $d_1 = 30$ m and $d_2 = 50$ m. $\gamma_{\bar{a}_1\bar{a}_2}(\omega)$ and $\gamma_{\hat{a}_1\hat{a}_2}(\omega)$ are given by the line ▬ and $\gamma_{\bar{y}_1\bar{y}_2}(\omega)$ obtained through Eq. (16) is given by the line ▬.

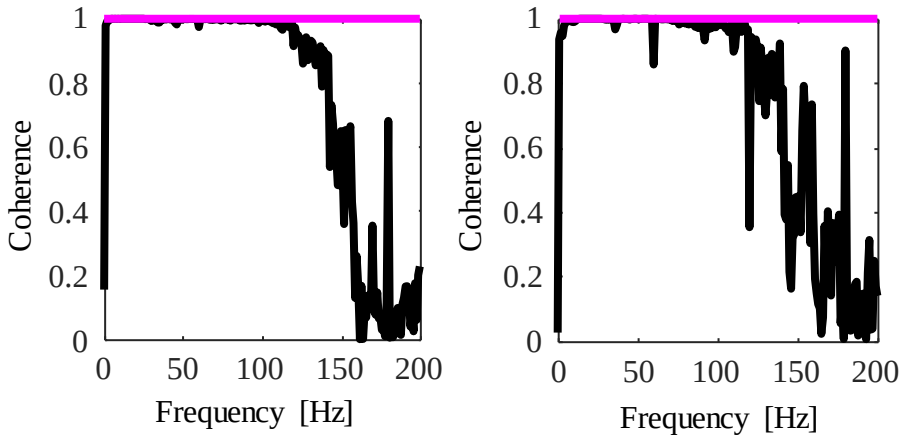

(a) Coherences $\gamma_{\bar{a}_1\bar{a}_2}(\omega)$ and $\gamma_{\bar{y}_1\bar{y}_2}(\omega)$

(b) Coherences $\gamma_{\hat{a}_1\hat{a}_2}(\omega)$ and $\gamma_{\bar{y}_1\bar{y}_2}(\omega)$

Source: elaborated by the author.

The coherences $\gamma_{\bar{a}_1\bar{a}_2}(\omega)$ and $\gamma_{\hat{a}_1\hat{a}_2}(\omega)$ were also calculated using the Welch's modified periodogram method of spectral estimation (OPPENHEIM; SCHAFER, 2011), with the parameters used to calculate the CPSDs $S_{\bar{a}_1\bar{a}_2}(\omega)$ and $S_{\hat{a}_1\hat{a}_2}(\omega)$. Both functions are shown in Fig. 38 (line ▬) in which the coherence $\gamma_{\bar{y}_1\bar{y}_2}(\omega)$ (line ▬), given by Eq. (16), is also shown. Note that the synthesized leak noise $\bar{y}_1(t)$ and $\bar{y}_2(t)$ are correlated over the entire bandwidth, since the coherence $\gamma_{\bar{y}_1\bar{y}_2}(\omega)$ is given by a unitary constant. However, the accelerations $\bar{a}_1(t)$ and $\bar{a}_2(t)$ are approximately correlated between 10 Hz and 150 Hz, since the coherence $\gamma_{\bar{a}_1\bar{a}_2}(\omega)$ is approximately a unitary constant within this bandwidth in Fig. 38(a). The same correlation can be checked for the accelerations $\hat{a}_1(t)$ and $\hat{a}_2(t)$ by observing $\gamma_{\hat{a}_1\hat{a}_2}(\omega)$ in Fig. 38(b). Below 10 Hz, the low correlation probably occurs due to the poor frequency response of the accelerometers with the associated instrumentation; and above 150 Hz, the low correlation probably occurs because the synthesized leak noise has a very small magnitude above this frequency that the computer is not able to reproduce as a voltage signal. So, if white noise is filtered by the IRFs $g^a(t, d_1)$ and $g^a(t, d_2)$, considering the parameters of the pipe and soil

from Tab. 2.1 with $d_1 = 30$ m and $d_2 = 50$ m, the voltage signal provided by the computer above 150 Hz is only uncorrelated noise.

The CCCs $\rho_{\bar{a}_1\bar{a}_2}(\tau)$ and $\rho_{\hat{a}_1\hat{a}_2}(\tau)$ are shown in Fig. 39 (line ▬), in which the CCC $\rho_{\bar{y}_1\bar{y}_2}(\tau)$ (line ▪▪), given by Eq. (15), represents the combination of acoustic correlation and the buried leaking pipe model in time domain. By comparing Fig. 39(a) with Fig. 39(b), the agreement of $\rho_{\hat{a}_1\hat{a}_2}(\tau)$ and $\rho_{\bar{y}_1\bar{y}_2}(\tau)$ is greater than the agreement of $\rho_{\bar{a}_1\bar{a}_2}(\tau)$ and $\rho_{\bar{y}_1\bar{y}_2}(\tau)$. This is an expected result since the agreement of $S_{\hat{a}_1\hat{a}_2}(\omega)$ and $S_{\bar{y}_1\bar{y}_2}(\omega)$ is greater than the agreement of $S_{\bar{a}_1\bar{a}_2}(\omega)$ and $S_{\bar{y}_1\bar{y}_2}(\omega)$ between approximately 10 Hz and 60 Hz, i.e. the greater the agreement between two functions in one domain, the greater the agreement between them in the transformed domain.

Figure 39 – CCCs $\rho_{\bar{a}_1\bar{a}_2}(\tau)$, $\rho_{\hat{a}_1\hat{a}_2}(\tau)$ and $\rho_{\bar{y}_1\bar{y}_2}(\tau)$ considering the parameters of the MDPE pipe and soil from Tab. 2.1 with $d_1 = 30$ m and $d_2 = 50$ m. $\rho_{\bar{a}_1\bar{a}_2}(\tau)$ and $\rho_{\hat{a}_1\hat{a}_2}(\tau)$ are given by the line ▬ and $\rho_{\bar{y}_1\bar{y}_2}(\tau)$ obtained through Eq. (15) is given by the line ▪▪.

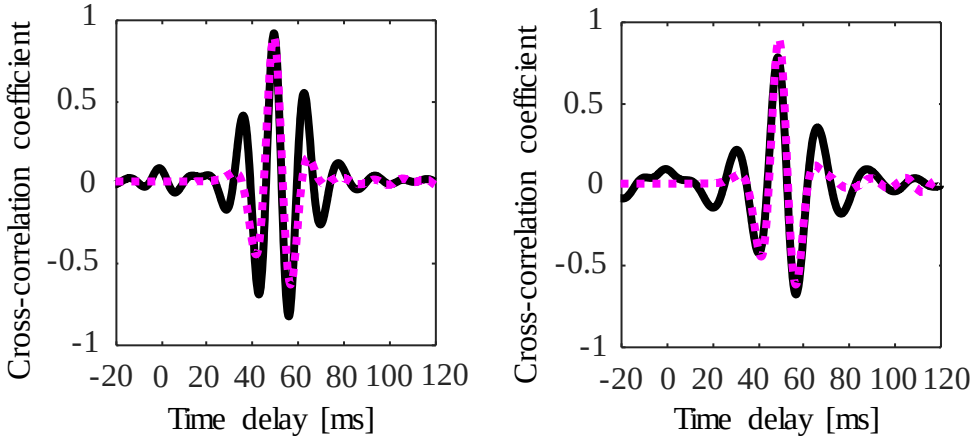

(a) CCCs $\rho_{\bar{a}_1\bar{a}_2}(\tau)$ and $\rho_{\bar{y}_1\bar{y}_2}(\tau)$

(b) CCCs $\rho_{\hat{a}_1\hat{a}_2}(\tau)$ and $\rho_{\bar{y}_1\bar{y}_2}(\tau)$

Source: elaborated by the author.

4.3 LEAK NOISE SIMULATION BY SUPPLYING THE VIRTUAL PIPE TEST RIG WITH MEASURED DATA OF REAL LEAKS FROM TEST SITES

To verify that the virtual pipe test rig is able to replicate the behavior of a real buried leaking pipes and to check the performance of the compensators, two experiments were carried out. They were leak noise simulation by supplying the virtual pipe systems 1 and 2 with measured data of a real leak, as shown in Fig. 40, and leak noise simulation by supplying the compensated virtual pipe systems 1 and 2 with measured data of a real leak, as shown in Fig. 41. To simulate leaks in different practical situations, such as different soil properties, leak strengths, pipe properties and pipe geometries, the experiments were performed using measured data from two different test sites: one is from SABESP, in Brazil, and the another is from NRC, in Canada. The data from both test sites are accelerations that were measured by two sensors, called sensor 1 and sensor 2, that were positioned either side of a leak in a buried pipe as shown in Fig. 3.

The accelerations from the SABESP test site were measured using two PCB 352B10 piezoelectric accelerometers, whose sensitivity is about 10 mV/g, and an LMS SCADAS data acquisition system. The signals were measured and recorded with a sampling frequency of 8,192 Hz and a time length of 120 s. The accelerations from NRC test site were measured using two piezoelectric accelerometers and a data acquisition system, whose specifications are given in Hunaidi and Chu (1999), and the signals were recorded with a sampling frequency of 500 Hz and a time length of 60 s.

In the first experiment, shown in Fig. 40, the measured data were directly supplied to the power amplifiers and the shakers 1 and 2 of the virtual pipe systems 1 and 2, resulting in the accelerations $\bar{a}_1(t)$ and $\bar{a}_2(t)$ respectively. In the second experiment, shown in Fig. 41, the measured data were filtered by the IRFs $\hat{h}_1^a(t)$ and $\hat{h}_2^a(t)$ of the modified compensators. The filtered signals were supplied to the power amplifiers and the shakers 1 and 2 of the virtual pipe systems 1 and 2, resulting in the accelerations $\hat{a}_1(t)$ and $\hat{a}_2(t)$ respectively. The following subsections present the results of each experiment when the systems are supplied with the measured data from the SABESP test site and when they are supplied with the measured data from the NRC test site.

Figure 40 – Schematic diagram of leak noise simulation using the virtual pipe systems 1 and 2, supplied by the accelerations measured at SABESP and NRC test sites, to generate the accelerations $\bar{a}_1(t)$ and $\bar{a}_2(t)$.

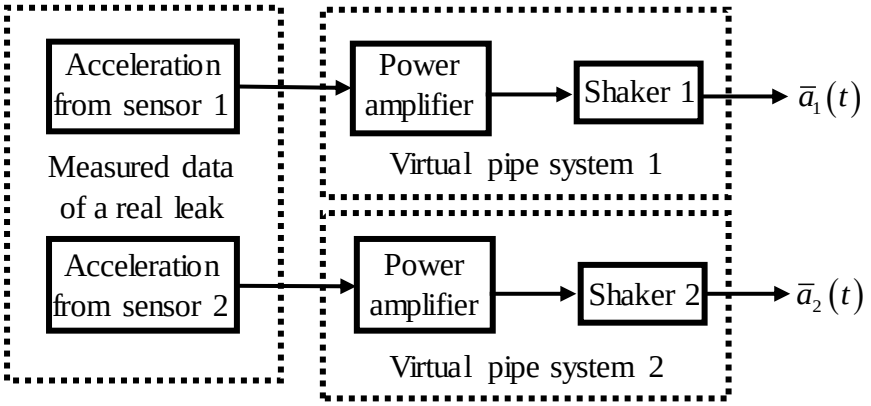

Source: elaborated by the author.

Figure 41 – Schematic diagram of leak noise simulation using the compensated virtual pipe systems 1 and 2, supplied by the accelerations measured at SABESP and NRC test sites, to generate the accelerations $\hat{a}_1(t)$ and $\hat{a}_2(t)$.

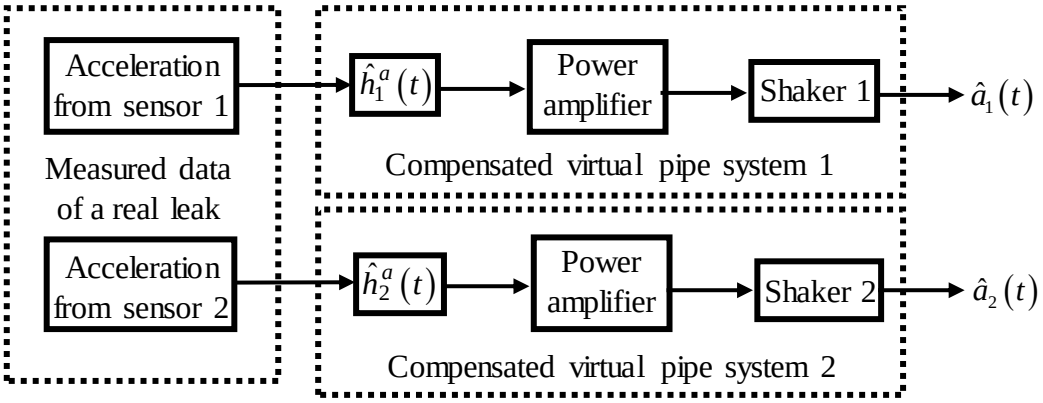

Source: elaborated by the author.

4.3.1 *Leak noise simulation by supplying the virtual pipe test rig with the measured data from the SABESP test rig*

By supplying the virtual pipe systems with the measured data from the SABESP test site, the CPSD $S_{\bar{a}_1\bar{a}_2}(\omega)$ of the accelerations $\bar{a}_1(t)$ and $\bar{a}_2(t)$ and the CPSD $S_{\hat{a}_1\hat{a}_2}(\omega)$ of the accelerations $\hat{a}_1(t)$ and $\hat{a}_2(t)$ were both calculated using the Welch's modified periodogram method of spectral estimation (OPPENHEIM; SCHAFER, 2011). Each signal was divided into 128 segments. Each segment was multiplied by a Hann window, and 50% overlap was adopted between the segments. The CCFs of the averaged signals were calculated, and the CPSDs were determined by calculating the Fourier transform of the CCFs. A sampling frequency of 8,192 Hz was used together with an 8,192-point CPSD, resulting in a frequency resolution of approximately 1 Hz. Both CPSDs are shown in Figs. 42-43 (line ▬) in terms of magnitude and unwrapped phase. Also shown in both figures is the CPSD $S_{\text{data}_1}(\omega)$ (line ▬) of the accelerations measured at the SABESP test site, which was calculated using the same method with the parameters used to calculate $S_{\bar{a}_1\bar{a}_2}(\omega)$ and $S_{\hat{a}_1\hat{a}_2}(\omega)$, when the virtual pipe systems and the compensated virtual pipe systems are supplied with this measured data.

Note in Fig. 42(a) and Fig. 43(a) that the measured data from the SABESP test rig and the accelerations provided by the shakers in the experiment agree between approximately 300 Hz and 600 Hz, since the magnitude of $S_{\bar{a}_1\bar{a}_2}(\omega)$, $S_{\hat{a}_1\hat{a}_2}(\omega)$ and $S_{\text{data}_1}(\omega)$ is higher within this bandwidth. Note in Fig. 42(b) and Fig. 43(b) that the unwrapped phase of these functions is approximately given by a straight line with a constant slope within this bandwidth, which suggests that the delay between the signals is approximately constant within this bandwidth.

Figure 42 – CPSDs $S_{\bar{a}_1\bar{a}_2}(\omega)$ and $S_{\text{data}_1}(\omega)$ by supplying the virtual pipe systems with the accelerations measured at the SABESP test site. $S_{\bar{a}_1\bar{a}_2}(\omega)$ is given by the line ▬ and $S_{\text{data}_1}(\omega)$ is given by the line ▬.

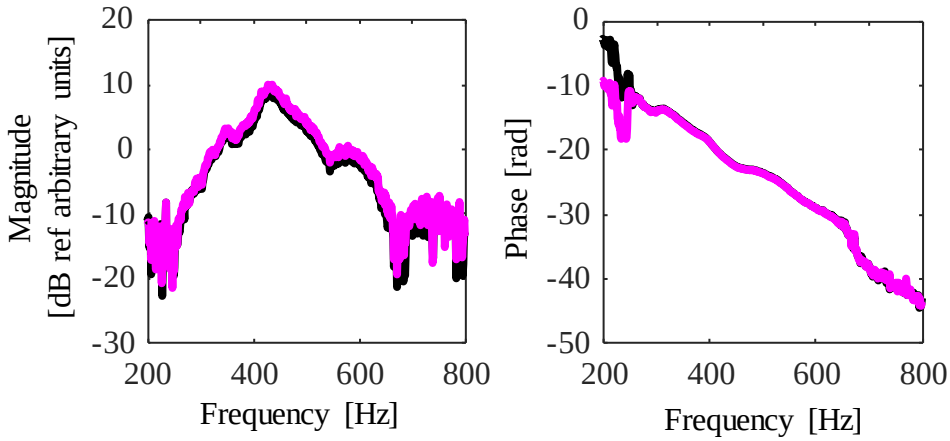

(a) Normalised magnitude (b) Unwrapped phase

Source: elaborated by the author.

Figure 43 – CPSDs $S_{\hat{a}_1\hat{a}_2}(\omega)$ and $S_{\text{data}_1}(\omega)$ by supplying the compensated virtual pipe systems with the accelerations measured at the SABESP test site. $S_{\hat{a}_1\hat{a}_2}(\omega)$ is given by the line ▬ and $S_{\text{data}_1}(\omega)$ is given by the line ▬.

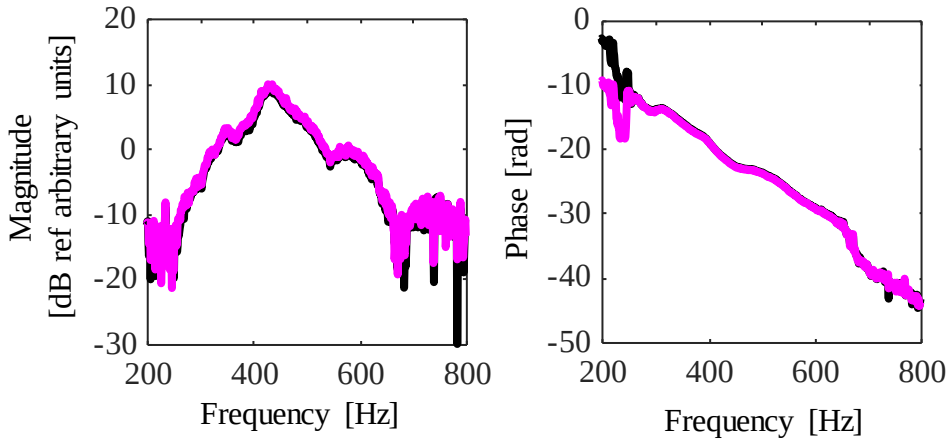

(a) Normalised magnitude (b) Unwrapped phase

Source: elaborated by the author.

The agreement of $S_{\bar{a}_1\bar{a}_2}(\omega)$ and $S_{\text{data}_1}(\omega)$, in Fig. 42, is approximately equal to the agreement of $S_{\hat{a}_1\hat{a}_2}(\omega)$ and $S_{\text{data}_1}(\omega)$, in Fig. 43. This suggests that filtering this measured data with the compensators, before supplying them to the power amplifiers and the shakers, does not provide accelerations whose correlation is better than that if the devices are supplied by this data without filtering. This is an expected result since the compensators only have an influence between approximately 10 Hz and 60 Hz, which is the bandwidth where the dynamics of the power amplifiers and the shakers have an effect.

The coherences $\gamma_{\bar{a}_1\bar{a}_2}(\omega)$ and $\gamma_{\hat{a}_1\hat{a}_2}(\omega)$, when the virtual pipe systems and the compensated virtual pipe systems are supplied with measured data from the SABESP test rig, were also calculated using the Welch's modified periodogram method of spectral estimation (OPPENHEIM; SCHAFER, 2011), with the parameters used to calculate the CPSDs $S_{\bar{a}_1\bar{a}_2}(\omega)$ and $S_{\hat{a}_1\hat{a}_2}(\omega)$. Both functions are shown in Fig. 44 (line ▬) in which the coherence $\gamma_{\text{data}_1}(\omega)$ (line ▬) of the measured data is also shown.

Figure 44 – Coherences $\gamma_{\bar{a}_1\bar{a}_2}(\omega)$, $\gamma_{\hat{a}_1\hat{a}_2}(\omega)$ and $\gamma_{\text{data}_1}(\omega)$ by supplying the virtual pipe systems and the compensated virtual pipe systems with the accelerations measured at the SABESP test site. $\gamma_{\bar{a}_1\bar{a}_2}(\omega)$ and $\gamma_{\hat{a}_1\hat{a}_2}(\omega)$ are given by the line ▬ and $\gamma_{\text{data}_1}(\omega)$ is given by the line ▬.

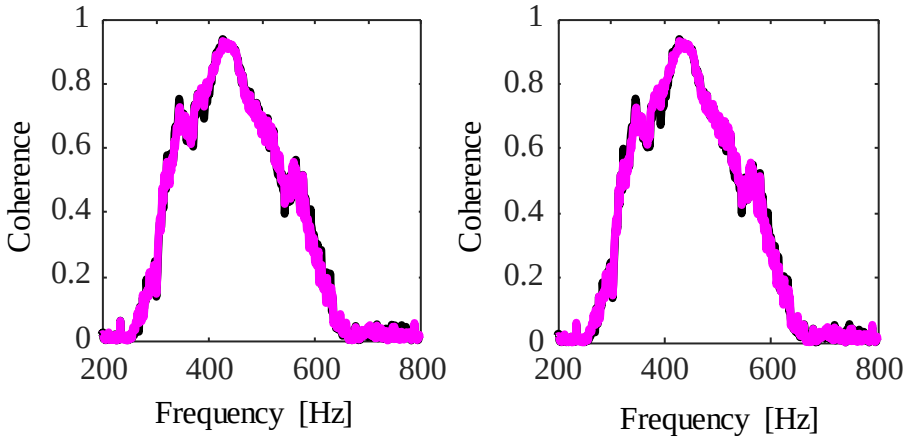

(a) Coherences $\gamma_{\bar{a}_1\bar{a}_2}(\omega)$ and $\gamma_{\text{data}_1}(\omega)$

(b) Coherences $\gamma_{\hat{a}_1\hat{a}_2}(\omega)$ and $\gamma_{\text{data}_1}(\omega)$

Source: elaborated by the author.

Note that the same information provided by $S_{\bar{a}_1\bar{a}_2}(\omega)$, $S_{\hat{a}_1\hat{a}_2}(\omega)$ and $S_{\text{data}_1}(\omega)$ is also observed in $\gamma_{\bar{a}_1\bar{a}_2}(\omega)$, $\gamma_{\hat{a}_1\hat{a}_2}(\omega)$ and $\gamma_{\text{data}_1}(\omega)$. The measured data from the SABESP test rig and the accelerations provided by the shakers are similar between approximately 300 Hz and 600 Hz, since the values of $\gamma_{\bar{a}_1\bar{a}_2}(\omega)$, $\gamma_{\hat{a}_1\hat{a}_2}(\omega)$ and $\gamma_{\text{data}_1}(\omega)$ are higher within this bandwidth; and the agreement of $\gamma_{\bar{a}_1\bar{a}_2}(\omega)$ and $\gamma_{\text{data}_1}(\omega)$ is approximately equal to the agreement of $\gamma_{\hat{a}_1\hat{a}_2}(\omega)$ and $\gamma_{\text{data}_1}(\omega)$. This suggests that supplying the devices with data filtered by the compensators does not provide accelerations whose correlation is more similar to the correlation of the measured data than without filtering it before the supply.

Figure 45 – CCCs $\rho_{\bar{a}_1\bar{a}_2}(\tau)$, $\rho_{\hat{a}_1\hat{a}_2}(\tau)$ and $\rho_{\text{data}_1}(\tau)$ by supplying the virtual pipe systems and the compensated virtual pipe systems with the accelerations measured at the SABESP test site. $\rho_{\bar{a}_1\bar{a}_2}(\tau)$ and $\rho_{\hat{a}_1\hat{a}_2}(\tau)$ are given by the line ▬ and $\rho_{\text{data}_1}(\tau)$ is given by the line ▪▪.

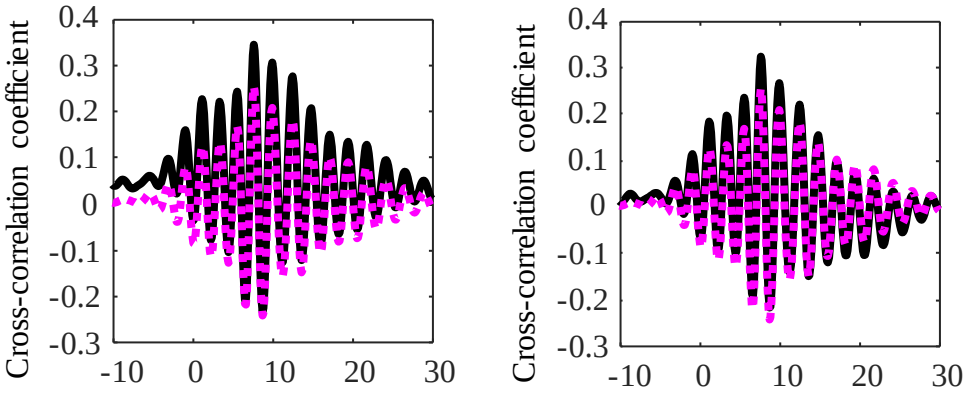

(a) CCCs $\rho_{\bar{a}_1\bar{a}_2}(\tau)$ and $\rho_{\bar{y}_1\bar{y}_2}(\tau)$

(b) CCCs $\rho_{\hat{a}_1\hat{a}_2}(\tau)$ and $\rho_{\bar{y}_1\bar{y}_2}(\tau)$

Source: elaborated by the author.

The CCCs $\rho_{\bar{a}_1\bar{a}_2}(\tau)$ and $\rho_{\hat{a}_1\hat{a}_2}(\tau)$ are shown in Fig. 45 (line ▬), in which the CCC $\rho_{\text{data}_1}(\tau)$ (line ▪▪) of the measured data is also shown. Although the agreement of $S_{\bar{a}_1\bar{a}_2}(\omega)$ and $S_{\text{data}_1}(\omega)$ is approximately equal to the agreement of $S_{\hat{a}_1\hat{a}_2}(\omega)$ and $S_{\text{data}_1}(\omega)$ within the bandwidth where the measured data are similar, the agreement of $\rho_{\hat{a}_1\hat{a}_2}(\tau)$ and $\rho_{\text{data}_1}(\tau)$ in Fig. 45(b) is slightly greater than the agreement of $\rho_{\bar{a}_1\bar{a}_2}(\tau)$ and $\rho_{\text{data}_1}(\tau)$ in Fig. 45(a). This is also an expected result since the compensators have an influence at low frequencies, where the dynamics of the power amplifiers and the shakers have an effect and the measured data has poor correlation.

4.3.2 *Leak noise simulation by supplying the virtual pipe test rig with the measured data from the NRC test rig*

By supplying the virtual pipe systems with the measured data from the NRC test site, the CPSD $S_{\bar{a}_1\bar{a}_2}(\omega)$ of the accelerations $\bar{a}_1(t)$ and $\bar{a}_2(t)$ and the CPSD $S_{\hat{a}_1\hat{a}_2}(\omega)$ of the accelerations $\hat{a}_1(t)$ and $\hat{a}_2(t)$ were both calculated using the Welch's modified periodogram method of spectral estimation (OPPENHEIM; SCHAFER, 2011). Each signal was divided into 64 segments. Each segment was multiplied by a Hann window, and 50% overlap was adopted between the segments. The CCFs of the averaged signals were calculated, and the CPSDs were determined by calculating the Fourier transform of the CCFs. A sampling frequency of 500 Hz was used together with a 500-point CPSD, resulting in a frequency resolution of approximately 1 Hz. Both CPSDs are shown in Figs. 46-47 (line ▬) in terms of magnitude and unwrapped phase. Also shown in both figures is the CPSD $S_{\text{data}_2}(\omega)$ (line ▬) of the accelerations measured at the NRC test site, which was calculated using the same method with the parameters used to calculate $S_{\bar{a}_1\bar{a}_2}(\omega)$ and $S_{\hat{a}_1\hat{a}_2}(\omega)$, when the virtual pipe systems and the compensated virtual pipe systems are supplied with this measured data.

Figure 46 – CPSDs $S_{\bar{a}_1\bar{a}_2}(\omega)$ and $S_{\text{data}_2}(\omega)$ by supplying the virtual pipe systems with the accelerations measured at the NRC test site. $S_{\bar{a}_1\bar{a}_2}(\omega)$ is given by the line ▬ and $S_{\text{data}_2}(\omega)$ is given by the line ▬.

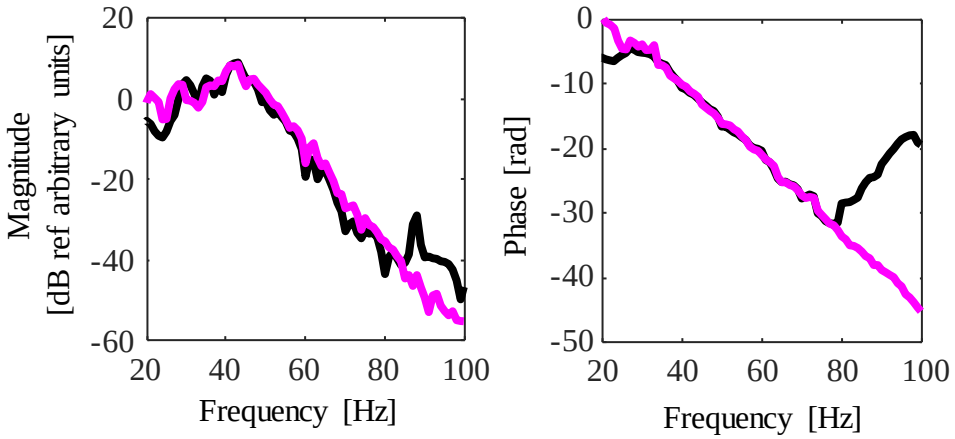

(a) Normalised magnitude (b) Unwrapped phase

Source: elaborated by the author.

Figure 47 – CPSDs $S_{\hat{a}_1\hat{a}_2}(\omega)$ and $S_{\text{data}_2}(\omega)$ by supplying the compensated virtual pipe systems with the accelerations measured at the NRC test site. $S_{\hat{a}_1\hat{a}_2}(\omega)$ is given by the line ▬ and $S_{\text{data}_2}(\omega)$ is given by the line ▬.

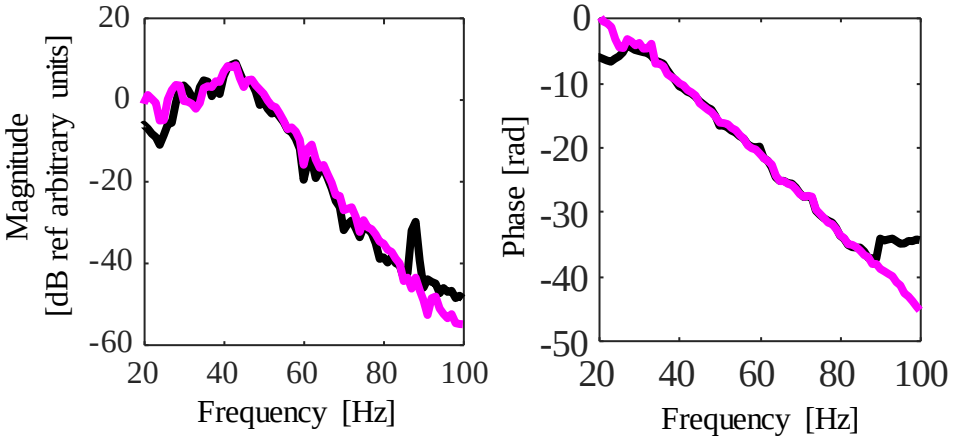

(a) Normalised magnitude (b) Unwrapped phase

Source: elaborated by the author.

Examining Fig. 46(a) and Fig. 47(a), it can be seen that the measured data from the NRC test rig and the accelerations provided by the shakers in the experiment are similar between approximately 30 Hz and 80 Hz, since the magnitude of $S_{\bar{a}_1\bar{a}_2}(\omega)$, $S_{\hat{a}_1\hat{a}_2}(\omega)$ and $S_{\text{data}_2}(\omega)$ is higher within this bandwidth. Note in Fig. 46(b) and Fig. 47(b) that the unwrapped phase of these functions is given by a straight line with a constant slope between approximately 30 Hz and 80 Hz, suggesting that the delay between the signals is approximately constant within this bandwidth.

The signals of the measured data from the NRC test rig are correlated within a bandwidth which is narrower than the bandwidth of the measured data from the SABESP test rig. This difference probably occurs due to the filtering effects of the pipe and the soil, which are a function of the soil properties, pipe properties, pipe geometries and the distances between the leak and the sensors. It is also due to the different types of sensors used to measure acceleration on the pipe network of both test rigs. Note in Fig. 46(a) and in Fig. 47(a) that above 80 Hz, there are some peaks in the magnitude of $S_{\bar{a}_1\bar{a}_2}(\omega)$ and in the magnitude of $S_{\hat{a}_1\hat{a}_2}(\omega)$. These peaks probably occur because the computer is not able to reproduce the measured data from the NRC test rig as a voltage signal, since the magnitude of this data is very small above this frequency. So, when this measured data is supplied to the power amplifiers and the shakers, the voltage signal provided by the computer above 80 Hz is only noise with only a small degree of correlation.

Note that the agreement of $S_{\bar{a}_1\bar{a}_2}(\omega)$ and $S_{\text{data}_2}(\omega)$, in Fig. 46, is approximately equal to the agreement of $S_{\hat{a}_1\hat{a}_2}(\omega)$ and $S_{\text{data}_2}(\omega)$, in Fig. 47, within the bandwidth where the measured data from the NRC test rig are similar, suggesting that the dynamics of the power amplifiers and the shakers does not have considerable influence on the accelerations provided by the virtual pipe systems when this data are supplied to them. So, if the power amplifiers and the shakers are supplied with this measured data filtered by the compensators, the correlation of the accelerations provided by them is not better than the correlation of the measured data than if the devices would be supplied by this data without filtering.

The coherences $\gamma_{\bar{a}_1\bar{a}_2}(\omega)$ and $\gamma_{\hat{a}_1\hat{a}_2}(\omega)$, when the virtual pipe systems and the compensated virtual pipe systems are supplied with the measured data from the NRC test rig, were also calculated using the Welch's modified periodogram method of spectral estimation (OPPENHEIM; SCHAFER, 2011), with the parameters used to calculate the CPSDs $S_{\bar{a}_1\bar{a}_2}(\omega)$

and $S_{\hat{a}_1\hat{a}_2}(\omega)$. Both functions are shown in Fig. 48 (line ▬) in which the coherence $\gamma_{\text{data}_2}(\omega)$ (line ▬) of the measured data is also shown.

Figure 48 – Coherences $\gamma_{\bar{a}_1\bar{a}_2}(\omega)$, $\gamma_{\hat{a}_1\hat{a}_2}(\omega)$ and $\gamma_{\text{data}_2}(\omega)$ by supplying the virtual pipe systems and the compensated virtual pipe systems with the accelerations measured at the NRC test site. $\gamma_{\bar{a}_1\bar{a}_2}(\omega)$ and $\gamma_{\hat{a}_1\hat{a}_2}(\omega)$ are given by the line ▬ and $\gamma_{\text{data}_2}(\omega)$ is given by the line ▬.

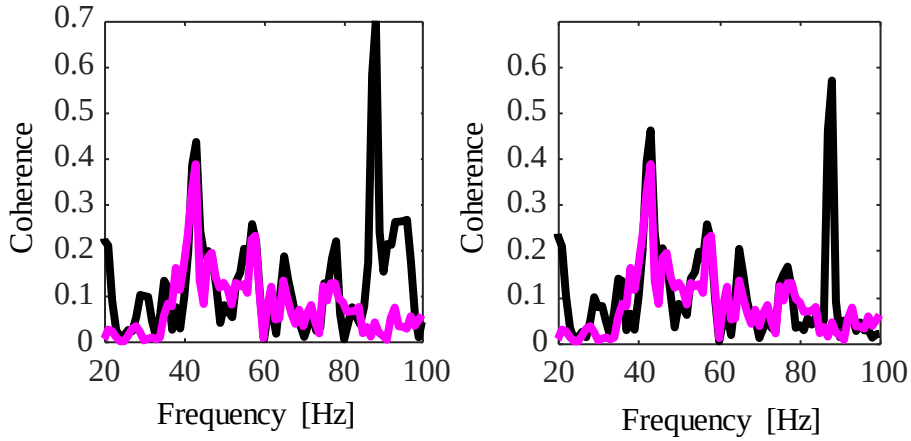

(a) Coherences $\gamma_{\bar{a}_1\bar{a}_2}(\omega)$ and $\gamma_{\text{data}_1}(\omega)$

(b) Coherences $\gamma_{\hat{a}_1\hat{a}_2}(\omega)$ and $\gamma_{\text{data}_2}(\omega)$

Source: elaborated by the author.

Note that the same information provided by $S_{\bar{a}_1\bar{a}_2}(\omega)$, $S_{\hat{a}_1\hat{a}_2}(\omega)$ and $S_{\text{data}_2}(\omega)$ are also observed in $\gamma_{\bar{a}_1\bar{a}_2}(\omega)$, $\gamma_{\hat{a}_1\hat{a}_2}(\omega)$ and $\gamma_{\text{data}_2}(\omega)$. The measured data from the NRC test rig and the accelerations provided by the shakers are similar between approximately 30 Hz and 80 Hz, since the values of these functions are higher within this bandwidth. There are some peaks in the coherences $\gamma_{\bar{a}_1\bar{a}_2}(\omega)$ and $\gamma_{\hat{a}_1\hat{a}_2}(\omega)$ caused by the correlated noise provided by the computer, since it is not able to reproduce the measured data from the NRC test rig above 80 Hz as a voltage signal. The agreement of $\gamma_{\bar{a}_1\bar{a}_2}(\omega)$ and $\gamma_{\text{data}_2}(\omega)$ is similar to the agreement of $\gamma_{\hat{a}_1\hat{a}_2}(\omega)$ and $\gamma_{\text{data}_2}(\omega)$, which suggests that supplying the power amplifiers and the shakers with such a data filtered by the compensators does not provide accelerations, whose correlation is better than the correlation of the measured data than without filtering.

The CCCs $\rho_{\bar{a}_1\bar{a}_2}(\tau)$ and $\rho_{\hat{a}_1\hat{a}_2}(\tau)$ are shown in Fig. 49 (line ▬) in which the CCC $\rho_{\text{data}_2}(\tau)$ (line ▪▪) of the measured data is also shown. By comparing the agreement of $\rho_{\bar{a}_1\bar{a}_2}(\tau)$ and $\rho_{\text{data}_2}(\tau)$ with the agreement of $\rho_{\hat{a}_1\hat{a}_2}(\tau)$ and $\rho_{\text{data}_2}(\tau)$, if the power amplifiers and the shakers are supplied with the measured data from the NRC test site filtered by the compensators, the correlation of the accelerations provided by them is not better than the correlation of the measured data when the devices are supplied by this data without filtering. This occurs because the dynamics of these devices does not have considerable influence on the accelerations provided by the virtual pipe systems, when these measured data are supplied to them.

Figure 49 – CCCs $\rho_{\bar{a}_1\bar{a}_2}(\tau)$, $\rho_{\hat{a}_1\hat{a}_2}(\tau)$ and $\rho_{\text{data}_2}(\tau)$ by supplying the virtual pipe systems and the compensated virtual pipe systems with the accelerations measured at the NRC test site. $\rho_{\bar{a}_1\bar{a}_2}(\tau)$ and $\rho_{\hat{a}_1\hat{a}_2}(\tau)$ are given by the line ▬ and $\rho_{\text{data}_2}(\tau)$ is given by the line ▪▪.

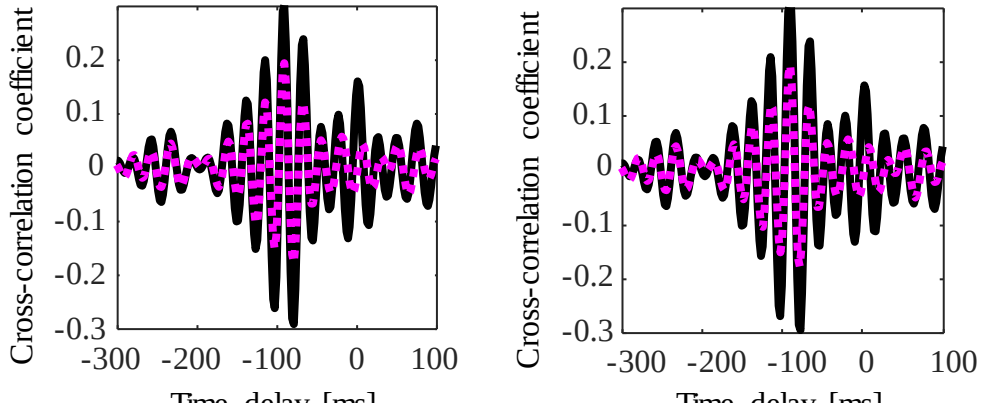

(a) CCCs $\rho_{\bar{a}_1\bar{a}_2}(\tau)$ and $\rho_{\bar{y}_1\bar{y}_2}(\tau)$

(b) CCCs $\rho_{\hat{a}_1\hat{a}_2}(\tau)$ and $\rho_{\bar{y}_1\bar{y}_2}(\tau)$

Source: elaborated by the author.

4.4 CONCLUSIONS

The leak noise simulation, which is the procedure that simulates in the laboratory a leak in a buried pipe using the virtual pipe test rig to generate vibrations similar to the vibrations generated by a leak in a buried pipe, was performed in two different ways. The first was by supplying the virtual pipe systems with synthesized leak noise, which is the leak noise generated by filtering white noise with the model of a buried pipe describe in Chapter 2. The second was by supplying the virtual pipe systems with measured data of real leaks from test sites. The performance of the compensators, that were introduced in Chapter 3, was checked in both domains by supplying the synthesized leak noise and the measured data from the test sites to the virtual pipe systems and to the compensated virtual pipe systems. The vibrations generated by the shakers were measured and the correlation between them was calculated in both domains, which was compared with the correlation of the signals that were supplied to the systems. The agreement between the correlation of the vibrations provided by the virtual pipe systems and the correlation of the signals supplied to them was compared with the agreement between the correlation of the vibrations provided by the compensated virtual pipe systems and the correlation of the signals supplied to them in both domains. It was verified that, if the dynamics of the power amplifiers and the shakers are similar within the bandwidth of the correlation of the signals, the compensators have a considerable influence since they compensate for such dynamics increasing the agreement between the correlation of the vibrations provided by these devices and the signals that are supplied to them. However, if the dynamics of such devices do not have considerable influence in the bandwidth where the signals provided to them are similar, the virtual pipe test rig can be used without the compensators since filtering these signals by them does not improve the correlation of these signals. Given the encouraging results, the virtual pipe test rig can simulate a leak in a buried pipe by supplying the power amplifiers and the shakers with synthesized leak noise or with measured data of a real leak.

5 CONCLUSIONS

5.1 SUMMARY OF THE THESIS

This chapter presents the summary of the work done in this dissertation, the main conclusions and some recommendations for further work. The design of a virtual pipe test rig, which is an indoor bench-top device that can generate vibrations similar to those generated by a leak on a pipe, has been investigated in this dissertation. For this purpose, leak noise is synthesized using a computer, in which white noise is filtered by the model of a buried leaking pipe implemented as a MATLAB® program, that supplies a dual-channel power amplifier and two shakers of the virtual pipe test rig. Since the dynamics of these devices cascaded in series have influence on the leak noise simulation using the virtual pipe test rig (BRENNAN *et al.*, 2016), a simplified approach is presented in which filters, called compensators, are used to compensate for such dynamics.

In Chapter 1, the topics of leak detection and compensation for system dynamics have been introduced, providing the background, the literature review and the main objectives and contributions to knowledge of the dissertation.

In Chapter 2, an overview of leak detection using acoustic correlation is presented in which the concept of cross-correlation has been introduced in the time and frequency domains, by presenting the CCF (and the CCC) and the CPSD respectively. The buried leaking pipe model has been introduced by presenting the FRF between the acceleration of the pipe-wall and the leak pressure. The wavenumber, which is a term in the FRF that contains information about the wave propagation has been introduced in Appendix A. Given the model in frequency domain, the IRF between the acceleration of the pipe-wall and the leak pressure has been introduced by calculating the inverse Fourier transform of the FRF. An example was used to illustrate the model using the parameters of the MDPE pipe and soil from Gao *et al.* (2017). The leak noise simulation was performed by filtering white noise with the IRF of a buried leaking pipe, resulting in the synthesized leak noise. The cross-correlation of the synthesized leak noise was compared in both domains resulting in good agreement.

In Chapter 3, the compensator design approach was illustrated by designing a compensator for a SDOF system. The same approach was used to design the compensators for the virtual pipe systems. The IRF for acceleration and the accelerance of a SDOF system has been introduced in Appendix B. By calculating the FRF of the system, the compensator was designed by inverting this function and applying a time delay to it. To check if it is able to compensate for the dynamics of a SDOF system, the response of the compensator was combined with the response of the system in both domains, resulting in a pure delay system. This was considered satisfactory since the compensated system provides output signals that are approximate delayed versions of the input signals. To check if the modified compensators designed for the virtual pipe systems are able to compensate for their dynamics, a laboratory experiment was performed in which white noise was filtered by the compensators, within the computer, and supplied to the power amplifiers and the shakers of the virtual pipe systems. By calculating the FRF and the IRF of the compensated virtual pipe systems, it was verified that they are also approximate pure delay systems.

In Chapter 4, some laboratory experiments were performed to check if the virtual pipe systems are able to reproduce vibrations representative of the pipe vibrations due to a leak. One experiment was to supply synthesized leak noise, using the model of a buried leaking pipe introduced in Chapter 2, to the power amplifiers and the shakers of the virtual pipe systems; and the another one was to supply signals of real leaks that were measured on test sites to them. Both experiments were performed by the direct supply of the signals to the virtual pipe systems, and by filtering the signals with the compensators, within the computer, before supplying them to the virtual pipe systems. Satisfactory results were achieved for both experiments which proves that the virtual pipe test rig is able to reproduce vibrations that simulates a buried leaking pipe.

In Chapter 5, the summary of the dissertation, the main conclusions and the recommendations for further works are given.

5.2 MAIN CONCLUSIONS

From the investigation conducted with the proposed compensator design approach to compensate for the dynamics of a SDOF system and for the dynamics of a power amplifier and a shaker cascaded in series, the following conclusions can be drawn:

- It has been shown that filtering an input signal with the compensator before supplying it to the system, the output signal provided by such a system is a delayed version of the input with the same time delay used to design the compensator. This means that, within the bandwidth where the compensator was designed, the FRF of the combined system (or compensated system) has a magnitude which is approximately unitary and an unwrapped phase which is a straight line, whose slope is a function of the compensator time delay. The IRF of the combined system is approximately given by a delayed Delta function, whose time delay is the same as the one applied by the compensator.

- The compensator is designed based on the FRF of the system, which can be given by a mathematical model or by measurements. Although the proposed approach was applied to design compensators for systems whose input signals are force or voltage and output signals are accelerations, it can be used to design compensators considering any kind of input and output signals, if the FRF is a known linear function and the system has a single input and a single output.

- It has been shown that the modified compensator can be used to compensate for the dynamics of the system, avoiding unnecessary computation when the compensator is implemented as a filter. Since this function is a truncated version of the compensator, the magnitude of the combined system FRF has Gibbs phenomenon related to the windowing effects resulted from the combination between the response of the compensator, which is a truncated function, and the response of the system. Although the Gibbs phenomenon is negligible in this work, it can be mitigated by increasing the time interval in which the IRF of the modified compensator is represented.

From the investigation conducted with the modified compensators, implemented as filters within the computer, and the laboratory experiments using the virtual pipe test rig together with the synthesized leak noise and the measured data from real leaks, the following conclusions can be drawn:

- The virtual pipe test rig is capable of generating vibration signals similar to that found in a buried water pipe.

- Although the modified compensators apply some time delay to the signals that are supplied to the virtual pipe systems, if the same time delay is applied on both signals, there is no extra delay between the vibrations provided by the virtual pipe systems. Therefore, both modified compensators must be designed with the same time delay.

Finally, it is important to note that the device built in this work, involving power amplifiers and shakers connected in series, can be used together with the modified compensators to simulate other systems aside from a buried leaking pipe. This opens up the possibility to simulate a physical system without the need to invest in sophisticated devices.

5.3 RECOMMENDATIONS FOR FURTHER WORK

The design of an indoor bench-top device, called virtual pipe test rig, which is able to reproduce vibrations that are representative of the vibrations due to a buried leaking pipe, has been investigated. Such a device was built by cascading in series a dual-channel power amplifier and two shakers, whose dynamics have been compensated by using the compensators which are filters designed by a simple approach proposed in this dissertation. The recommended further works are:

1. To implement an algorithm in the compensator design approach that is able to estimate the optimal time interval if it is continuous, or the number of samples if it is discrete, in which the IRF of the modified compensator can be represented.

2. To check the performance of the compensator design approach in compensating the dynamics of other kinds of exciters for different applications.

3. To check the performance of the compensator design approach in compensating the dynamics of the systems given by other kinds of FRFs. It is important to note that if a different sensor is used to measure the output signals of the systems, the FRF has different characteristics, and, consequently, the compensator is also different.

4. To implement a new compensator design approach which is able to compensate for the dynamics of the systems in real-time.

REFERENCES

AHMADIZADEH, M.; MOSQUEDA, G.; REINHORN, A. M. Compensation of actuator delay and dynamics for real-time hybrid structural simulation. *Earthquake Engineering and Structural Dynamics*, Oxford, v. 37, n. 1, p. 21-42, 2007.

ALMEIDA, F. C. L.; BRENNAN, M. J.; JOSEPH, P. F.; WHITFIELD, S.; DRAY, S.; PASCHOALINI, A. T. Measurement of wave attenuation in buried plastic water distribution pipes. *Strojniški vestnik - Journal of Mechanical Engineering*, Santa Clara, v. 60, n. 5, p. 298-306, 2014a.

ALMEIDA, F. C. L.; BRENNAN, M. J.; JOSEPH, P. F.; WHITFIELD, S.; DRAY, S.; PASCHOALINI, A. T. On the acoustic filtering of the pipe and sensor in a buried plastic water pipe and its effect on leak detection: an experimental investigation. *Sensors*, Newton, v. 14, p. 5595-5610, 2014b.

ALMEIDA, F. C. L.; BRENNAN, M. J.; JOSEPH, P. F.; DRAY, S.; WHITFIELD, S.; PASCHOALINI, A. T. Towards an in-situ measurement of wave velocity in buried plastic water distribution pipes for the purposes of leak detection. *Journal of Sound and Vibration*, London, v. 359, p. 40-55, 2015.

ALMEIDA, F. C. L.; BRENNAN, M. J.; JOSEPH, P. F.; GAO, Y.; PASCHOALINI, A. T. The effects of resonances on time delay estimation for water leak detection in plastic pipes. *Journal of Sound and Vibration*, London, v. 420, p. 315-329, 2018.

BAREN, J. V.; MACMILLAN, B. Vibration test replication of operating environments. *Sound and Vibration*, Bay Village, v. 38, n. 8, p. 10-13, 2004.

BRENNAN, M. J.; GAO, Y.; JOSEPH, P. F. On the relationship between time and frequency domain methods in time delay estimation for leak detection in water distribution pipes. *Journal of Sound and Vibration*, London, v. 304, p. 213-223, 2007.

BRENNAN, M. J.; KROLL LIMA, F.; ALMEIDA, F. C. L.; JOSEPH, P. F.; PASCHOALINI, A. T. A virtual pipe rig for testing acoustic leak detection correlators: Proof of concept. *Applied Acoustics*, Oxford, v. 102, p. 137-145, 2016.

BRENNAN, M. J.; KARIMI, M.; ALMEIDA, F. C. L.; LIMA, F. K.; AYALA, P. C.; OBATA, D.; PASCHOALINI, A. T.; KESSISSOGLOU, N. On the role of vibro-acoustics in leak detection for plastic water distribution pipes. *Procedia Engineering*, Amsterdam, v. 199, p. 1350-1355, 2017.

BRENNAN, M. J.; KARIMI, M.; MUGGLETON, J. M.; ALMEIDA, F. C. L.; LIMA, F. K.; AYALA, P. C.; OBATA, D.; PASCHOALINI, A. T.; KESSISSOGLOU, N. On the effects of soil properties on leak noise propagation in plastic water distribution pipes. *Journal of Sound and Vibration*, London, v. 427, p. 120-133, 2018.

BRITISH BROADCASTING CORPORATION – BBC. *The 11 cities most likely to run out of drinking water – like Cape town*, 2018. Available in: https://www.bbc.com/news/world-42982959. Access in: Mar. 28, 2019.

CHEN, C. *Development and numerical simulation of hybrid effective testing method*. 2007. (Ph. D. Dissertation) - Lehigh University, Bethlehem, 2007.

CHEN, C.; RICLES, J. M. Analysis of actuator delay compensation methods for real-time testing. *Engineering Structures*, Oxford, v. 31, p. 2643-2655, 2009.

CHEN, C.; RICLES, J. M.; MARULLO, T. M.; MERCAN, O. Real-time hybrid testing using the unconditionally stable explicit CR integration algorithm. *Earthquake Engineering and Structural Dynamics*, Oxford, v. 38, n. 1, p. 23-44, 2009.

CORNELIS, B.; TOSO, A.; VERPOEST, W.; PEETERS, B. Improved MIMO FRF estimation and model updating for robust time waveform replication on durability test rigs. *In*: PROCEEDINGS OF ISMA 2014 INTERNATIONAL CONFERENCE ON NOISE AND VIBRATION ENGINEERING, 2014, Leuven. *Proceedings of the* […], Leuven: KU Leuven, 2014. p. 737-752. Available in: http://past.isma-isaac.be/downloads/isma2014/papers/isma2014_0704.pdf. Access in: Ago. 23, 2019.

FANTOZZI, M.; CHIRICO, G. D.; FONTANA, E.; TONOLINI, F. Leak inspection on water pipelines by acoustic emission with cross-correlation method. *In*: ANNUAL CONFERENCE PROCEEDING, AMERICAN WATER WORKS ASSOCIATION, ENGINEERING AND OPERATIONS, 1993, San Antonio. *Proceedings of the* […] Santo Antonio: AWWA, 1993. p. 609-622.

FUCHS, H. V.; RIEHLE, R. Ten years of experience with leak detection by acoustic signal analysis. *Applied Acoustics*, Oxford, v. 33, p. 1-19, 1991.

GAO, Y.; BRENNAN, M. J.; JOSEPH, P. F.; MUGGLETON, J. M.; HUNAIDI, O. A model of the correlation of leak noise in buried plastic water pipes. *Journal of Sound and Vibration*, London, v. 277, p. 133-148, 2004.

GAO, Y.; BRENNAN, M. J.; JOSEPH, P. F.; MUGGLETON, J. M.; HUNAIDI, O. On the selection of acoustic/vibration sensors for leak detection in plastic water pipes. *Journal of Sound and Vibration*, London, v. 283, p. 927-941, 2005.

GAO, Y.; BRENNAN, M. J.; JOSEPH, P. F. A comparison of time delay estimators for the detection of leak noise signals in plastic water distributions pipes. *Journal of Sound and Vibration*, London, v. 292, p. 552-570, 2006.

GAO, Y.; SUI, F.; MUGGLETON, J. M.; YANG, J. Simplified dispersion relationships for fluid-dominated axisymmetric wave motion in buried fluid-filled pipes. *Journal of Sound and Vibration*, London, v. 375, p. 386-402, 2016.

GAO, Y., LIU, Y.; MUGGLETON, J. M. Axisymmetric fluid-dominated wave in fluid-filled plastic pipes: loading effects of surrounding elastic medium. *Applied Acoustics*, Oxford, v. 116, p. 43-49, 2017.

GRANT, S. B.; SAPHORES, J. D.; FELDMAN, D. L.; HAMILTON, A. J.; FLETCHER, T. D.; COOK, P. L. M.; STEWARDSON, M.; SANDERS, B. F.; LEVIN, L. A.; AMBROSE, R. F.; DELETIC, A.; BROWN, R.; JIANG, S. C.; ROSSO, D.; COOPER, W. J.; MARUSIC, I. Taking the "waste" out of "wastewater" for human water security and ecosystem sustainability. *Science*, Washington, v. 337, p. 681-686, 2012.

HORIUCHI, T.; KONNO, T. A new method for compensating actuator delay in real-time hybrid experiment. *Philosophical Transactions of the Royal Society Series A*, London, v. 359, p. 1893-1909, 2001.

HUNAIDI, O.; GIAMOU, P. Ground-penetrating radar for detection of leaks in buried plastic water distribution pipes. *In*: INTERNATIONAL CONFERENCE ON GROUND-PENETRATING RADAR, 7, 1998, Lawrence. *Conference of the* […] Lawrence: Radar Systems and Remote Sensing Laboratory, 1998. Available in: https://pdfs.semanticscholar.org/1495/5303ae2eae60cd88f996d74c05432caa044d.pdf. Access in: Ago. 23, 2019.

HUNAIDI, O.; CHU, W. T. Acoustical characteristics of leak signals in plastic water distribution pipes. *Applied Acoustics*, Oxford, v. 58, n. 3, p. 235–254, 1999.

HUNAIDI, O.; CHU, W. T.; WANG, A.; GUAN, W. Detecting leaks in plastic pipes. *Journal of the American Water Works Association*, Oxford, v. 92, p. 82-94, 2000a.

HUNAIDI, O. *Detecting leaks in water-distribution pipes*. Canada: National Research Council, 2000b. Construction Technology Update, 40.

IWANAGA, M. K.; BRENNAN, M. J.; SCUSSEL, O.; ALMEIDA, F. C. L. On the design of a digital filter to compensate for the shaker dynamics in a virtual pipe test rig. *In:* INTERNATIONAL SYMPOSIUM ON DYNAMIC PROBLEMS OF MECHANICS, 18, 2019, Búzios. *International of the* […] 2019. Búzios: ABCM, 2019.

JUNG, R. Y.; SHING, P. B. Performance evaluation of a real-time pseudodynamic test system. *Earthquake Engineering and Structural Dynamic*, Oxford, v. 35, n.7, p. 789-810, 2006.

KINGDOM, B.; LIEMBERGER, R.; MARIN, P. *The challenge of reducing non-revenue water (NRW) in developing countries*. [S.l.]: The World Bank, Washington, 2006. Available in: https://siteresources.worldbank.org/INTWSS/Resources/WSS8fin4.pdf. Access in: Ago. 23 2019. Water Supply and Sanitation Board Discussion Paper Series, Paper, 8.

Li, X., Zhiqun, D.D., Rauchenstein, L.T., Carlson, T.J. Contributed Review: Source-localization algorithms and applications using time of arrival and time difference of arrival measurements. *Review of Scientific Instruments*, 87, 041502, 2016.

LIMA, F. K.; BRENNAN, M. J.; ALMEIDA, F. C. L.; AYALA, P. C.; OBATA, D.; SCUSSEL, O.; PASCHOALINI, A. T. Comparison of two methods of excitation for leak noise velocity measurement in buried plastic water pipes. *In:* INTERNATIONAL SYMPOSIUM ON DYNAMIC PROBLEMS OF MECHANICS, 18, 2019, Búzios. *International of the* […] 2019. Búzios: ABCM, 2019.

LISTON, D. A.; LISTON, J. D. Leak detection techniques. *Journal of the New England Water Works Association*, Holliston, v. 106, n. 2, p. 103-108, 1992.

MERCAN, O. *Analytical and experimental studies on large scale, real-time pseudodynamic testing*. 2007. Bethlehem: Lehigh University, Department of Civil and Environmental Engineering, 2007. 412 p.

MUGGLETON, J. M.; BRENNAN, M. J.; PINNINGTON, R. J. Wavenumber prediction of waves in buried pipes for water leak detection. *Journal of Sound and Vibration*, London, v. 249, p. 5, p. 939-954, 2002.

MUGGLETON, J.; BRENNAN, M. J. Leak noise propagation and attenuation in submerged plastic water pipes. *Journal of Sound and Vibration*, London, v. 278, p. 527-537, 2004a.

MUGGLETON, J. M.; BRENNAN, M. J.; LINFORD, P. W. Axisymmetric wave propagation in fluid-filled pipes: wavenumber measurements in in-vacuo and buried pipes. *Journal of Sound and Vibration*, London, v. 270, p. 272-190, 2004b.

Muggleton, J.M., Brennan, M.J. Axisymmetric wave propagation in buried, fluid-filled pipes: Effects of discontinuities. *Journal of Sound and Vibration*, 281, 849-867, 2005.

MUGGLETON, J. M.; BRENNAN, M. J. The design and instrumentation of an experimental rig to investigate acoustic methods for the detection and location of underground piping systems. *Applied Acoustics*, Oxford, v. 69, n. 11, p. 1101-1107, 2008.

MUGGLETON, J. M.; BRENNAN, M. J.; GAO, Y. Determining the location of buried plastic water pipes from measurements of ground surface vibration. *Journal of Applied Geophysics*, Amsterdam, v. 75, n. 1, p. 54-61, 2011.

MUGGLETON, J. M.; YAN, J. Wavenumber prediction and measurement of axisymmetric waves in buried fluid filled pipes: inclusion of shear coupling at a lubricated pipe/soil interface. *Journal of Sound and Vibration*, London, v. 332, n. 5, p. 1216-1230, 2013.

O GLOBO. *Vazamento e "gatos" fazem oito estados perderem metade ou mais da água que produzem, diz estudo*. 2019, Available in: https://g1.globo.com/economia/noticia/2019/06/05/oito-estados-do-pais-perdem-metade-ou-mais-da-agua-que-produzem-com-vazamentos-e-gatos-diz-estudo.ghtml. Access in: Jun. 19, 2019.

OPPENHEIM, A.; SCHAFER, R. *Discrete-time signal processing*. Upper Saddle River: Pearson Education, 2011.

PINNINGTON, R. J.; BRISCOE, A. R. Externally applied sensor for axisymmetric waves in a fluid filled pipe. *Journal of Sound and Vibration*, London, v. 173, n. 4, p. 503-516, 1994.

PUUST, R.; KAPELAN, Z.; SAVIC, D. A.; KOPPEL, T. A review of methods for leakage management in pipe networks. *Urban Water Journal*, Oxfordshire, v. 7, n. 1, p. 25-45, 2010.

RITU; DHULL, S. K. Review on acoustic source localization techniques. *European Journal of Advances in Engineering and Technology*, v. 2, n. 9, p. 72-77, 2015. Available in: http://www.ejaet.com/PDF/2-9/EJAET-2-9-72-77.pdf. Access in: Ago. 23, 2019.

SCUSSEL, O.; BRENNAN, M. J.; MUGGLETON, J. M.; ALMEIDA, F. C. L.; PASCHOALINI, A. T. On the dynamic loading effects of soil on plastic water distribution pipes and its significances for leak detection using acoustics. *In*: PROCEEDINGS OF ASME 2018 INTERNATIONAL MECHANICAL ENGINEERING CONGRESS AND EXPOSITION, 2018, Pittsburgh. *Proceedings of the* […] Pittsburgh: ASME, 2018. 7 p.

SCUSSEL, O.; BRENNAN, M. J.; MUGGLETON, J. M.; ALMEIDA, F. C. L.; PASCHOALINI, A. T. Estimation of the bulk and shear moduli of soil surrounding a plastic water pipe using measurements of the predominantly fluid wave in the pipe. *Journal of Applied Geophysics*, Amsterdam, v. 164, p. 237-246, 2019.

SERVIÇO DE ABASTECIMENTO DO ESTADO DE SÃO PAULO - SABESP. *Combate a perdas*. Available in: http://site.sabesp.com.br/site/interna/Default.aspx?secaoId=499. Access in: Mar. 28, 2019.

SHEN, G.; ZHENG, S. T.; YE, Z. M.; HUANG, Q. T.; CONG, D. C.; HAN, J. W. Adaptative inverse control of time waveform replication for electrohydraulic shaking table. *Journal of Vibration and Control*, London, v. 17, n. 11, p. 1611-1633, 2010.

SHEN, G.; ZHU, Z. C.; LI, X.; LI, G.; TANG, Y.; LIU, S. Experimental evaluation of acceleration waveform replication on electrohydraulic shaking tables: a review. *International Journal of Advanced Robotic Systems*, London, v. 13, n. 5, p. 1-25, 2016.

SHEN, G.; ZHU, Z. C.; LI, X.; WANG, Q. G.; LI, G.; TANG, Y. Acceleration waveform replication on six-degree-of-freedom redundant electro-hydraulic shaking tables using an inverse model controller with a modelling error. *Transactions of the Institute of Measurements and Control*, London, v. 40, n. 3, p. 968-986, 2018.

SHIN, K.; HAMMOND, J. K. *Fundamentals of signal processing for sound and vibration engineers*. Chichester: Wiley, 2008.

SNEDDON, K. W.; OLHOEFT, G. R.; POWERS, M. H. Determining and mapping DNAPL saturation values from noninvasive GPR measurements. *In*: EEGS SYMPOSIUM ON THE APPLICATION OF GEOPHYSICS TO ENGINEERING AND ENVIRONMENTAL PROBLEMS, SAGEEP, 13, 2000, Arlington. *Proceedings of the* […]. Arlington: EEGS, 2000. Available in: http://earthdoc.eage.org/publication/publicationdetails/?publication=46447. Access in: Ago. 23 2019.

WEIL, G. J. Non contact, remote sensing of buried water pipeline leaks using infrared thermography. *In*: ANDERSON, J. L. (ed.). *Water resources planning and management and urban water resources*. [S.l.]: ASMES, 1993. p. 404-407.

YAO, J.; WAN, Z.; ZHAO, Y.; YU, J.; QIAN, C.; FU, Y. Resonance suppression for hydraulic servo shaking table based on adaptative notch filter. *Shock and Vibration*, New

York, v. 2019, 12 p., 2019. Available in:
http://downloads.hindawi.com/journals/sv/2019/9407520.pdf. Access in: Ago. 23, 2019.

APPENDIX A – WAVENUMBER PREDICTION

A.1 INTRODUCTION

This appendix briefly describes the prediction of a variable, named wavenumber, which contains information regarding the wave propagation and energy distribution within a medium. Recent research has shown that at low frequencies, one particular axisymmetric $(n=0)$ wave, named fluid-dominated $(s=1)$ wave, is considered the main carrier of the vibrational energy in buried fluid-filled plastic pipes (MUGGLETON *et al.*, 2002; MUGGLETON *et al.*, 2004a; MUGGLETON; BRENNAN, 2005; MUGGLETON; YAN, 2013). This special case, where $n=0$ and $s=1$, corresponds to a breathing mode (or no motion at all) of the pipe shell in the circumferential direction. An analytical model of the fluid-filled pipe surrounded by an elastic medium was proposed by Gao *et al.* (2017) for investigating the loadings effects of such a medium, acting as a combination of mass, stiffness and radiation damping, on the propagation characteristic of the $(s=1)$ wave. Then, such a model was studied and improved by Scussel *et al.* (2018), which was rewritten with physical insight.

A.2 ANALYTICAL MODEL FOR WAVENUMBER PREDICTION WITH PHYSICAL INSIGHT

At low frequencies, well below the pipe ring frequency, the axisymmetric $(n=0)$ fluid-dominated $(s=1)$ wavenumber in a fluid-filled pipe surrounded by an infinite elastic medium given by the "no-slip" coupling, where the soil-pipe interface is assumed to be under compact contact, was proposed by Gao *et al.* (2017).

In this study, soil is the elastic medium that surrounds the fluid-filled pipe. The combination of the fluid-filled pipe and the soil is modelled as a cylindrical tri-layer system with the cross-section as shown in Fig. 50. The wavenumber, in this case, is given by (SCUSSEL *et al.*, 2018)

$$k(\omega)=k_{\text{water}}(\omega)\left(1+\frac{K_{\text{water}}}{K_{\text{pipe}}+K_{\text{soil}}}\right)^{\frac{1}{2}}, \tag{23}$$

where $k_{\text{water}}(\omega)=\omega\left(\rho_{\text{water}}/B_{\text{water}}\right)^{\frac{1}{2}}$ is the free-field wavenumber of water, which is a function of the density ρ_{water}, bulk modulus B_{water} and the angular frequency ω. The term

$K_{\text{water}} = 2B_{\text{water}}/a$ is the stiffness of the water and K_{pipe} is the dynamic stiffness of the pipe-wall which is given by

$$K_{\text{pipe}} = \frac{K_{\text{pipe}}^{(\text{stiff})}}{\left(1-\nu_{\text{pipe}}^2\right)} + K_{\text{pipe}}^{(\text{inertia})} = \frac{E_{\text{pipe}}h}{a^2\left(1-\nu_{\text{pipe}}^2\right)} - \omega^2\rho_{\text{pipe}}h, \tag{24}$$

where ρ_{pipe} and ν_{pipe} are the density and Poisson's ratio of the pipe respectively. The terms $K_{\text{pipe}}^{(\text{stiff})}$ and $K_{\text{pipe}}^{(\text{inertia})}$ denote the stiffness and inertial components of the pipe wall respectively.

Figure 50 – Schematic diagram of the cross-section of a fluid-filled pipe surrounded by infinite soil.

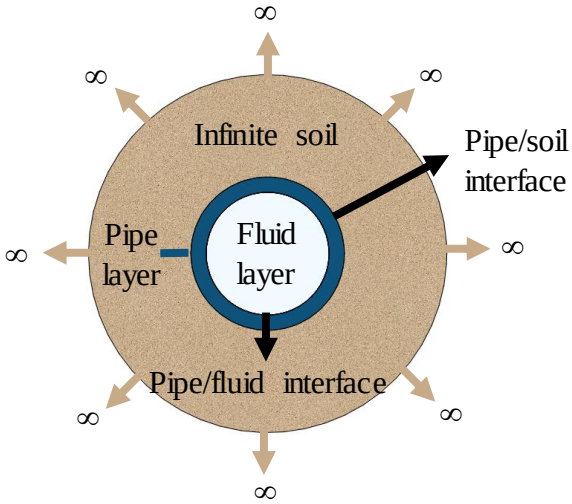

Source: elaborated by the author.

The term K_{soil} is the dynamic stiffness of surrounding medium given by

$$K_{\text{soil}} = \frac{\mu_{\text{soil}}}{a}K_{\text{soil}}^{(\text{a})} + \frac{E_{\text{pipe}}h}{a^2\left(1-\nu_{\text{pipe}}^2\right)}K_{\text{soil}}^{(\text{b})}, \tag{25}$$

where the terms $K_{\text{soil}}^{(\text{a})}$ and $K_{\text{soil}}^{(\text{b})}$ are given by

$$K_{\text{soil}}^{(\text{a})} = 2 + \frac{k_r^r a k_r^2 a^2 \left[\frac{H_0\left(k_r^r a\right)}{H_0^{'}\left(k_r^r a\right)}\right]\left[\frac{H_0\left(k_d^r a\right)}{H_0^{'}\left(k_d^r a\right)}\right]}{k_r^r a k_d^r a \left[\frac{H_0\left(k_r^r a\right)}{H_0^{'}\left(k_r^r a\right)}\right] + k^2 a^2 \left[\frac{H_0\left(k_d^r a\right)}{H_0^{'}\left(k_d^r a\right)}\right]} \tag{26}$$

and

$$K_{\text{soil}}^{(\text{b})} = -\frac{\nu_{\text{pipe}}^2}{\left(1+\frac{S_1}{k^2 a^2}\right)} + \frac{j2\nu_{\text{pipe}} S_2}{ka\left(1+\frac{S_1}{k^2 a^2}\right)} + \frac{S_2^2}{k^2 a^2 \left(1+\frac{S_1}{k^2 a^2}\right)}, \tag{27}$$

in which

$$S_1 = -\mu_{\text{soil}} \frac{\left(1-\nu_{\text{pipe}}^2\right) a}{E_{\text{pipe}} h} \left[\frac{k_d^r a k_r^2 a^2}{k_r^r a^2 k_d^r \left[\frac{H_0\left(k_r^r a\right)}{H_0^{'}\left(k_r^r a\right)}\right] + k^2 a^2 \left[\frac{H_0\left(k_d^r a\right)}{H_0^{'}\left(k_d^r a\right)}\right]}\right] \tag{28}$$

and

$$S_2 = \frac{j\mu_{\text{soil}}\left(1-\nu_{\text{pipe}}^2\right) k a^2}{E_{\text{pipe}} h} \left[2 - \frac{k_r^2 a^2 \left[\frac{H_0\left(k_d^r a\right)}{H_0^{'}\left(k_d^r a\right)}\right]}{k_r^r a^2 k_d^r \left[\frac{H_0\left(k_r^r a\right)}{H_0^{'}\left(k_r^r a\right)}\right] + k^2 a^2 \left[\frac{H_0\left(k_d^r a\right)}{H_0^{'}\left(k_d^r a\right)}\right]}\right]. \tag{29}$$

The terms k_d^r and k_r^r are the surrounding soil radial wavenumbers given by $k_d^r = \sqrt{k_d^2 - k^2}$ and $k_r^r = \sqrt{k_r^2 - k^2}$, where k_d and k_r are the compressional and shear wavenumbers in the surrounding soil, respectively, given by $k_d^2 = \omega^2 \rho_{\text{soil}} / (\lambda_{\text{soil}} + 2\mu_{\text{soil}})$ and $k_r^2 = \omega^2 \rho_{\text{soil}} / \mu_{\text{soil}}$, in which ρ_{soil} is the density of the surrounding soil and $\lambda_{\text{soil}} = B_{\text{soil}} - 2G_{\text{soil}}/3$, $\mu_{\text{soil}} = G_{\text{soil}}$ are the Lamé coefficients, which are function of bulk modulus B_{soil} and shear modulus G_{soil} of the soil. The term H_0 is the Hankel function of zero order and second kind which describes the outgoing waves in the surrounding soil (SCUSSEL *et al.*, 2018), and ' denotes the spatial derivative.

The real part of the wavenumber $k(\omega)$ provides the wavespeed $c(\omega)$ by (GAO *et al.*, 2004)

$$\text{Re}\{k(\omega)\} = \frac{\omega}{c(\omega)}, \tag{30}$$

and the imaginary part of $k(\omega)$ provides the attenuation of the fluid-borne wave (GAO *et al.*, 2004)

$$\text{Attenuation} = \frac{-20\,\text{Im}\{k(\omega)\}}{\ln(10)}, \tag{31}$$

which is given in terms of dB/m.

APPENDIX B – IMPULSE RESPONSE FUNCTIONS FOR DISPLACEMENT, VELOCITY AND ACCELERATION OF A SINGLE DEGREE OF FREEDOM

B.1 INTRODUCTION

This appendix describes the calculation of the Impulse Response Function (IRF) for velocity and the IRF for acceleration of a Single Degree of Freedom (SDOF) system, by differentiating the displacement response to an impulse. An alternative way is shown to obtain such functions by multiplying the response with the Heaviside step function before the differentiation. The parameters of the SDOF system given in Chapter 3 are also used in this appendix as an example to verify the difference between the functions obtained by differentiating the displacement response of the system and by using the inverse Fourier transform of the accelerance of the system. Such a comparison is important to understand the actual shape of the IRF for acceleration of a SDOF system, whose representation in frequency domain is the accelerance of such a system.

B.2 DIFFERENTIATION OF THE RESPONSE OF A SDOF SYSTEM TO AN IMPULSE

The displacement response $y(t)$ of a SDOF system to an impulse $\hat{f}$, at $t=0$, is given by

$$y(t)=\frac{\hat{f}}{m\omega_d}e^{-\zeta\omega_n t}\sin(\omega_d t),\ \text{for } t\geq 0, \tag{32}$$

where ω_n and ω_d are the natural frequency and damped natural frequency of the system, respectively, given by $\omega_n=\sqrt{k/m}$ and $\omega_d=\omega_n\sqrt{1-\zeta^2}$. Furthermore, ζ is the damping ratio of the system, given by $\zeta=c\Big/\left(2\sqrt{mk}\right)$, and the terms m, k and c are the mass, stiffness and damping of the SDOF system respectively.

If $\hat{f}$ is a Dirac delta function, then the response $y(t)$ becomes the displacement IRF $h(t)$ of a SDOF system, which is given by

$$h(t) = \frac{1}{m\omega_d} e^{-\zeta\omega_n t} \sin(\omega_d t). \tag{33}$$

An alternative way of writing Eq. (32), considering that $\hat{f}$ is a Dirac delta function, is

$$y(t) = H_e(t) h(t), \tag{34}$$

where $H_e(t)$ is the Heaviside step function. Differentiating Eq. (34) with respect to t gives

$$\dot{y}(t) = \dot{H}_e(t) h(t) + H_e(t) \dot{h}(t), \tag{35}$$

where $\dot{H}_e(t) h(t) = \delta(t) h(t) = 0$, in which $\delta(t)$ is the Dirac delta function, and

$$\dot{h}(t) = \frac{1}{m\omega_d} e^{-\zeta\omega_n t} \left(\omega_d \cos(\omega_d t) - \zeta\omega_n \sin(\omega_d t)\right). \tag{36}$$

So, the velocity response $\dot{y}(t)$ of a SDOF system is given by

$$\dot{y}(t) = H_e(t) \dot{h}(t) = \frac{1}{m\omega_d} e^{-\zeta\omega_n t} \left(\omega_d \cos(\omega_d t) - \zeta\omega_n \sin(\omega_d t)\right). \tag{37}$$

Note from Eqs. (36)-(37) that $\dot{y}(t)$ is equal to $\dot{h}(t)$, i.e., the velocity response of a SDOF system to a force impulse described by a Dirac delta function, given by Eq. (37), can be determined simply by the differentiation of $h(t)$ with respect to t.

Differentiating Eq. (35) with respect to t gives

$$\ddot{y}(t) = \dot{H}_e(t) \dot{h}(t) + H_e(t) \ddot{h}(t), \tag{38}$$

where $\dot{H}_e(t) \dot{h}(t) = \delta(t)/m$ and

$$\ddot{h}(t) = \frac{1}{m\omega_d} e^{-\zeta\omega_n t}\left(\left(\left(\zeta\omega_n\right)^2 - \omega_d^2\right)\sin\left(\omega_d t\right) - 2\zeta\omega_n\omega_d\cos\left(\omega_d t\right)\right). \tag{39}$$

So, the acceleration response $\ddot{y}(t)$ of a SDOF system is given by

$$\ddot{y}(t) = \frac{\delta(t)}{m} + \frac{1}{m\omega_d} e^{-\zeta\omega_n t}\left(\left(\left(\zeta\omega_n\right)^2 - \omega_d^2\right)\sin\left(\omega_d t\right) - 2\zeta\omega_n\omega_d\cos\left(\omega_d t\right)\right). \tag{40}$$

If $\zeta << 1$, Eq. (40) can be approximated by

$$\ddot{h}(t) \approx -\frac{\omega_d}{m} e^{-\zeta\omega_n t}\sin\left(\omega_d t\right) \tag{41}$$

and, consequently,

$$\ddot{y}(t) \approx \frac{\delta(t)}{m} - \frac{\omega_d}{m} e^{-\zeta\omega_n t}\sin\left(\omega_d t\right). \tag{42}$$

Note that Eq. (40) must be determined by adding the term $\delta(t)/m$ to the differentiation of $\dot{h}(t)$. Such information can be checked by calculating the inverse Fourier transform of the accelerance $H^a(\omega)$ of the SDOF system, which is the FRF that provides the relationship between acceleration and force of the system in the frequency domain and is given by

$$H^a(\omega) = \frac{-\omega^2}{k - m\omega^2 + j\omega c}, \tag{43}$$

where $j = \sqrt{-1}$ and ω is the angular frequency.

Figs. 51-52 show the importance of considering the term $\delta(t)/m$ in the IRF $\ddot{h}(t)$ when $\ddot{y}(t)$ is the response of a SDOF system to a Dirac delta function. Such functions were plotted considering the parameters of the SDOF system presented in Chapter 3 (values of mass, stiffness and damping ratio are given in Tab. 3.1). Fig. 51 compares the IRF $\ddot{h}(t)$ calculated through Eq. (40) (line ▪▪) and the differentiation of $\dot{h}(t)$ (line ▬) with the inverse Fourier transform of $H^a(\omega)$ (line ▬). Note that the inverse Fourier transform of $H^a(\omega)$ and the IRF for acceleration calculated through Eq. (40), considering the Heaviside step function, have the best agreement. Note also that the lines ▪▪, ▬ and ▬ are overlaid for $t > 0$ in Fig. 51.

Figure 51 – IRF $\ddot{h}(t)$ of the SDOF system. $\ddot{h}(t)$ calculated using the inverse Fourier transform of $H^a(\omega)$ is given by the line ▬, $\ddot{h}(t)$ calculated through Eq. (40) is given by the line ▪▪ and $\ddot{h}(t)$ calculated through the differentiation of $\dot{h}(t)$ is given by the line ▬.

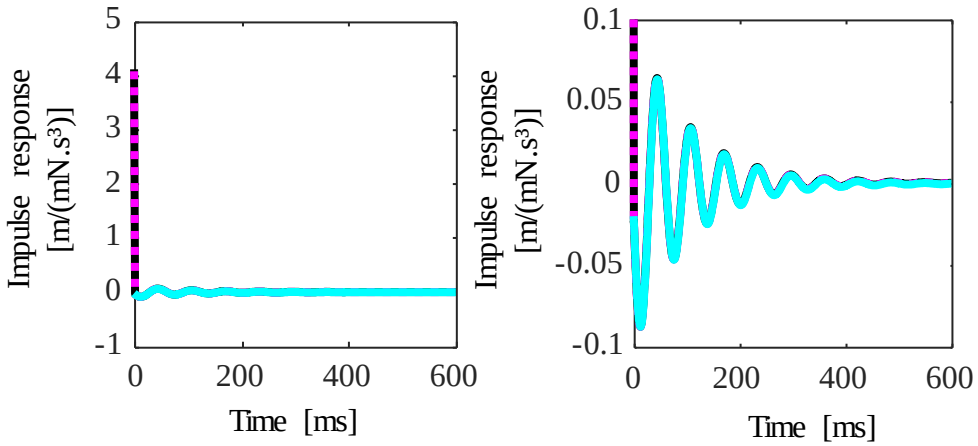

(a) IRF $\ddot{h}(t)$ (b) Zoomed IRF $\ddot{h}(t)$

Source: elaborated by the author.

Fig. 52 compares such functions in the frequency domain. The Fourier Transform of Eq. (40) (line ▪▪) and the Fourier transform of the differentiation of $\dot{h}(t)$ (line ▬) are compared with the FRF $H^a(\omega)$ given by Eq. (43) (line ▬). Note that the Fourier transform of Eq. (40) and the FRF $H^a(\omega)$, given by Eq. (43), are in agreement.

Figure 52 – FRF $H^a(\omega)$, of the SDOF system. $H^a(\omega)$ calculated using Eq. (43) is given by the line ▬, $H^a(\omega)$ calculated using the Fourier transform of Eq. (40) is given by the line ▪▪ and $H^a(\omega)$ calculated through the Fourier transform of the differentiation of $\dot{h}(t)$ is given by the line ▬.

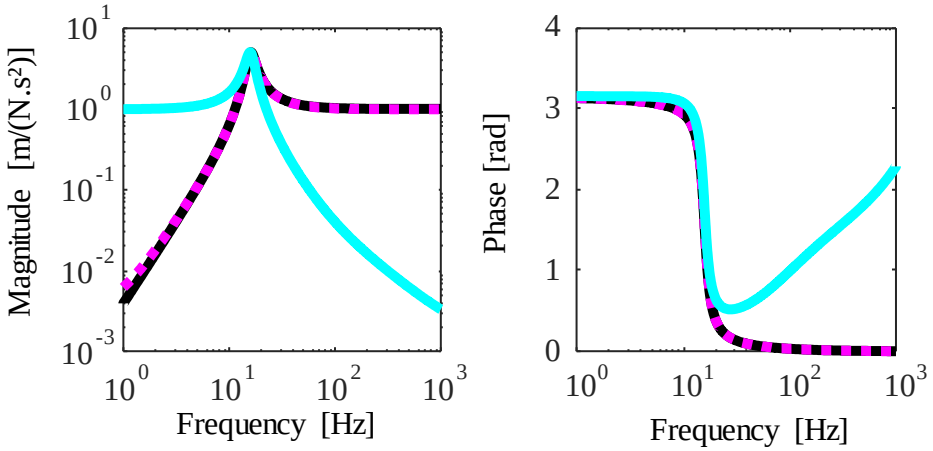

(a) Magnitude (b) Phase

Source: elaborated by the author.